ABSTRACT

GRAPHENE-COATED SUBSTRATES FOR BIOCHEMICAL AND OPTO-ELECTRONIC APPLICATIONS

by
Amrita Banerjee

Graphene – monolayer or a few layers of graphite - has proven to possess remarkable properties: large thermal conductivity, mechanical robustness, two-dimensional ultra large electronic mobility, chemical inertness and biochemical compatibility. Realization of some applications has been impeded by lack of a large area deposition method. By using a novel methodology to deposit graphene on solid and perforated substrates, various optoelectronic and biochemical elements have been demonstrated in this thesis: (1) graphene based transistors were fabricated and their characteristics were assessed. The mobility for such transistors exceeded 5000 cm^2/V·s, much larger than their silicon based counterparts. Such attribute opens up new potential application in the field of very large scale integration (VLSI). (2) In parallel to vacuum tubes, where accelerated electrons are retained by a biased screen, a graphene based retaining electrode, placed in a wet-cell battery has stopped the battery's current. In that respect, graphene proved to be a good ionic screening electrode because it does not oxidize easily. Applications could be in the field of ionic transistors and special electrochemical cells. (3) As surface plasmon waveguides enter the electronic circuitry, surface plasmon sources are required. Graphene based surface plasmons lasers were fabricated and characterized. Their attributes, illustrated by operational threshold, gain, spectral line narrowing and feedback at 630 nm all alluded to the action of a laser. Such, local plasmonic sources may find applications in optoelectronic and sensor systems. (4) Infrared (IR) metal-mesh screens have been

investigated as optical filters in the visible through the THz spectral region for astronomy and remote sensing applications. By interfacing these metal mesh screens with graphene, new spectroscopic platforms were fabricated. It has been shown that these platforms enhance IR and Raman signals of molecules and, specifically, signal of bio-species at the screens' surface. Biochemical sensing applications are envisioned. (5) Finally, the Raman spectra of molecules, deposited on graphene-coated nano-hole arrays have been investigated. It has been shown that these platforms were able to intensify such Raman signals, significantly. Potential usage of such platforms as biochemical sensors is envisioned.

GRAPHENE-COATED SUBSTRATES FOR BIOCHEMICAL
AND OPTOELECTRONIC APPLICATIONS

by
Amrita Banerjee

A Dissertation
Submitted to the Faculty of
New Jersey Institute of Technology
in Partial Fulfillment of the Requirements for the Degree of
Doctor of Philosophy in Electrical Engineering

Department of Electrical and Computer Engineering

August 2012

.

APPROVAL PAGE

GRAPHENE-COATED SUBSTRATES FOR BIOCHEMICAL
AND OPTOELECTRONIC APPLICATIONS

Amrita Banerjee

Dr. Haim Grebel, Dissertation Advisor	Date
Professor of Electrical and Computer Engineering, NJIT	

Dr. Karl D. Moeller, Dissertation Co-Advisor	Date
Research Faculty of Electrical and Computer Engineering, NJIT	

Dr. Leonid Tsybeskov, Committee Member	Date
Professor of Electrical and Computer Engineering, NJIT	

Dr. Durga Misra, Committee Member	Date
Professor of Electrical and Computer Engineering, NJIT	

Dr. Gerald Whitman, Committee Member	Date
Professor of Electrical and Computer Engineering, NJIT	

Dr. Andrei Sirenko, Committee Member	Date
Associate Professor of Physics Department, NJIT	

BIOGRAPHICAL SKETCH

Author: Amrita Banerjee

Degree: Doctor of Philosophy

Date: January 2012

Undergraduate and Graduate Education:

- Doctor of Philosophy in Electrical Engineering,
  New Jersey Institute of Technology, Newark, NJ, 2012

- Master of Science in Electrical Engineering,
  New Jersey Institute of Technology, Newark, NJ, 2006

- Bachelor of Engineering in Electronics and Communication Engineering,
  University of Burdwan, West Bengal, India, 2004

Major: Electrical Engineering

Publications:

Amrita Banerjee, Raquel Perez-Castillejos, D. Hahn, Alex Smirnov and Haim Grebel, "Microfluidic Channels on Nanopattered Substrate: Monitoring Protein Binding to Lipid Bilayers with Surface-Enhanced Raman Spectroscopy," *Chemical Physics Letters*, vol. 489, no.1-3, pp. 121-126, 2010.

Amrita Banerjee, D. Sliwinski, K. P. Stewart, Dieter K. Moeller and Haim Grebel, "Curved Infrared Screens," *Optics Letters*, vol. 35, no. 10, pp. 1635-1637, 2010.

Amrita Banerjee and Haim Grebel, "On the Stopping Potential of Ionic Currents," *Electrochemistry Communications*, vol. 12, no. 2, pp. 274-277, 2010.

Amrita Banerjee, Dieter K. Moeller, Alex Smirnov and Haim Grebel, "Graphenated IR Screens," *IEEE Sensor Journal*, vol. 10, no. 3, pp. 419-422, 2010.

Amrita Banerjee and Haim Grebel, "Depositing Graphene Films on a Solid and Perforated Substrates," *Nanotechnology*, vol. 19, no. 36, pp. 365303-365306, 2008.

Amrita Banerjee and Haim Grebel, "Surface Plasmon Lasers with Quantum Dots as Gain Media," *Applied Physics Letters*, vol. 95, no. 25, pp. 251106-365309, 2009.

Amrita Banerjee, Rui-Qiong Li and Haim Grebel, "Raman Spectroscopy with Graphenated Anodized Aluminum Oxide Substrate," *Nanotechnology*, vol. 20, no. 29, pp. 295502-295509, 2009.

Rui-Qiong Li, Amrita Banerjee and Haim Grebel, "The Possibilities for Surface Plasmons Lasers," *Optics Express*, vol. 17, no. 3, pp. 1622-1627, 2009.

Amrita Banerjee, Sumit Chakraborty and Haim Grebel, "Graphenated IR Screen for Detection of Human and Avian Flu Viruses," *Proceedings of the IEEE Conference on Nanotechnology*, art. no. 6144595, pp. 354-357, 2011.

Amrita Banerjee, Sumit Chakraborty and Haim Grebel, "Detection of Human and Avian Flu Viruses Using Graphenated Infrared Screen," *Technical Proceedings of the 2011 NSTI Nanotechnology Conference and Expo, NSTI-Nanotech*, no. 3, pp. 105-108, 2011.

Amrita Banerjee, Karl D. Moeller and Haim Grebel, "Novel Spectroscopic Platforms for Bio-Chemical Detection: Graphenated IR Screen," *ECS Transaction*, vol. 19, no. 5, pp. 233-236, 2009.

Amrita Banerjee and Haim Grebel, "Freestanding Graphene and Its Applications," *ECS Transaction*, vol. 19, no. 5, pp. 53-56, 2009.

Sreeya Sreevatsa, Amrita Banerjee and Haim Grebel, "Graphene as a Permeable Ionic Barrier," *ECS Transaction*, vol. 19, no. 5, pp. 259- 262, 2009.

Amrita Banerjee, Karl D. Moeller and Haim Grebel, "Graphenated IR Screens: A New Spectroscopic Platform for Bio-species," *MRS Symposium Proceedings*, vol. 1133E, pp. AA0704, 2009.

Amrita Banerjee, Rui-Qiong Li and Haim Grebel, "Raman Spectrum of Graphene Coated Nano-Holes," *MRS Symposium Proceedings*, vol. 1059, pp. 26-29, 2008.

To my husband, Sumit Chakraborty for his support and encouragement
and
my beloved son, Soumil R. Chakraborty for his beautiful smile and unconditional love

ACKNOWLEDGMENT

Many people have assisted me during the course of this work. I am very grateful to my graduate advisor Prof. Haim Grebel whose inspiration and continuous guidance benefited me significantly; without his valuable and countless support, encouragement, and reassurance this work could not have been finished.

I would like to thank my co-advisor Prof. Karl D. Moeller for his moral support throughout my PhD program. Special thanks to my committee members, Prof. Leonid Tsybeskov, Prof. Gerald Whitman, Prof. Durga Misra and Prof. Andrei Sirenko for their suggestions and careful reviews of my dissertation.

In addition, I would like to thank my friends in NJIT who have given me moral support during my stay. I feel particularly grateful to Nilufa Rahim, Sugata Banerjee, Selina Akter Mala, Renita Machado, Sumana Pai, Atreyee Sinha, Ishita Biswas and Samarth Trivedi.

I am profoundly indebted to my husband, Dr. Sumit Chakraborty, for his affection, and constant support. I am also grateful to my parents to provide me such an opportunity.

I would like to thank my one year old son, Soumil R. Chakraborty, for keeping me stress-free during the most difficult time.

TABLE OF CONTENTS

TABLE OF CONTENTS
(Continued)

LIST OF FIGURES

Figure   **Page**

Figure **Page**

LIST OF TABLES

LIST OF SYMBOLS

a	Lattice Constant
δ	Nearest Neighbor Vector
B	Reciprocal Lattice Vector
k	Momentum
K	Dirac Point
t	Nearest Neighbor Hopping Energy
v_F	Fermi Velocity ($\sim 10^6$ m/s).
m*	Effective Mass
E_F	Fermi Energy
A(E)	Area in the k Space
n	Electron Density
k_F	Fermi Momentum
ρ (E)	Density of States Near Dirac Point
μ	Mobility
C_G	Conductance
V_G	Gate Voltage
σ	Conductivity
h	Plank constant (6.63×10^{-34} m^{2}kg/s
n_{imp}	Concentration of Charged Impurity
n*	Residual Carrier Density
x	Dielectric Constant

C_o^{RPA}	Normalized Voltage Fluctuation Constant
T_{opt}	Optical Transmittance
α	Fine Structure Constant
G_o	Universal Conductance
c	Speed of Light
$\Delta\omega$	Raman Shift
λ	Wavelength of Light
k_x	Propagation Constant of a Surface Wave
k_o	Propagation Constant of an Incident Beam
g	Periodicity of Metal Screen
ε_o	Dielectric Constant of Air
ε_m	Dielectric Constant of Metal
$\mathbf{G}$	Reciprocal Lattice Vector of Holes
β	Wavevector
q	Integer
n_{eff}	Effective Index of surface Waveguide
$\mathbf{K}$	Phonon Wavenumber
I_{ds}	Drain to Source Current
V_{ds}	Drain to Source Voltage
I_{cell}	Current Between Zn and Cu Electrodes
E_{cell}	Voltage Between Zn and Cu Electrodes
V_{bias}	Bias Voltage
$V_{G\text{-}Cu}$	Voltage Between Graphene and Cu Electrodes

$V_{G\text{-}Zn}$	Voltage Between Graphene and Zn Electrodes
R_L	Load Resistance
V	Potential Drop Across the Boudary
η	Phase Boundary Potential
a_a and a_c	Reaction Coefficient
R_{eff}	Effective Resistor Value
β	Propagation Constant
f	Focusing Length
G^{max}	Maximum Gain
γ	Gain Coefficient
l_g	Thickness
g_{ss}	Normalized Small Gain Coefficient
I	Pump Laser Intensity
I_s	Saturation Intensity
D	Spot Size
K_d	Dissociation Constant

CHAPTER 1

INTRODUCTION

Carbon has been extensively studied in various forms. Some of these are; three-dimensional (3-D) diamond, three dimensional layered structure of graphite, folded 1-D carbon nanotubes and more recently, as a 2-D monolayer of graphite or graphene [1]. Graphene has exhibited remarkable properties, such as, large thermal conductivity, mechanical robustness, chemical inertness and outstanding electronic properties, such as high mobility [2-5]. Several techniques are used to lay down graphene: mechanical cleavage of highly oriented pyrolitic graphite (HOPG) followed by transfer of a few layers to a substrate; peeling off surface layers of HOPG using scotch tape and transferring them to a substrate by subsequent taping (often resulting in ribbons and terraces); exfoliation and dry contact transfer (DCT) technique; epitaxial growth on single-crystal silicon carbide substrates, and reduced form of graphene oxide, which may be applicable for flexible substrates [2-8]. While, no doubt these techniques were essential to the study of graphene's properties, they resulted in layered structures, which were somewhat hard to control and rather limited in area covered. In addition, very large scale integrated (VLSI) film technology calls for lithography patterning steps, which involve photoresists. On the nano-scale, these photoresist materials are hard to remove and have a deleterious effect on free carriers' mobility within the graphene layer.

Identifying the layout of graphene as the major stumbling block for the realization of graphene-based devices, a simple mechanical technique for its deposition has

been proposed and carried out during this project. In this process, lines of graphite were drawn by exfoliating HOPG on virtually any substrate. As-is written films consist of a multi-layered graphite in a form of connected islands. A few layered graphene (one to four layers) are obtained by post annealing and sonication of these graphitic layers. It is shown in later chapters that highly crystalline films can be obtained from this innovative technique (on solid and perforated substrates alike). As stated above, such a technique minimizes the use of lithographic methods as well.

The ability to fabricate free-standing graphene layers leads to new applications in electronic, optoelectronic, bio-chemical and electro-chemical areas. The following chapters will discuss several applications- graphene based field effect transistors, graphene based surface Plasmon laser, graphene based battery and graphene based bio-detectors.

Chapter 2 provides a brief overview of graphene, discusses various properties of graphene, describes various growth techniques and confers potential applications.

In Chapter 3, various experimental methods for substrate fabrication of graphene, graphene deposition and related characterization techniques are discussed.

Chapter 4 presents simulations and theoretical consideration of infrared screens and graphene coated AAO. In Chapter 5, various applications of graphene are described. These applications include graphene based transistors, batteries, bio-chemical and optoelectronic devices. Conclusions are given in chapter 6 and future work is suggested in chapter 7.

CHAPTER 2

GRAPHENE

2.1 Overview

Two dimensional (2-D) graphene is a well-known crystallographic form of carbon with sp^2-hybridized bonds. It is the building block of many important allotropes: it can be stacked into 3-D graphite, rolled into 1-D nanotube and is the basis of 0D fullerenes [Figure 2.1]. The 2-D monolayer structure of carbon atoms had been previously considered thermodynamically unstable as a free standing film and, thus a crystallographic form which does not to exist. Recently, it has been demonstrated that graphene can be deposited on solid substrates [2-8]. Since 2004, graphene has been extensively studied both theoretically and experimentally. It exhibited remarkable properties including large thermal and electrical conductivity values and mechanical robustness.

Studies of graphite have been conducted for quite some time [9]. During 2004/2005, A.K. Geim and K. S. Novoselov at Manchester University, first isolated single and few-layered graphene [5] for which they received the 2010 Nobel Prize for Physics. The resulting single and few layered flakes were attached to a substrate by van der Waals forces [Figure 2.2]. Free standing samples were made by simply etching the substrate off and letting the graphene be held by its edges [10].
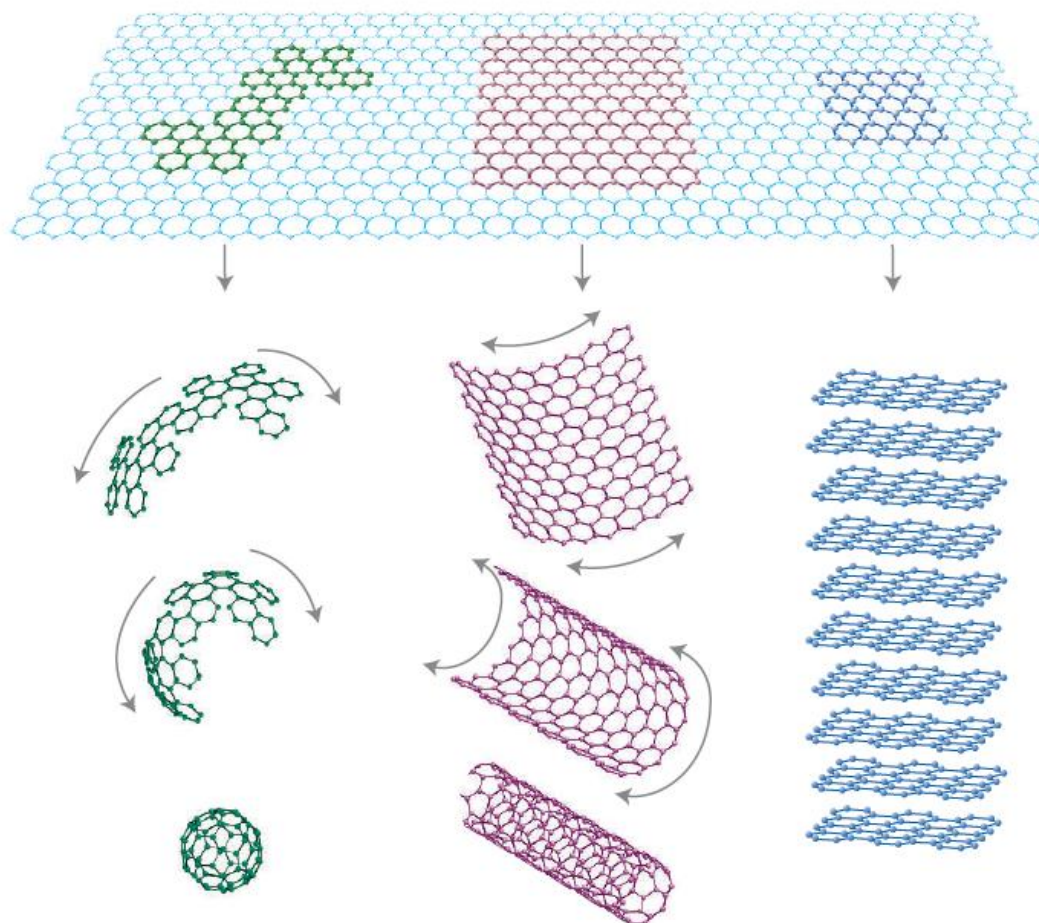
Figure 2.1 Various morphologies which may be realized with graphene [1].

After isolating mono and few layer graphene, many of its properties were revealed, including ambipolar field effect transistor [11], quantum Hall effect at room temperature [12-17], extreme high carrier mobility [18-20] and detection of single molecules [21-22]. These unique properties made graphene a very attractive field of current interest. These properties also led scientists to believe that graphene may be a key future component of high-speed logic devices, ultra-sensitive sensors, transparent electrodes for displays and solar cells and unique thermally and electrically conductive composites.
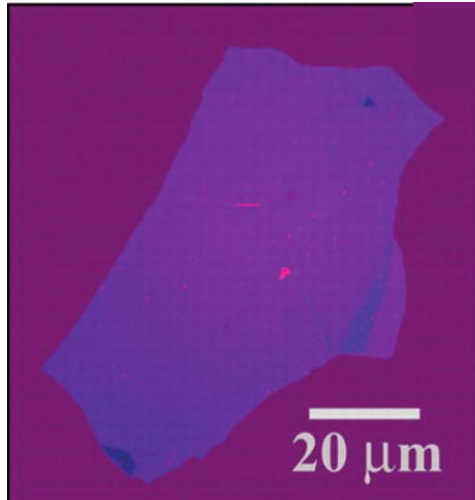
Figure 2.2   Single layer graphene, first demonstrated by A. K. Geim and K. S. Novoselov at Manchester University in 2004 [5].

2.2 Properties of Graphene

2.2.1 Atomic Structure

The distance between two adjacent layers in multi-layered graphene is 0.34 nm along the (002) direction as viewed by X-Ray diffraction. The carbon-carbon sp^2 bond in graphene is 0.142 nm long. Graphene in solid form has a density of more than 1g/cm^2.

The atomic structure of single layered graphene is generally studied using transmission electron microscopy (TEM) where graphene layeres are generally suspended between two bars or metal grids [23]. Graphene has been successfully studied on SiO$_2$ substrates using scanning tunneling microscopy (STM) [24]. In both cases, the diffraction pattern exhibits the hexagonal structure of graphene [Figure 2.3] with some ripples in the otherwise flat graphene sheets.
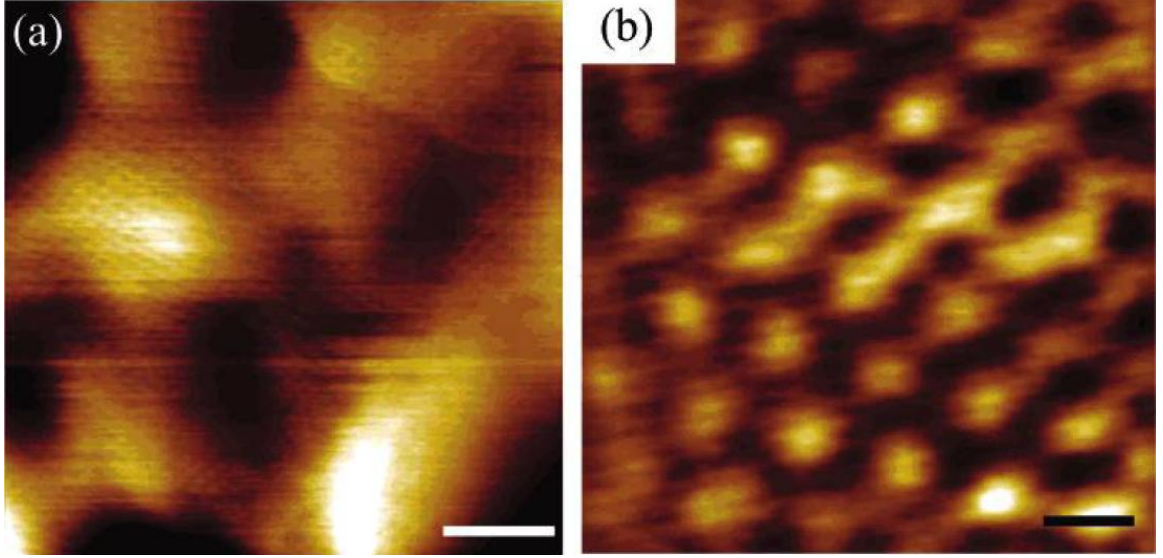
Figure 2.3 (a) STM image of monolayer graphene, (b) Atomically resolved image using STM [24].

2.2.2 Electronic Properties

Graphene is an array of carbon atoms arranged in a honeycomb structure. One can simplify its lattice structure by considering two triangular sub-units. As depicted in Figure 2.4a, the lattice vectors are a_1 and a_2, where,

$$a_1 = \frac{a}{2}(3, \sqrt{3}); \quad a_2 = \frac{a}{2}(3, -\sqrt{3}) \tag{2.1}$$

where a is the lattice constant and equals to 1.42 Å. The three nearest neighbor vectors are:

$$\delta_1 = \frac{a}{2}(1, \sqrt{3}), \quad \delta_2 = \frac{a}{2}(1, -\sqrt{3}) \text{ and } \delta_3 = -a(1, 0) \tag{2.2}$$

From Figure 2.4b it is evident that the reciprocal lattice vectors are b_1 and b_2, written as:

$$b_1 = \frac{2\pi}{3a}\left(1, \sqrt{3}\right), \; b_2 = \frac{2\pi}{3a}\left(1, -\sqrt{3}\right) \tag{2.3}$$

The corners of the Brillouin zone, the two points denoted by K and K' [1], are known as Dirac points. These points can be represented by two vectors:

$$K = \left(\frac{2\pi}{3a}, \frac{2\pi}{3\sqrt{3}a}\right) \text{ and } K' = \left(\frac{2\pi}{3a}, -\frac{2\pi}{3\sqrt{3}a}\right) \tag{2.4}$$

(a)   (b)
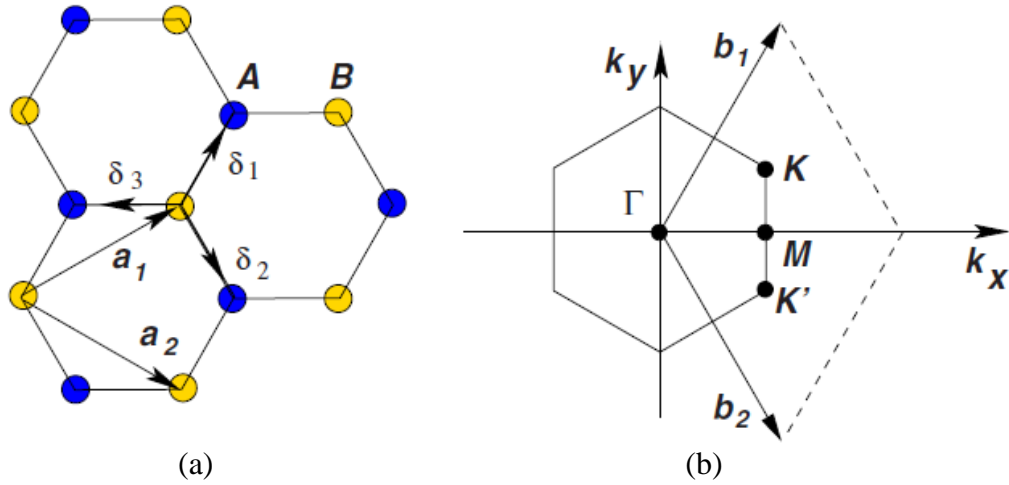
Figure 2.4 (a) Lattice structure of graphene, (b) first Brillouin zone of graphene [1].

The energy band diagram, derived by P. R. Wallace in 1947 [6] is written as

$$E_{\pm}(\mathbf{k}) = \pm t \sqrt{3 + f(\mathbf{k})} - t'f(\mathbf{k}). \tag{2.5}$$

where $\mathbf{k}$ is the reciprocal wavevector, $t \approx 2.8$ eV is the nearest neighbor hopping energy

when hopping is made within the same sub-lattice unit, and t'≈ −0.1 eV is the nearest neighbor hopping energy when hopping is made between different sub-lattices and

$$f(\mathbf{k}) = 2\cos(\sqrt{3}\,k_y a) + 4\cos(\sqrt{3}/2\ k_y\, a)\cos(3/2\,k_x a). \qquad (2.6)$$

It is evident from Equation (2.5), that the spectrum around the Dirac point is symmetric if t` = 0. It is asymmetric for any finite values of t`. The dispersion around the Dirac points (**K**, **K'**) can be obtained by an expansion, **k** = **K**+**q**; where q is an infinitesimal change in momentum around Dirac point.

From Equations (2.4) - (2.6), writing for the electron momentum near the Brillion zone corner, **K**, **k**= **K**+**q** and assuming |**q**| ≪ **K**) one can write,

$$E_{\pm}(\mathbf{q}) = \pm v_F\,|\mathbf{q}| + O[\frac{q}{K}]^2 \qquad (2.7)$$

where v_F is the Fermi velocity (~10^6 m/s), a constant.
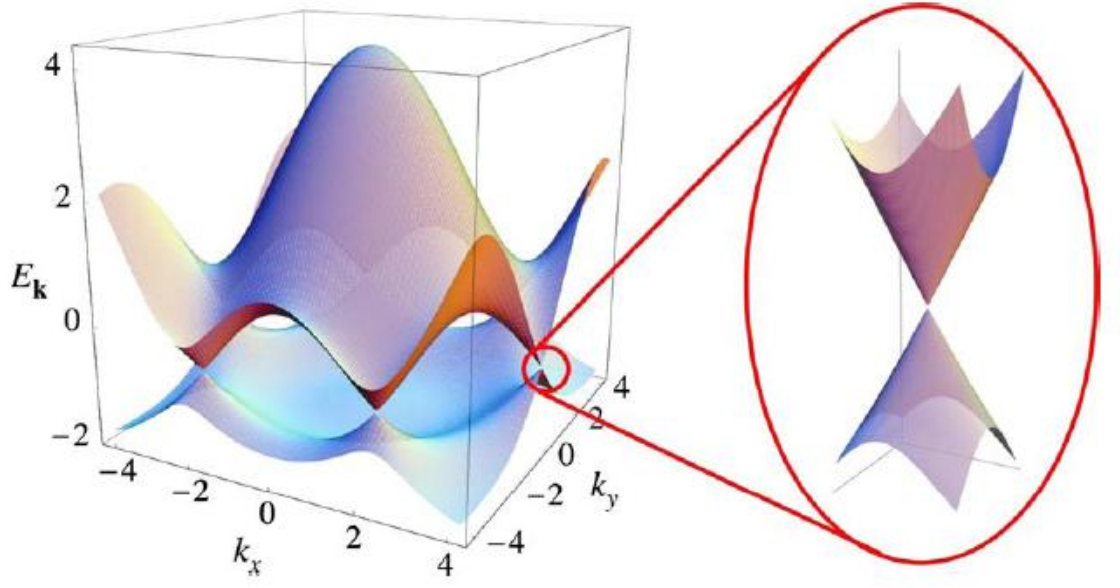
Figure 2.5 Left: Energy spectrum of graphene, right: zoomed in band diagram at Dirac point [25].

It is evident from Equation (2.7) that the velocity of the free carriers in graphene near the Brillion Zone corners (the so called Fermi velocity) does not depend on their energy. Generally, the velocity of such particles is derived from the kinetic energy as, $v = k/m = \sqrt{(2E/m)}$, which clearly exhibits nonlinear dependence on the particle's energy. The energy dispersion at Equation (2.7) resembles the energy of a relativistic particle, and therefore, may be described by the massless Dirac equation [25].

The effective mass in this case:

$$m^* = \frac{1}{2\pi} \left[\frac{\partial A\,(E)}{\partial E} \right]_{E=E_F} \tag{2.8}$$

where E_F is the Fermi energy and $A(E)$ is the area in the **k**- space

$$A(E) = \pi q(E)^2 = \pi \frac{E^2}{v_F{}^2} \qquad (2.9)$$

The electronic density n is related to Fermi momentum, k_F as $k^2{}_F/\pi = n$. By combining Equations (2.8) and (2.9), the effective mass is given by

$$m^* = \frac{E_F}{v_F{}^2} = \frac{k_F}{v_F} = \frac{\sqrt{\pi}}{v_F}\sqrt{n} \qquad (2.10)$$

Using Equation (2.7), the density of energy states near Dirac point is [1]

$$\rho(\varepsilon) = \pi q(\varepsilon)^2 = \pi \frac{E^2}{v_F{}^2} \qquad (2.11)$$
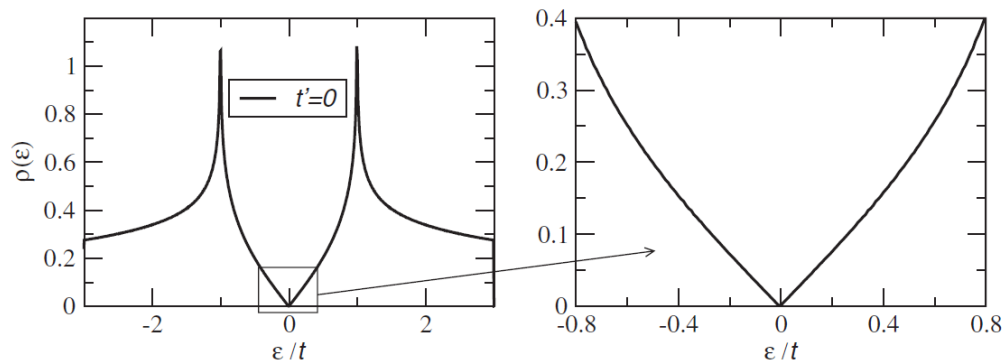
Figure 2.6   Density of states per unit cell as a function of energy (in units of t). Also shown is a zoom-in of the density of states close to the neutrality point of one electron per site [1].

Graphene has remarkably high electron mobility. For intrinsic graphene at room temperature, the mobility is calculated as 200, 000 cm^2/V·s [13] while measured value is

only 15,000 cm^2/Vs [26]. The measurement of mobility value typically makes use of a field effect transistor (FET) construction where the current in the graphene channel is controlled by a gate electrode. A general practice is to calculate the mobility, μ from the derivative of the conductance with respect to the gate voltage, which

$$\frac{1}{C_G}\frac{\partial \sigma}{\partial V_G} = \mu + V_G\frac{\partial \mu}{\partial V_G}. \tag{2.12}$$

However, this approach does not take into consideration impurities. Empirically, the Dirac points are exhibited by the minimum in the curve for the conductance vs. the gate voltage. In that case, a shift in the curve may be related to the mobility as [27, 28].

$$\mu = \frac{\sigma - \sigma_{min}}{C_G - (V_G - V_{G-min})} \tag{2.13}$$
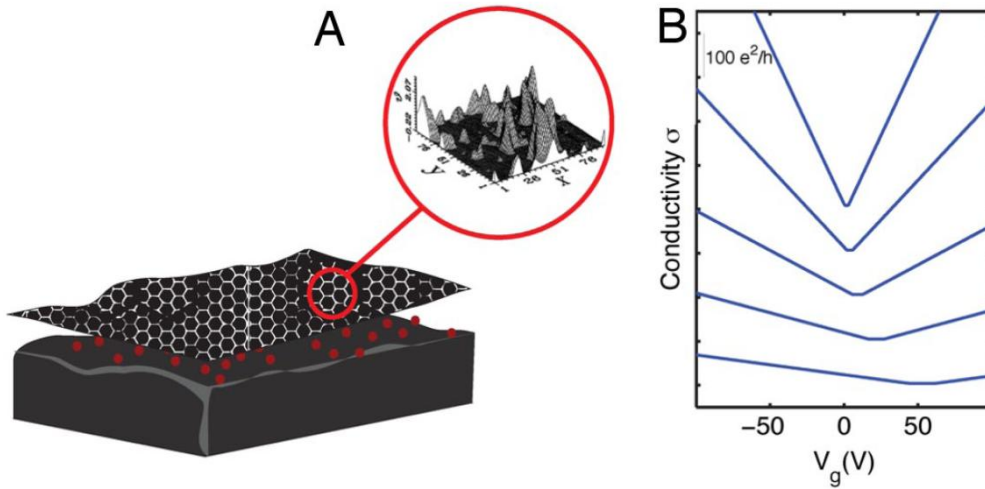
Figure 2.7   (A) schematic of graphene with charge puddles. (B) Conductivity of graphene for various concentration of charge impurity, n_{imp} [29].

The impact of charge impurities is more profound in graphene then for bulk material. These impurities create inhomogeneous potential fluctuations, which in turn generates electron-hole puddles. Such local charge distributions are thought to be responsible for the observed finite conductivity at the Dirac points, as well [29]. The concentration of charged impurity, n_{imp} is 250-400 x 10^{10} cm^{-2} for unclean samples for which the value for the minimum conductivity is $4e^2/h$. Cleaner samples exhibit even larger minimum conductivity values; for example, when the concentration of charge impurities reaches 20 x 10^{10} cm^{-2}, the minimum conductivity becomes $8e^2/h$ [17].

The concentration of charge impurity, n_{imp}, may be expressed as,

$$n_{imp} = \frac{n^*}{2r_s^2 . C_0^{RPA}} \qquad (2.14)$$

where n* is the residual electron density. n* determines the conductivity of graphene on a dielectric. Here, $r_s = (2e^2)/[hv_F x)$, where x is the dielectric constant. C_o^{RPA} is the normalized voltage fluctuation constant [17].

Mobility of graphene with impurities may be written as [17],

$$\mu = 50\,\mu_0\,\frac{n_o}{n_{imp}} \qquad (2.15)$$

where $\mu_0 = 1m^2/Vs$ and $n_o = 10^{10} cm^{-2}$.

2.2.3 Mechanical Robustness

Elastic properties of intrinsic monolayer graphene were measured by atomic force microscopy (AFM) [30, 31]. In these cases, monolayer graphene was laid suspended over micron size holes [Figure 2.8]. Graphene is 200 times stronger than steel under similar conditions [30]. The breaking strength (intrinsic strength of a defect free sheet) of single layer of graphene is reported to be 42 Nm^{-1}, with a tensile strength of 130 GPa. Its Young's modulus is 1 TPa establishing graphene as one of the strongest materials on Earth.
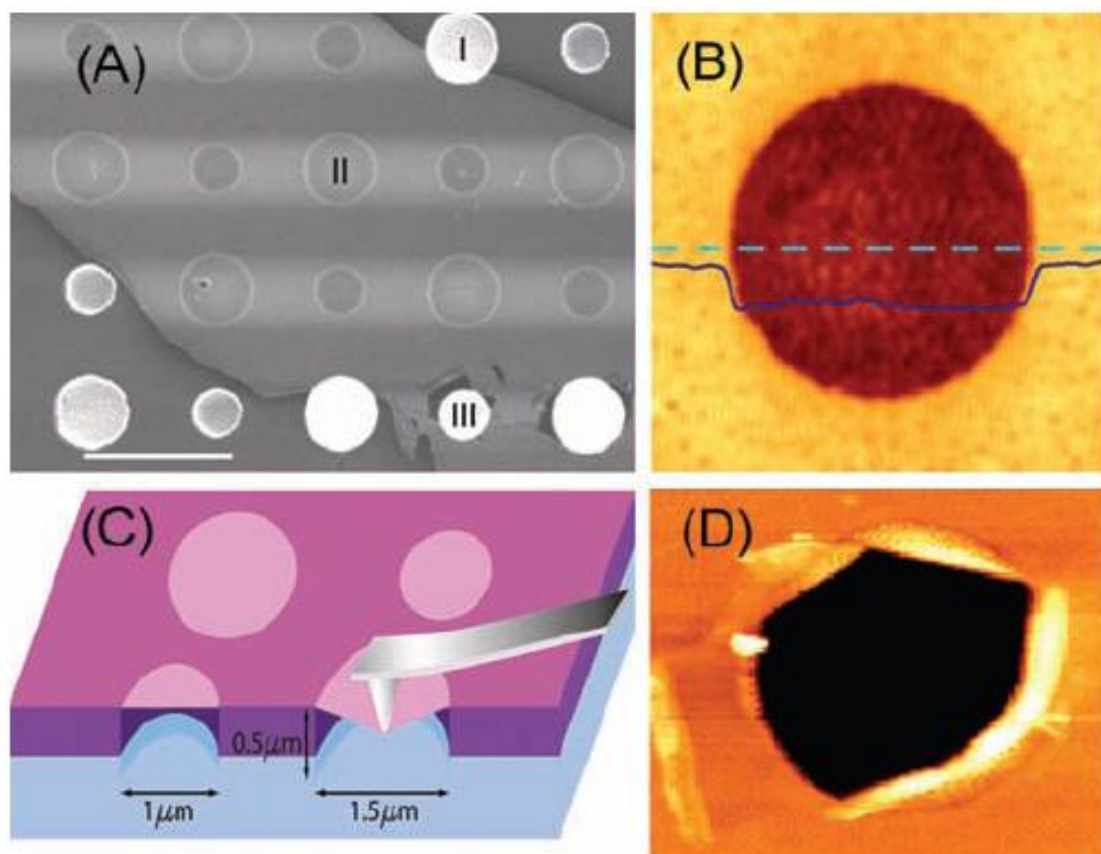
Figure 2.8 (A) Scanning electron microscope picture of suspended graphene, (B) atomic force microscope picture of single whole covered with mono layer graphene in a non contact mode, (C) schematic diagram of graphene coated holes and (D) ruptured graphene membrane over a hole [31].

Thus, one could consider strong a graphene paper for electro-mechanical application [32]. Commercialization is a future goal.

2.2.4 Optical Properties

Graphene is optically transparent for photon energies between 0.1 and 0.6eV [33]. Optical transmittance of a free standing monolayer graphene is expressed as T_{opt} [33].

$$T_{opt} = (1 + \frac{\pi\alpha}{2})^{-2} \approx 1 - \pi\alpha \approx 0.977 \qquad (2.16)$$

where α is the fine structure constant, $e^2/\hbar c$.
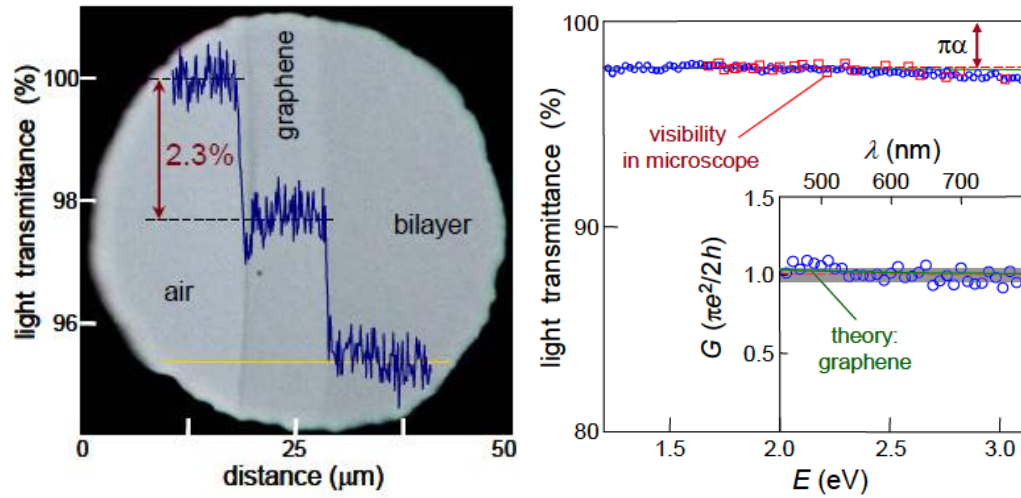
Figure 2.9 (a) White light transmission through mono and bilayer graphene, (b) Transmission spectrum of graphene in near infrared to violet light. The red line is the opacity of $\pi\alpha$. The inset graph shows the conductance of graphene in visible light, calculated from the measured T_{opt} [34].

The optical conductance of graphene due to optical interband transition is almost independent of frequency and determined by universal conductance value of $G_0 = e^2/4\hbar =$

6.08 x $10^{-5}\Omega$. It has been reported that the conductance, G, varies between 1.01 to 1.04 of the G_0 [34].

2.3 Growth Techniques

The growth techniques of graphene may be divided into basically three categories: 1. mechanical exfoliation, 2. epitaxial growth on silicon carbide (SiC) and 3. chemical vapor deposition (CVD).

2.3.1 Mechanical Exfoliation

This method was first developed by the Geim and Novoselov group in 2004. Using highly ordered pyrolitic graphite (HOPG), mono and few layer graphene were deposited on Si-SiO$_2$ substrates at sizes of approximately 10 μm^2 [5]. Graphene layers were cleaved from the HOPG by pressing a scotch tape on it and transferring the layers to the substrate. This is a simple and inexpensive method. However, reproducibility and large scale manufacturing is a challenge.
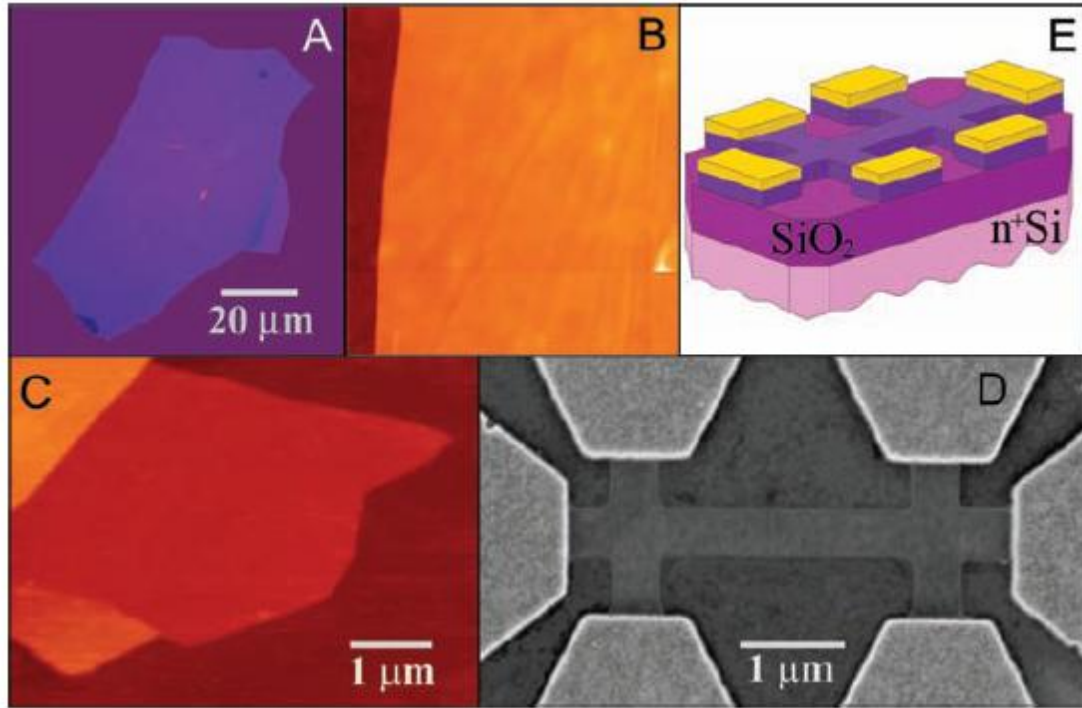
Figure 2.10 (A) Photograph of mono layer graphene deposited on Si-SiO$_2$ substrate, (b) AFM picture of the sample, (C) another view of the sample, (D) scanning electron microscope(SEM) image of the experiment where graphene was deposited between metal structures and (E) schematic view of the metal structure [5].

2.3.2 Epitaxial Growth on SiC

The possibility of large integrated electronics on SiC-epitaxial graphene was first proposed in 2004 [35, 36]. In this method, mono and few layer graphene films have been produced by thermal decomposition of silicon carbide at very high temperatures at ultra-high vacuum. In this method, very high quality large area graphene has been produced. The main drawback of this method is the high cost of fabrication.
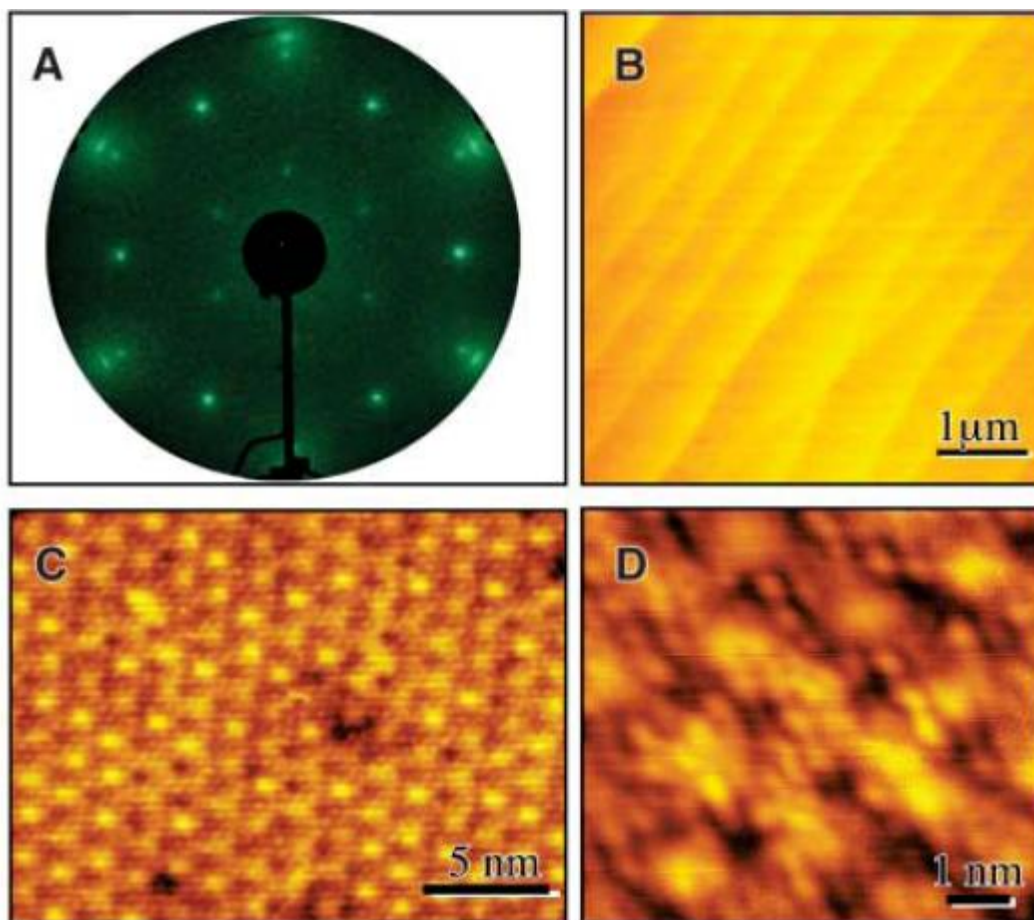
Figure 2.11 (A) LEED pattern of 3 layer graphene grown on SiC substrate, (B) AFM picture of the sample, (C) STM image of mono layer graphene (D) graphene- SiC interaction at their interface [23].

2.3.3 Chemical Vapor Deposition (CVD)

Large area growth of graphene is desirable for many applications and yet very challenging to obtain. Many efforts have been made to get macro size graphene films. Some of these attempts involve high temperature treatment, as well. These methods are as useful as the chemically reduced graphene films in the sense that the films may be transferred to any substrate according to need. The epitaxial method produces graphene by removing silicon atoms from silicon carbide wafers [37-39]. Graphene films were also

made on nickel [40] as well as copper sheets [41] using the metals as catalysts. The graphene films were then transferred to other substrate by using an adhesive polymeric layer. Graphene was also made from chemically reduced graphene oxide (GO) [42, 43].

Chemical vapor deposition (CVD) is also known as vapor-phase epitaxy (VPE). CVD is a process whereby an epitaxial layer is formed by a chemical reaction between gaseous compounds. CVD can be performed at atmospheric pressure (APCVD) or at low pressure (LPCVD).

The mechanism of CVD involves a number of steps: a) the reactants (gases or dopants) are transported to the substrate surface; b) they are transferred to the substrate, where they are adsorbed; c) a chemical reaction occurs, catalyzed at the surface, followed by growth of the epitaxial layer; d) the gaseous products are de-absorbed into the main gas stream; and e) the reaction products are transported out of the reaction chamber.

Scalable growth of free-standing graphene wafers with copper (Cu) catalyst on SiO_2/Si substrate at low temperature has been reported [44]. The Cu is the most common and the cheapest catalyst among electronic materials. This process for producing the graphene with the Cu is based on a low-pressure, fast-heating chemical vapor deposition method.

Similar methods have been developed to produce wafers of high-quality graphene films. Upto 3 inch film on nickel (Ni) was produced under ambient pressure and then was transferred onto arbitrary substrate through instantaneous etching of metal layers [45-47]. In those methods, the silicon substrate is covered with SiO_2 and capped with an electron-beam evaporator deposited copper or nickel film, which serves as the catalyst for carbon precursor decomposition. Methane is used as the carbon precursor in this method.

Three key parameters of CVD growths in this case are the growth temperature, time, and the post-growth cooling rate which allow the reproducibility of fabrication of single layer graphene larger than 100 m^2.
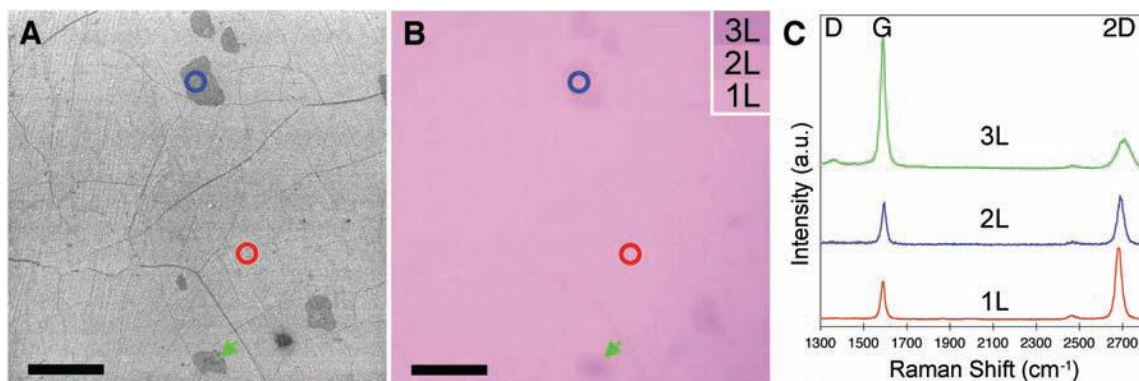
Figure 2.12 (a) graphene grown by chemical vapor deposition, (b) another view of graphene, (c) Raman spectra of mono and few layer graphene [41].

After deposition of the graphene layer, etching of the metal (Ni or Cu) and transferring graphene to another substrate is important for further device processing. In case of CVD using nickel precursor, nickel can be etched by strong acids such as nitric acid (HNO$_3$) or ferric chloride (FeCl$_3$) solutions [41]. Copper is generally etched using aqueous solution of iron nitrate [40]. There are two well established methods to remove graphene from the solution- (1) after metal is dissolved, a substrate is brought into contact with the graphene film and it is pulled from the solution; (2) the surface of the graphene –on-metal is coated with polydimethylsiloxane (PDMS) or poly-methyl methacrylate (PMMA) and after the metal is dissolved the PDMS/ PMMA-graphene is lifted from the solution [40, 41].

2.4 Applications

2.4.1 Graphene Transistors

The large mobility of graphene make it attractive for electronic applications. In 2004, the Manchester group demonstrated the first grapahene transistor [6]. In 2006, the Georgia Tech researchers introduced the first planar FET with side gates [48]. In 2009, researchers of Politechnico di Milano, demonstrated logic gates using graphene [49]. During the same year, a group from the Massachusetts Institute of Technology in the USA built a frequency multiplier, one that is capable of taking an incoming electrical signal of a certain frequency and producing an output signal that is a multiple of that frequency [50].
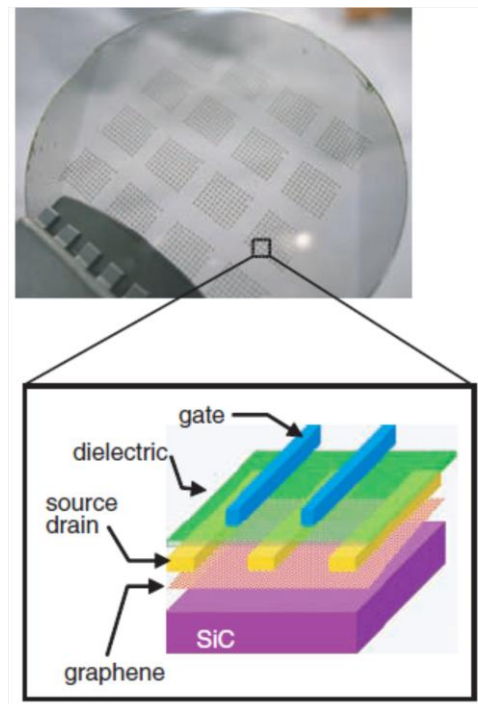
Figure 2.13 Graphene FET grown on 2 inch wafer and schematic cross-sectional view of top- gated graphene FET [50].

Recently in 2010, a group at IBM reported that they have fabricated the fasted graphene transistors, which may reach 100 GHz [51]. Though graphene transistors have very poor on-off ratio and overall low current (which is unattractive for memory applications), many researches are committed to graphene based transistors and to improve its functionality.

2.4.2 Conducting and Transparent Electrodes

High electrical conductivity and optical transparency make graphene a suitable candidate for transparent electrodes. These electrodes are important for touch screen, liquid crystal displays, organic photovoltaic cells, organic light emitting diodes and solar cells. Currently, indium tin oxide is used for these tasks. This material is brittle and expensive. Large-area, continuous, transparent, and highly conducting few-layered graphene films were produced by chemical vapor deposition and used as anodes for photovoltaic applications. A power conversion efficiency (PCE) up to 1.71% was demonstrated, which is 55% of the PCE value for an indium-tin-oxide based control device [52].

2.4.3 Graphene Nanoribbons

Graphene nano- ribbon (GNR), consists of thin strips of graphene. The GNR was first introduced theoretically by Mitsutaka Fujita [53]. The electronic states of GNR depend on the edge morphology. The edge could be either armchair or zigzag. Zigzag GNRs are always metallic while armchairs can be either metallic or semiconducting, depending on their width. Calculations show that armchair nanoribbons are semiconducting with an energy gap scaling with the inverse of the GNR width. Recent experimental data supports

that notion [54]. GNR has been fabricated by Scanning Tunneling Microscope (STM) lithography [55]. The unique two-dimensional structure, high electrical and thermal conductivity, and low noise make GNR a possible alternative to copper for integrated circuit interconnects. Because of its semiconductive properties, it is a potential technological alternative to silicon semiconductors and possible channels for field effect transistors (FETs) which are less than 10 nm wide and with an I_{on} / I_{off} ratio greater than 10^6 at room temperature.

2.4.4 Ultra-Capacitors

Ultracapacitors are electrical energy storage devices that store and release energy by nanoscopic charge separation at electrochemical interface between an electrode and an electrolyte [56]. The stored energy is inversely proportional to the thickness of the double layer of the capacitor. These capacitors may store very high energy density compared to the so called dielectric capacitors. The capacitors are able to store large amount of charge, which can then be delivered at a higher rate than rechargeable batteries. Ultracapacitors are popular for their unique properties, such as, high power storage, long life, low maintenance, low weight, flexible packaging and wide temperature operating range.

An ultracapacitor may be composed of two porous carbon electrodes that are isolated from one another by a porous separator that prevents electronic discharge. A variety of porous forms of carbon are currently preferred as the electrode materials because they have exceptionally high surface areas, relatively high electronic conductivity, and acceptable cost [57]. Metal foils or carbon impregnated polymers are used to conduct electrical current from each electrode. The separator and the electrodes

are filled with electrolytes, which allow ionic current to flow between the electrodes while preventing electronic current form discharging the cell.

Instead of porous carbon electrodes, chemically modified graphene layers are now used, which provided for larger flexibility and smaller size of the capacitor. The high surface area of the electrodes increases the conductivity for such a network [58, 59]. High electrical conductivity of the graphene eliminates the need for conductive fillers, used in ultracapacitor and thus allows an increased electrode thickness. Increasing the electrode thickness and eliminating the additive leads to improve the electrode performance and the ability to store a larger energy density.
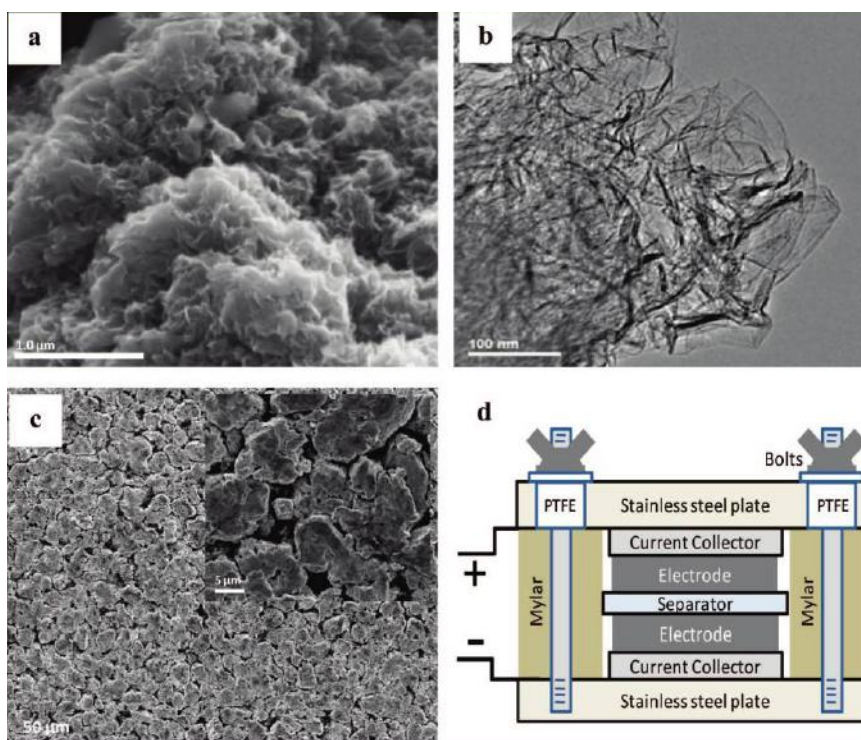
Figure 2.14 (a) SEM image of chemically modified graphene, (b) TEMimage showing graphene sheets in the chemically modified graphene substrate, (c) low and high (inset) magnification SEM images of chemically modified electrode surface and (d) schematic of ultracapacitor [56].

2.4.5 Graphene Based Bio-devices

In the last decade there has been large activity in the fields of biomedicine, bio-actuators and bio-detectors. The main issue here is reliable interfacing at the molecular and cell levels. Chemically modified graphene (CMG), with their 2-D structures and adjustable surface chemistry, may couple better than carbon nanotubes or fullerenes with biological compounds without any geometrical restrictions [60].

Graphene is a semimetal and therefore inadequate for electronic purposes unless a second gate electrode or proper doping is used. Little work has been done to date to exploit this property and detect various biomolecules [53]. Figure 2.15 shows a small molecule (DNA) and large molecule (bacteria) attached to CMG and detecting them optically.
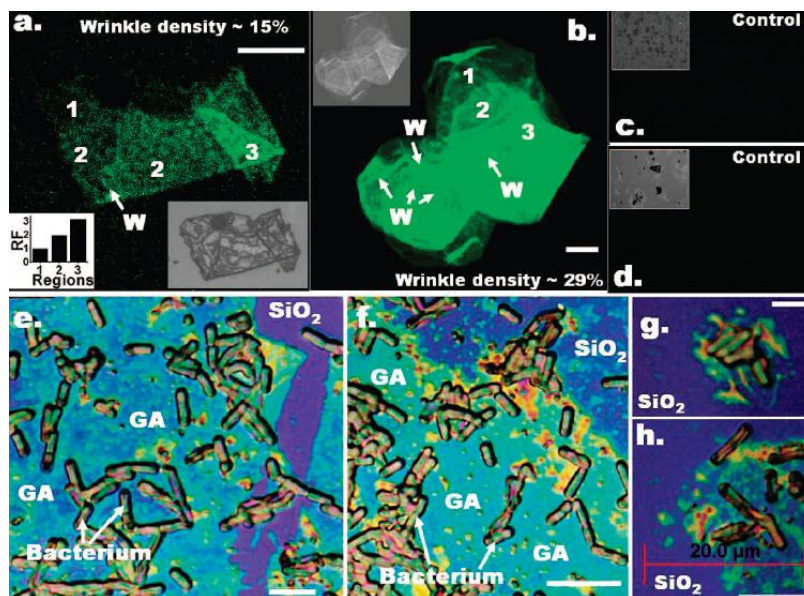
Figure 2.15 (a, b) Confocal images of florescent-labeled probe-DNA attached on graphene oxide (GO) sheets; the bottom right inset of (a) and top left inset of (b) show the optical inages of corresponding GO sheets before DNA deposition, (c, d) confocal images of no probe-DNA and no target-DNA (e, f) Microscope images showing selective attachement of bacterial cell on GO and (g, h) selective deposition of bacteria on smaller GO sheets [60].

2.4.6 Gas Sensors

The prospective use of graphene as gas sensor is a focus of many studies [61, 62]. Similarly to carbon nanotubes, graphene does not have dangling bonds. Therefore, it remains insensitive when exposed to most chemicals. On the other hand, it has inherently low electrical noise due to the quality of its crystal lattice. Since the electrical properties of graphene are largely affected by molecules residing at its interface modification of the interface may serve as a sensor. When chemically modified graphene absorbs gases, its resistivity substantially changes. For example, graphene flakes served as sensors for ammonia (NH_3), nitrogen dioxide (NO_2), carbon monoxide (CO) and water vapors (H_2O) at room temperature by mesuring their related resistivity change. These can be either single flake devices with platinum nanoelectrodes deposited by means of focused ion beam (FIB) technique, or multi-flake thin film device with interdigitated gold transducer.

CHAPTER 3

EXPERIMENTAL METHODS

In Chapter 3, various experimental methods for substrate fabrication of graphene, graphene deposition and their characterization are discussed.

3.1 Anodized Aluminum Oxide (AAO)

Anodic alumina is a self-organized nano-structure containing high density of uniform cylindrical pores that are aligned perpendicularly on the surface of the materials and penetrate through its entire thickness. A regular porous structure is formed when aluminum is electrochemically anodized in certain solutions. In general, a thin dense alumina barrier layer separates the pores from the aluminum. Dimensions of this porous structure are defined by the reaction conditions, providing a convenient way to precisely engineer the nanoscale morphology. The pore diameter is tunable from 5 nm to several hundred nm by use of different values of voltages. AAO is optically transparent, electrically insulating, thermally and mechanically robust and chemically inert. AAO processing is compatible with micro-fabrication and scalable to high volume production.

The substrates were prepared according to well-established recipe [63, 64]. High purity (99.999+%) Al foil (250 lm thick) from Sigma–Aldrich was ultrasonically cleaned in deionized (DI) water for 30 minute. Then, the Al foils were degreased in acetone for more than 24 hours. After a rinse in ethanol, the samples were electro-

polished in a mixture of ethanol, $HClO_4$ and DI water at 5 ^{o}C and 50 V to decrease surface roughness. Anodization was carried out at 5 ^{o}C and 35 V in a 0.3 M solution of oxalic acid in deionized water for 6–8 hours. Consequently, the anodic oxide layer was removed by immersing the substrate into a mixture of phosphoric (6% wt) and chromic acids (1.8% wt) maintained at 65 ^{o}C for 3 hours. The Al specimen was later anodized again for 5 minutes under the same conditions as before.
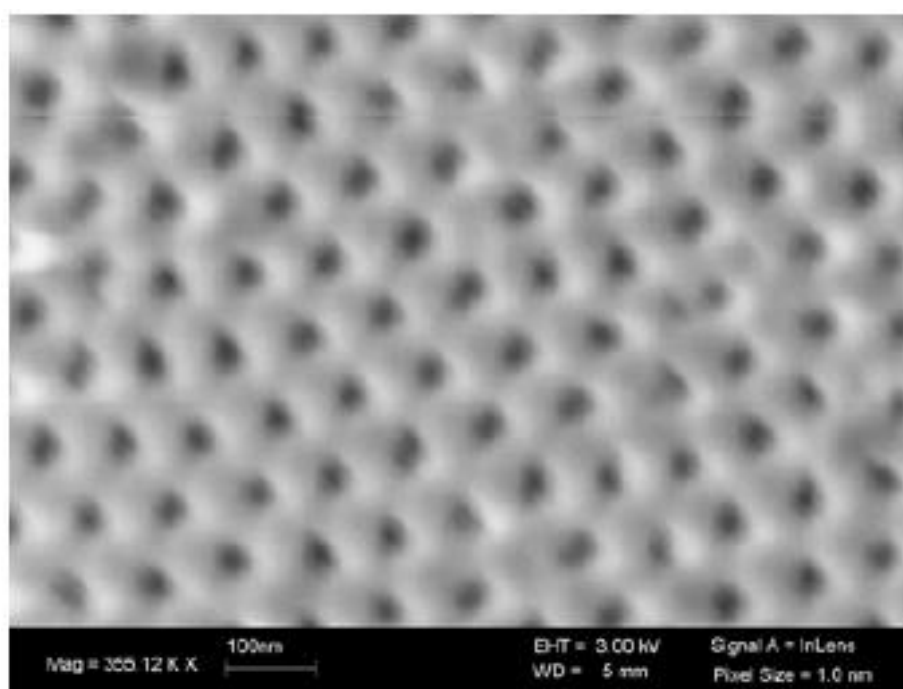
Figure 3.1 SEM picture of anodized aluminum oxide with a hole size of 20 nm.

3.2 Graphene Deposition

Here a novel, yet, simple, method to lay out stress free, graphene layers is described. The resulting films cover hundreds of micron squares.

3.2.1   Deposition Technique

The 'writing' system is schematically shown in Figure 3.2. It consisted of a 2-D translational stage on which the substrate is fixed. A second stage gently brings the HOPG ingot in contact with the substrate. The computer controlled 2-D stage is moved to create the desired feature. The resultant exfoliated graphene is inevitably irregular and comprised of small, approximately sub-micron size, islands. The substrate is then annealed at 800°C for 3 hours in 100 sccm of Argon following by sonication in ethanol to remove most of the loose particulate. This latter stage is called the thinning stage. The resultant films are then inspected by scanning electron microscope (FE-SEM), Raman (pump with 514.5 nm line of Ar laser at 20 mW, 75 cm single chamber spectrometer equipped with a cooled CCD camera at -15°C), infrared (IR) spectroscopy and in the case of deposition between electrodes, by current-voltage measurements, as well.

φ,z-axis stage

HOPG

substrate

translational stage
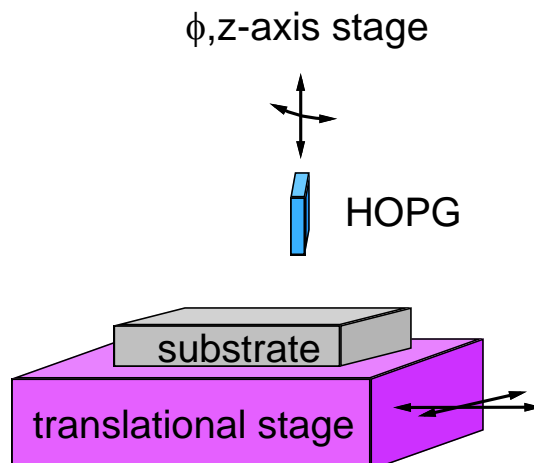
Figure 3.2   Schematic configuration of the 'writing tool': The substrate is put on a 2-D stage. The HOPG ingot is gently touching the substrate and the stage is moved to obtain the desired printed feature.

3.3 Characterization Techniques

Mono and few layer graphene have been characterized optically and physically using various methods. In this part, those methodologies are described.

3.3.1   Raman Spectroscopy

Raman spectroscopy is a spectroscopic technique to determine vibrational modes of molecules through assessment of scattered light.   The frequency shift of the scattered light with respect to the incident light alludes to the vibration frequency of the molecules.
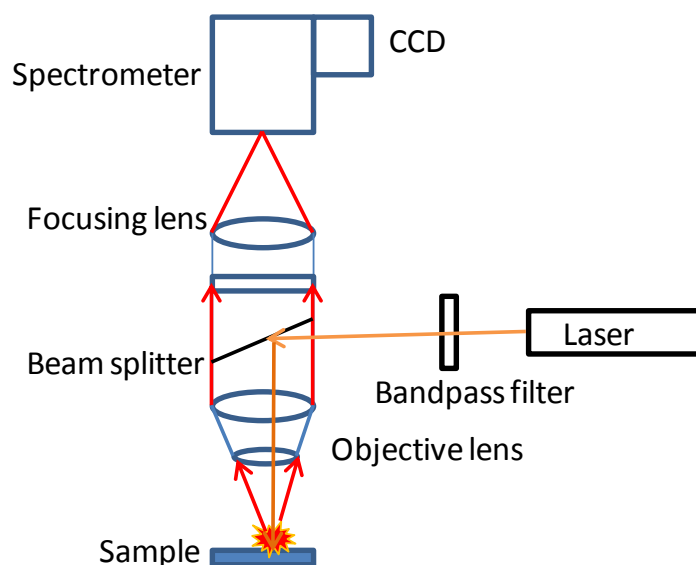
Figure 3.3   Schematic of Raman spectroscope.

In the experiment, a laser beam is focused on the sample by use of an objective lens. An optical bandpass filter ensures that only the laser frequency is used to 'pump' the sample. Scattered light from the illuminated area is collected through the same objective lens (so call confocal arrangement) and is directed onto a spectrometer [Figure 3.3]. Wavelengths close to the laser line (due to Rayleigh scattering) are filtered out by use of another optical filter, which is placed at the spectrometer entrance slit. The filtered beam is dispersed by a grating and impinges on a cooled detector array for spectral analysis.

The scattering mechanism is depicted in [Figure 3.4]. In a Stokes process, the pump laser beam excites the molecular vibrations. Energy is diverted from the pump beam thereby, upon relaxation, the scattered light is of lower frequency (lower energy) than the pump laser frequency. An anti-Stokes process consumes energy from an already excited vibrational state. Thereby, the scattered photon is of higher frequency (larger energy) than the original pump beam. In the experiments, one can

assess the frequency shift of the scattered beam. The Raman shift is typically expressed in wavenumbers,

$$\Delta\omega \text{ (cm-1)} = [1/\lambda_1 \text{ nm}^{-1} + 1/\lambda_2 \text{ nm}^{-1}] \times 10^7 \text{ nm/cm} \qquad 3.1$$
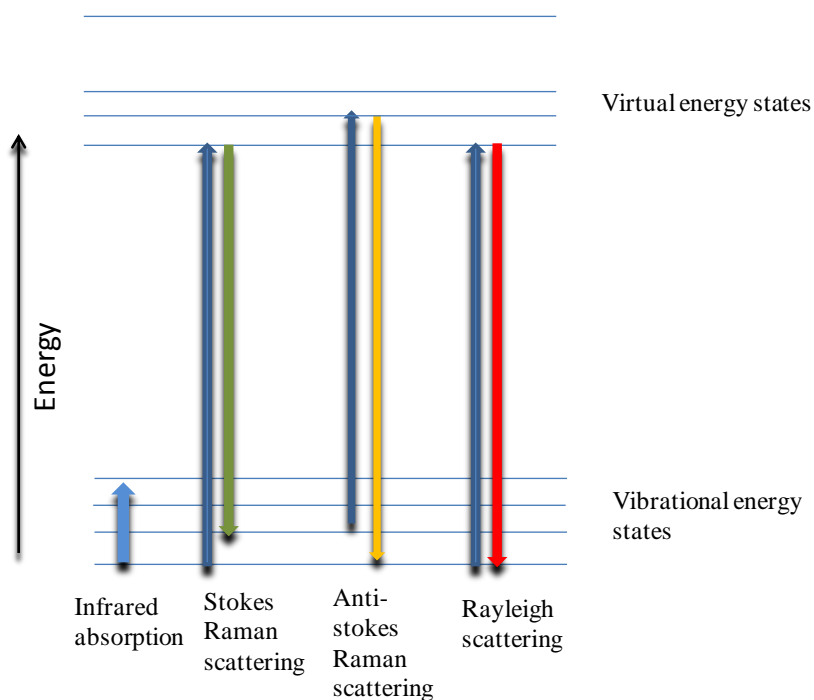
Figure 3.4 Energy level diagram showing various scattering modes of Raman signal.

3.3.2   Infrared (IR) Spectroscopy

Infrared (IR) spectroscopy deals with electromagnetic scattering and absorption by molecules in the infrared region of the spectrum. The infrared portion of the electromagnetic spectrum is divided into three regions. The near-infrared region, which is between 14000 cm^{-1} to 4000 cm^{-1}. The mid-infrared region which is between 4000 cm^{-1} to 400 cm^{-1} and far-infrared region which is between 400 cm^{-1} to 10 cm^{-1}. The most

prevalent characterization technique is based on absorption spectroscopy [Figure 3.5]. Generally a Fourier transform infrared (FTIR) spectrometer is used for the measurement.
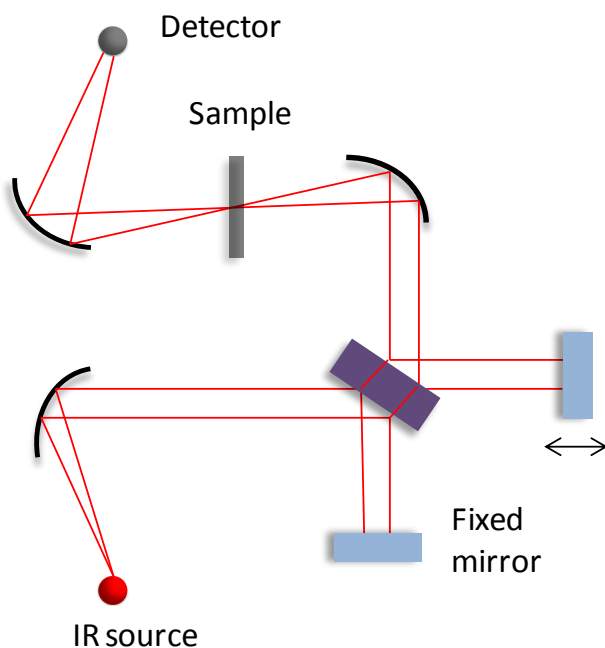
Figure 3.5 Schematic of Infrared Spectrosmeter.

Infrared spectroscopy exploits the fact that molecules absorb electromagnetic energy at specific frequencies which are characteristic of their structure. These absorptions are resonant vibrational modes. A linear molecule with N number of atoms has 3N-5 possible vibrational modes. A non-linear molecule with N number of atoms has 3N-6 degrees of vibrational mode. Simple diatomic molecules have only one bond and only one form of vibration (along the molecular axis). More complex molecules, like organic compounds, have very complex vibrational spectra, which is translated to many absorption peaks in the IR wavelength region.

3.3.3   Scanning Electron Microscope (SEM)

Scanning electron microscopes (SEM) [Figure 3.6] employ a beam of high-energy electrons to generate images of surfaces of solid sample. The signals, derived from electron scattering reveal information about the sample morphology, chemical composition and crystalline structure. In most cases data is generated as a 2-dimensional image of the sample's surface. Areas ranging from approximately from 5 μm^2 up to 1 cm^2 may be imaged using a scanning mode. Magnification ranges from 20X to approximately 30,000X with spatial resolution of 20 to 100 nm [65].

Accelerated electrons in an SEM carry significant amounts of kinetic energy. Such energy may dissipate and generate secondary electron emission. Secondary electrons are most valuable for accentuating morphology and topography of the sample's surface and backscattered electrons are most valuable for illustrating contrasts in composition of multiphase samples. SEM analysis is considered to be "non-destructive", that is, x-rays generated by electron interactions do not lead to volume loss of the sample. Thus it is possible to obtain a repeated image of the same sample.
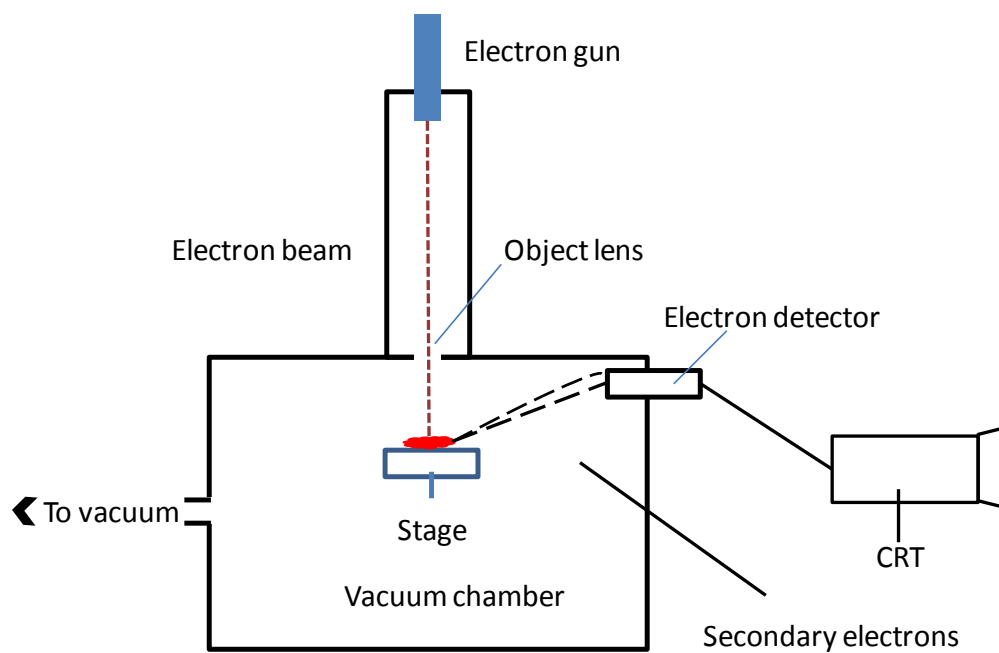
Figure 3.6 Scanning electron microscope (SEM).

CHAPTER 4

SIMULATIONS AND THEORY

In Chapter 4, simulation of graphene-coated infrared metal-mesh screens in the micrometer scale and graphene-coated nano-scale array of holes in the dielectric layer above metal substrates are described.

4.1 Infrared (IR) Screens

Freestanding metal screens or filters have been studied for short [66] and long wavelength regions [67]. Their transmittance was investigated from the invisible to the terahertz spectral region due to their important role in astronomy, in particular, infrared (IR) astronomy [68] and remote sensing. In general, these filters are able to separate desired IR signals from more energetic short wavelength radiation, allow color temperature measurements, provide order sorting for grating spectrometers, and improve the signal-to-noise ratio of Fourier transform spectrometers (FTIR). Square-shaped freestanding metal screens are commercially available and have been used as bandpass filters [69, 70], reflectors for long IR wavelengths, Fabry–Perot etalons [71], and antennas [67].

Freestanding, square shaped, electroformed copper screens were purchased from Buckbee-Mears. Those screens were 4 microns thick with periodicity of 15 microns and openings of 8 microns [Figure 4.1].
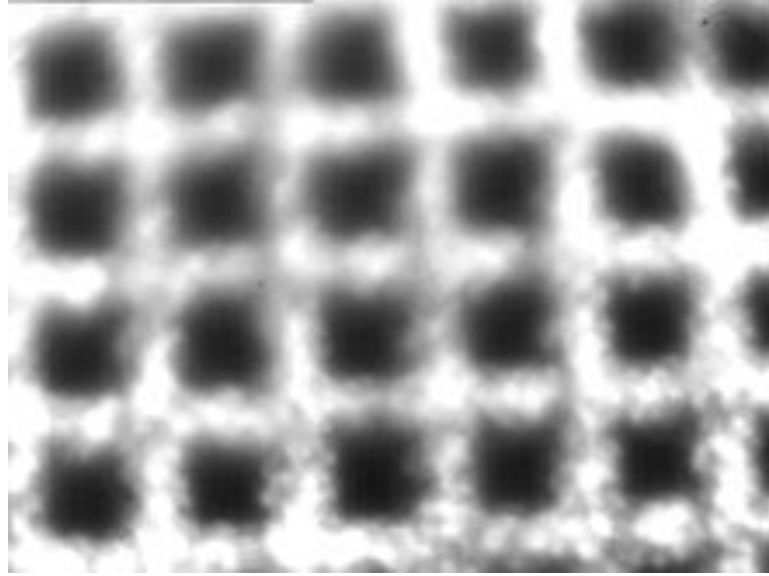
Figure 4.1 Flat metal screen: 7.6x7.6 μm^2 openings, arranged in a square lattice with a 12.7 μm pitch.

4.1.1 Theoretical Consideration

Surface plasmon polariton (SPP) waves are surface waves, propagating laterally on either of the copper screen's surfaces. The waves on each surface are coupled by waveguides modes, either propagating or evanescent, through the screen's opening. In principle, the electric field component of an electromagnetic wave may oscillate in two polarization states: *p*-polarization (electrical vector oscillating within the plane of incidence) and *s*-polarization (electrical vector oscillating normal to the plane of incidence) [72]. Only the p-polarized incident beam is effectively coupled to surface modes; the s-polarized beam is basically nullified by the local field arising from the oscillating free carriers in the metal.

An effective coupling between an incident, free space propagating beam and a surface mode takes advantage of the periodic structure of the metal mesh screen. This is made by a scattering process, which generates forward and backward surface modes. If the screen is aligned along one of its symmetry axes, the coupling process can be described by one-dimension relationship: the propagation constant of the surface wave k_s, the periodicity g of copper mesh screen and the propagation constant of the incident beam k_0 are related through, $(k_{sx})^+=k_0sin(\theta)+q2\pi/g$ and $(k_{sx})^-=k_0sin(\theta)-q2\pi/g$, with q – a positive integer. The propagation wavenumber of a surface mode that propagates on a continuous metal film is written as $k_s=k_0(\varepsilon_m\varepsilon_0/\varepsilon_m+\varepsilon_0)^{1/2}$ with ε_m, the dielectric constant of metal and ε_0, the dielectric constant of air or any other dielectric film which is situated at the metal-mesh screen's surface [67]. We assume that this relationship hold for inhomogeneous metal films (metal mesh screens), as well, if the area of the openings is relatively small. Assuming copper to be an ideal metal, its permittivity constant has a large negative real component, $\varepsilon_m<<0$, implying $k_s\sim k_0$. Therefore, the optimal coupling between a normal incident electromagnetic wave ($\theta=0$) and a surface mode occurs whenever the propagation constant of the incident beam matches the screen's periodicity g. This is also the condition that creates a surface wave resonance: the two counter-propagating surface components interfere and their standing wave pattern matches that of the screen, alternatively, we writefor normal incidence, $\boldsymbol{k}_s=(k_{sx})^++(k_{sx})^-=0$.

4.1.2   Graphenated Infrared Screen

Graphene-coated screens [Figure 4.2] have been fabricated. In the simulations, the graphene was modeled as an extremely thin conductor deposited on top of the metal-mesh copper screen.
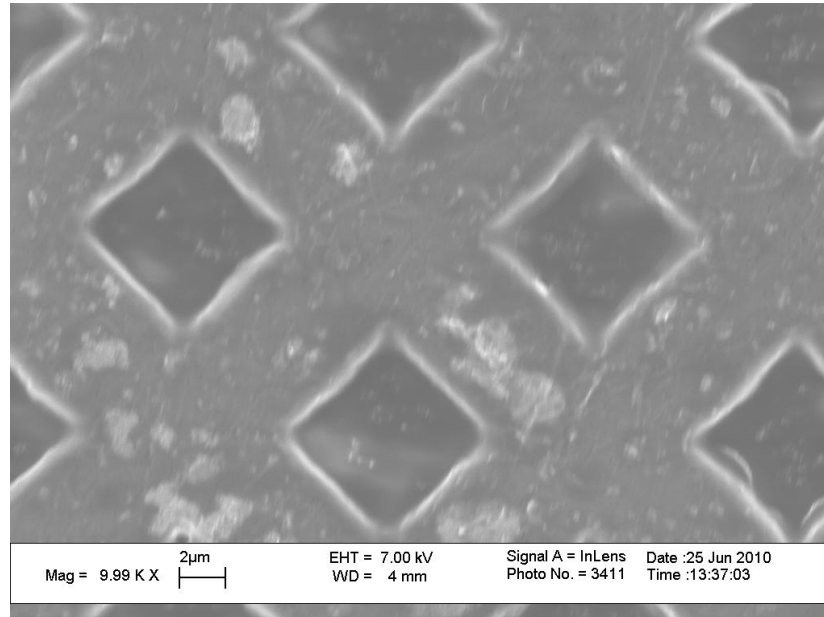
Figure 4.2 Graphene coated copper screen: 7.6x7.6 μm^2 opening, arranged in a square lattice with a 12.7 μm pitch.

Finite element software (Micro-Stripe) was used in the simulations. The peak of the electric field is positioned near the opening edge while dropping to approximately one half of its maximum value at the midst of the opening. The simulation in Figure 4.3 shows the electric field distribution at optimal coupling (resonance conditions) across an area of one opening: the electric field in the metal region is zero. The polarization of the incident electric field is along top-to-bottom in the figure.
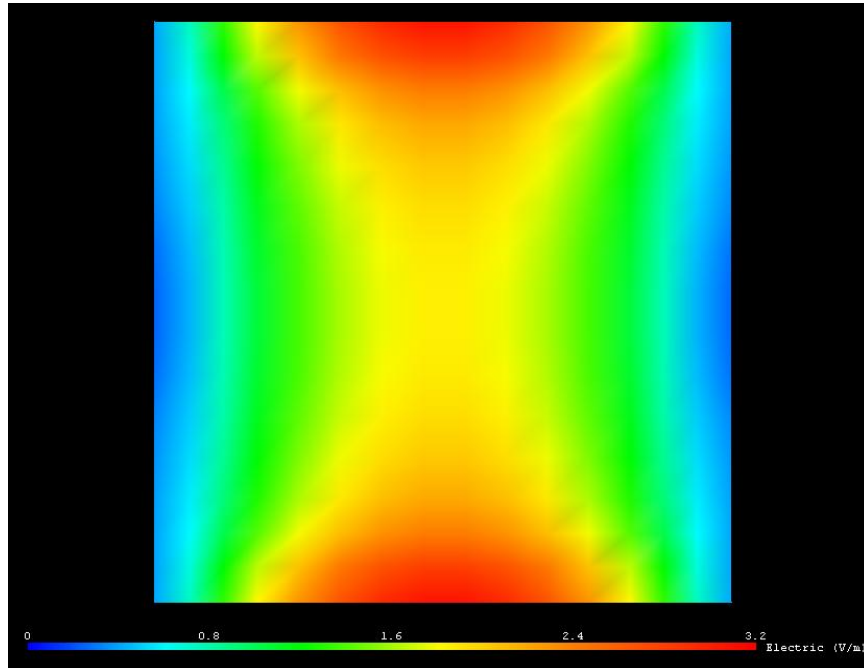
Figure 4.3 Simulation of electric field distribution on graphene coated metal screen: 7.6x7.6 μm^2 opening, arranged in a square lattice with a 12.7 μm pitch. The incident electric field is oscillating along top-to-bottom. The incident wavelength is at resonance with the structure's pitch.

4.2 Anodized Aluminum Oxide (AAO)

4.2.1 Graphenated AAO

Graphene was coating AAO substrates and thinned to a 1-2 layers as shown in Figure 4.4. A commercial code (MicroStripes) was used to calculate the field distribution at the surface of the perforated substrates. As shown in the figure, a perforated oxide is lying on top of aluminum film and is covered by graphene. For calculation purposes, graphene was modeled as an extremely thin metal. The polarized incident plane wave was impinging on the substrate normally. As can be seen from Figure 4.5 (a), the electric field

is concentrated at the holes, just above the hole/air interface. The intensity of the electric field at the surface hole center as a function of incident wavelength is shown in Figure 4.5 (b). The Figure implies that the maximum field intensity is obtained for a wavelength of 370 nm, approximately four times the pitch [Figure 4.6].
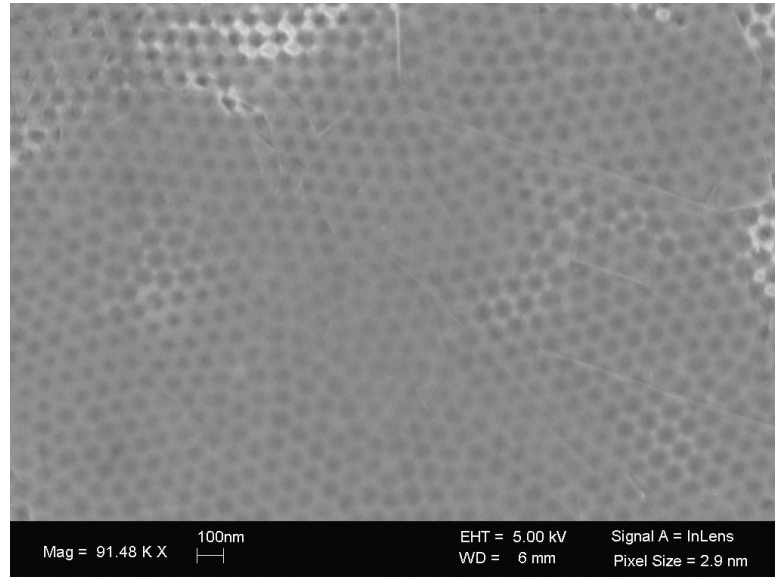
Figure 4.4 SEM picture of graphenated anodized aluminum oxide with a hole size of 20 nm.
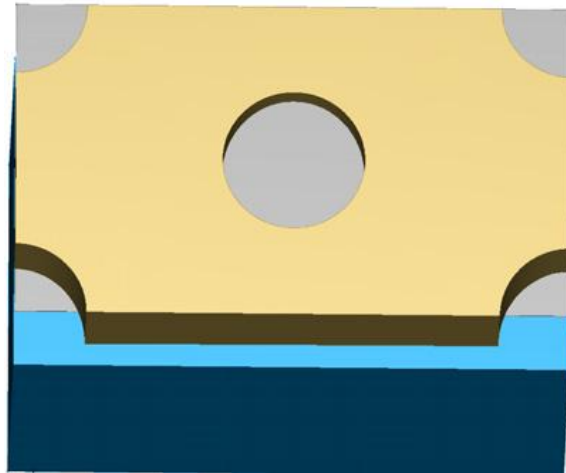
(a)
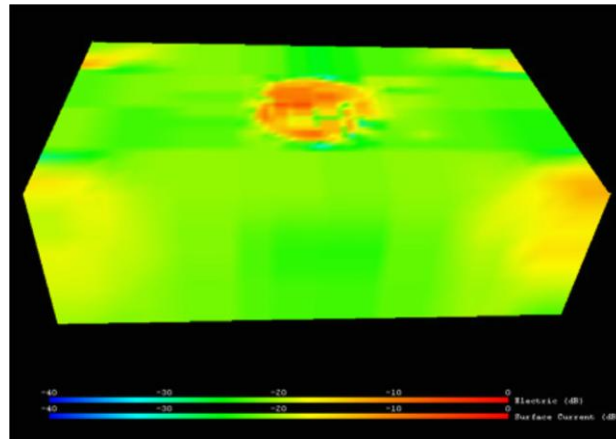
(b)
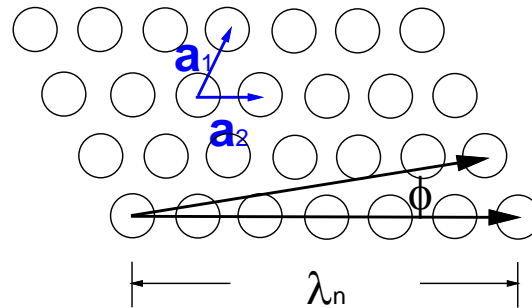
(c)

Figure 4.5 (a) The simulation cell: a 50 nm thick hexagonally perforated oxide (top layer) is lying on top of aluminum (bottom layer). The graphene is deposited on top of the oxide layer. The arrow points to the direction of the TEM polarization state. (b) Electric field intensity map (high intensity at the center is 0 dB. (c) Symmetry of the hole-array. The hexagonal crystallography dictates 60 degrees azimuthal symmetry. Standing wave doubles that value to 30 degrees. Phonons, coupled by the various planes, contribute to in-plane rotation symmetry of 7.5 degrees when considering the 2700 cm^{-1} Raman D' line.
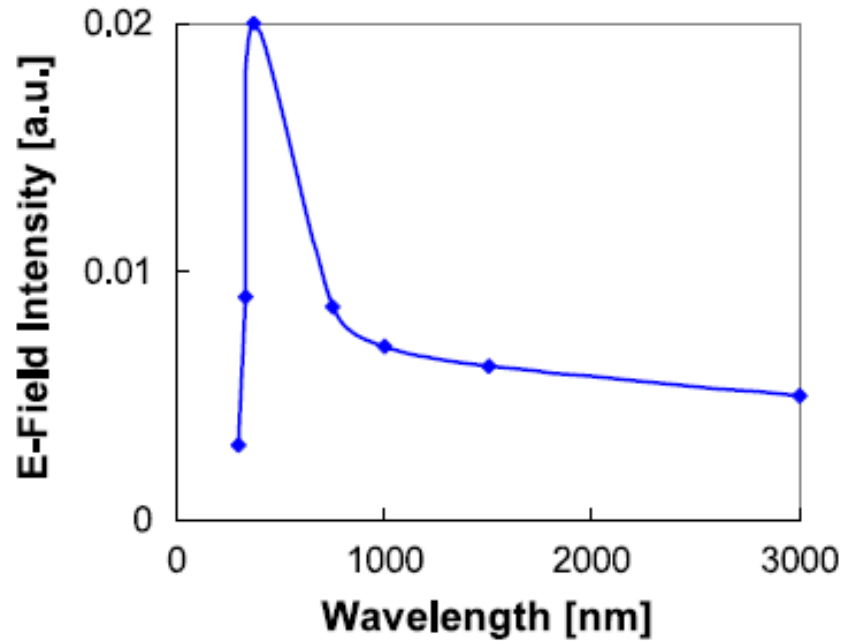
Figure 4.6 Field intensity at the surface-hole center as a function of incident optical wavelength.

4.2.2 Theoretical Consideration – Linear Scattering

This section reiterates the coupling process with more details. Coupling of an incident, free-space electromagnetic beam to surface waves or, surface plasmons polariton (SPP) modes is most conveniently made using corrugated structures and takes the momentum conservation form of,

$$\mathbf{k}_{xy} + q\mathbf{G} = \beta. \tag{4.1}$$

Here $\mathbf{k}_{xy}$ is the projection of the incident beam on the surface, such that, $\left|\mathbf{k}_{xy}\right|=\left|\mathbf{k}_0 sin(\theta)\right|$. The incident beam is launched at an angle θ with respect to the surface normal; β is the wavevector of the SPP mode propagating along the surface; ; $\mathbf{G}$ is the reciprocal lattice vector of holes (openings). The integer q takes both negative and positive values. We note that when G≤k, only the TM mode, with its oscillating electric field within the plane of incidence, may propagate along the surface. Optimal coupling process occurs whenever the pump or the scattered wavelengths are at resonance with the periodic structure [73]. We have extended the resonance condition to sub-wavelength structures. The feedback to the SPP waves may be provided by the periodic hole-array with the caveat that the pitch is much smaller than the incident wavelength. This type of resonance extends over several hole planes and hence, the parameter q is fractional: for example, for a SPP wavelength of 540 nm and hole-array pitch of a=90 nm, resonance at normal incidence dictates $q=\pm1/6$. Coupling to and from these surface modes is provided by the same periodic array of holes.

In an ideal 2-D hexagonal case [Figure 4.5] two lattice vectors are $a_1 = \hat{x}a$ and $a_2 = \hat{x}a/2 + \hat{y}a\sqrt{3}/2$, where a is the distance between the nearest neighbor holes (Figure 4.5(c). The reciprocal lattice vectors are; $G_1 = \hat{x}2\pi/a - \hat{y}2\pi/a\sqrt{3}$ and $G_2 = \hat{y}4\pi/a\sqrt{3}$. Light is coupled to the periodic array of holes by momentum conservation as described by Equation 4.1. Suppose that the surface component of the wave along the AAO sample is scattered from the same periodic structure. This may happen because the AAO is made of densely packed holes with inter hole-spacing, which is much smaller than the propagating wavelength. This is also happening because of the abrupt nature of the hole in the AAO slab, invoking higher-orders and sub-orders of diffraction. One can envision

that such Bragg diffraction creates a standing wave within the hole-array. These considerations are true for the pump as well as, for the scattering wavelengths.

There are two frequencies associated with a given launching angle θ: these are ω^- and ω^+ corresponding to $\boldsymbol{\beta}^-$ and $\boldsymbol{\beta}^+$, respectively. The difference frequency, $\delta\Omega=\omega^+-\omega^-$ defines a frequency gap. At normal incidence, θ=0, the incident beam generates two counter-propagating surface waves, β=±qG. Optimal conditions occur when the scattered mode in the AAO is a standing surface wave. The propagation constant of this surface wave may be written as $\beta=k_0 n_{eff}$ with n_{eff} – the effective index of the surface waveguide. For a loaded SPP waveguides, namely, surface metallic guides topped with a very thin oxide layer, $n_{eff}{\sim}1$, due to the large negative permittivity of the aluminum and the small thickness of oxide layer. Optimal launching conditions may be achieved by a small tilt and in-plane rotation of the sample with respect to the incident beam due to the incomplete gap throughout the Brillouin zone for the hole-array [74]:

$$sin(\theta) = \frac{\lambda_0}{a}\sqrt{(\frac{4}{3})(q_1^2 - q_1 q_2 + q_2^2)} - n_{eff} \tag{4.2}$$

For example, Equation 4.2 predicts θ~5° and θ~0° with q_2=0; q_1=1/6 for the pump wavelength at 514.5 nm and the 558 nm G-Raman line (the 1600 cm^{-1} Stoke line of graphene corresponds to a +43 nm shift from the laser wavelength or, λ=558 nm). It predicts θ~3° for the 587 nm Stoke shift of ~2700 cm^{-1} with q_2=0; q_1=1/7. In fact, one may find numerous resonances in the range between 5-12 degrees because of the densely packed hole-array structure. One of the strongest resonances is for tilt angle θ=8° with q_2=−1/10; q_1=1/10.

CHAPTER 5

RESULTS AND DISCUSSION

In Chapter 5, various applications of graphene are discussed. The applications include graphene based transistors, battery, bio-chemical and optoelectronic devices.

5.1 Characterization of Graphene

As discussed in section 3.2.1, a simple mechanical technique has been developed to lay out mono and few layer graphene on solid and perforated material [75]. With this method graphene was deposited on several substrates: solid, perforated with small holes and largely perforated platforms. Specifically, these substrates were: silicon (Si), anodized aluminium oxide (AAO) and copper screens. Silicon wafers (*p*-type, doping 10^{-16} cm^{-3}) were oxidized to form a thin (20 nm) oxide layer on top of them. In Figure 5.1, deposited graphene layer before and after the thinning stage is demonstrated. Clearly seen is the transparent 2-D crystal on top of the Si [Figure 5.1a, 5.1b and 5.1c]. The coverage was more than 200x50 micron^2 for a given written line. Subsequent and adjacent lines may be obtained as well.
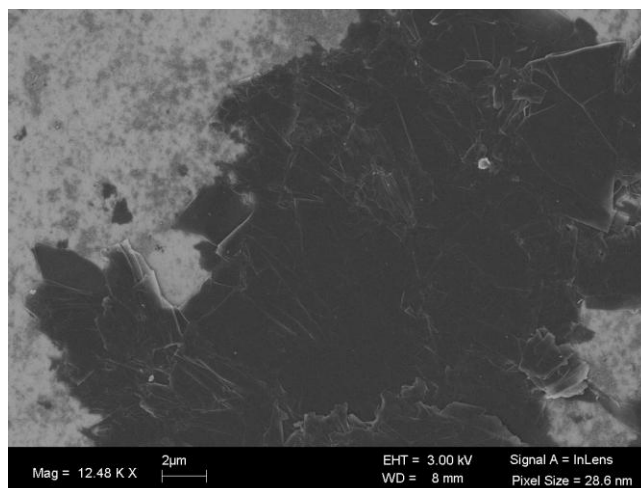
(a)
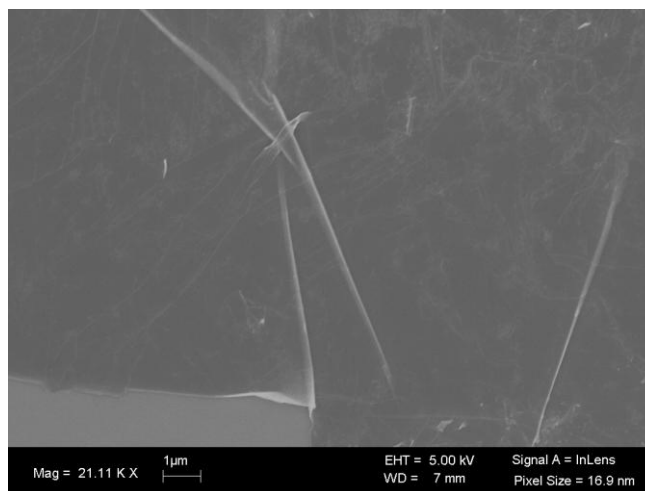
(b)
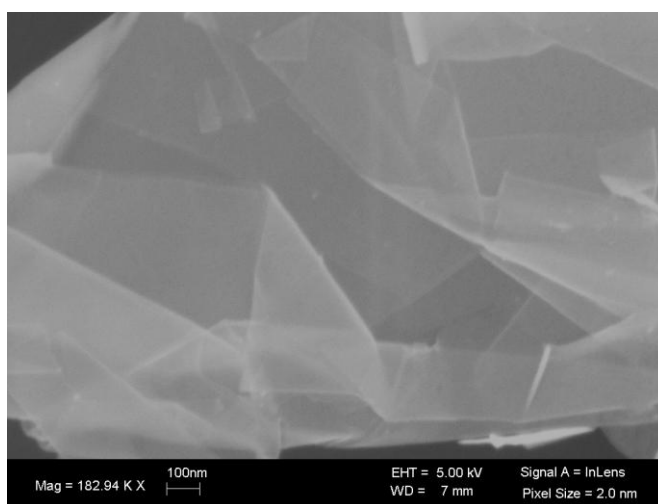
(c)

Figure 5.1 Graphene on Si before (a) and after (b) the thinning stage, (c) a closer look at Figure 5.1b.

Anodized aluminium oxide (AAO) is a perforated, 50 nm thick oxide layer on top of aluminium substrate. The graphene was deposited and processed on AAO similarly to grapheme on Si. The results are shown in Figure 5.2a and 5.2b.
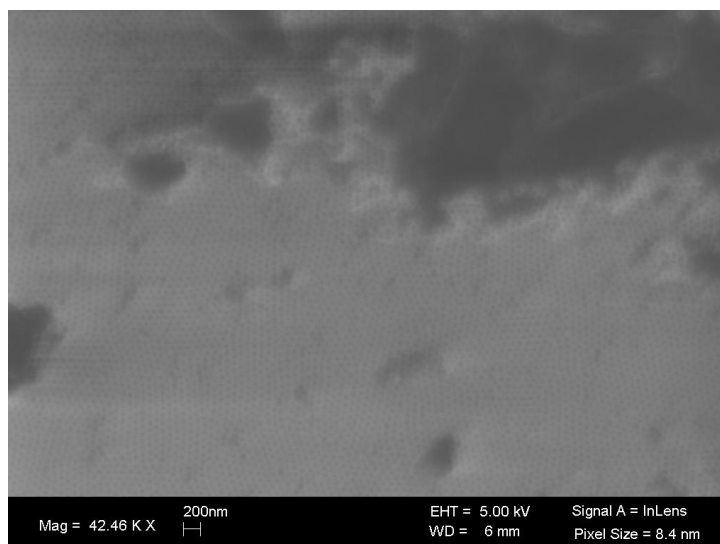
(a)
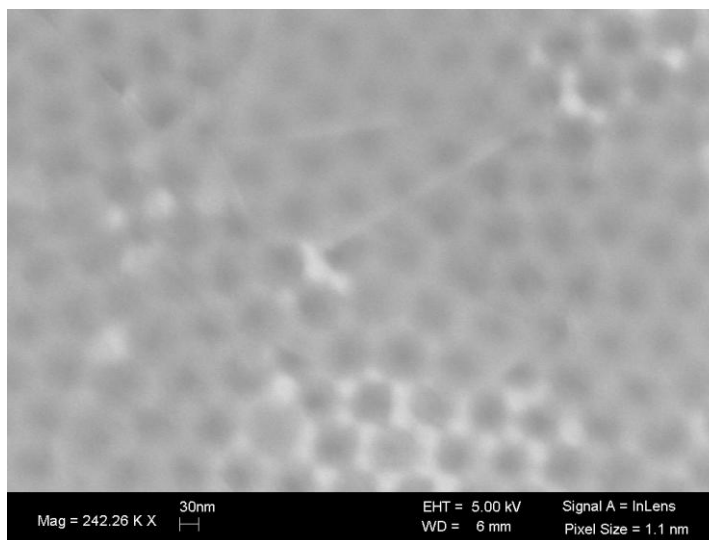
(b)

Figure 5.2 Graphene on AAO: (a) SEM picture of multi layered graphene. (b) a monolayer of graphite (graphene) on AAO after the thinning stage.

Graphene was also deposited on copper screens. These were 5 micron thick screens with periodicity of 15 microns and openings of 8 microns. The graphene-coated screens were sonicated for 2 minutes in ethanol in order to remove excessive layers of graphite. The result was a free standing, three to four layer thick grapheme on the metal-mesh copper screen [Figure 5.3].
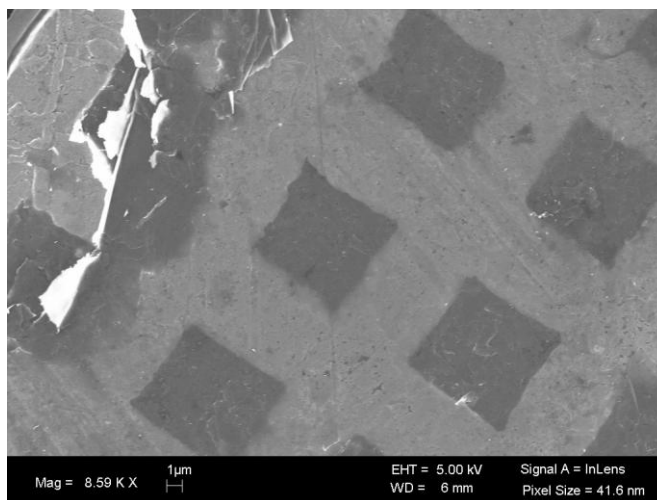
Figure 5.3   Free standing 3-4 layered graphene on copper screen.

Raman spectroscopy is a widely used tool to study graphene. The D` Raman peak of graphene shifts to lower frequencies and somewhat increases as a function of reduced number of layers [Figure 5.4]. The two inmost peak positions for a double layered graphene are 2683 cm^{-1} and 2702 cm^{-1}, respectively [76]. These two peaks are alluded to by curve fitting, yet, hardly resolved experimentally when a two-layer graphene is deposited on silicon [Figure 5.5a]. In contrast, the peaks become clearly visible without any data processing when the graphene is deposited on AAO [Figure 5.5b]. Better resolution may be the result of the unique electric field distribution in AAO: the electric

field intensity in such arrays is concentrated within each hole at the oxide/air interface. It could be assumed that the intensity of Raman spectra depends on the orientation of the hole array with respect to the incidence beam. Indeed, characterizations as a function of tilt angle and laser polarization to be discussed later in this chapter confirm this hypothesis.

For the Raman measurement, an argon (Ar) ion laser at 514.5 nm was used to irradiate the sample. The scattered light was detected in a confocal arrangement with a cooled silicon detector array and using a 0.75 m spectrometer. A bandpass filter was placed before the sample and an edge filter was placed in front of a spectrometer to reject the laser plasma lines and laser line, respectively. Data acquisition was made by averaging five 10 second scans. The intensity of the laser light was 10 mW at the sample using a 40X objective lens.
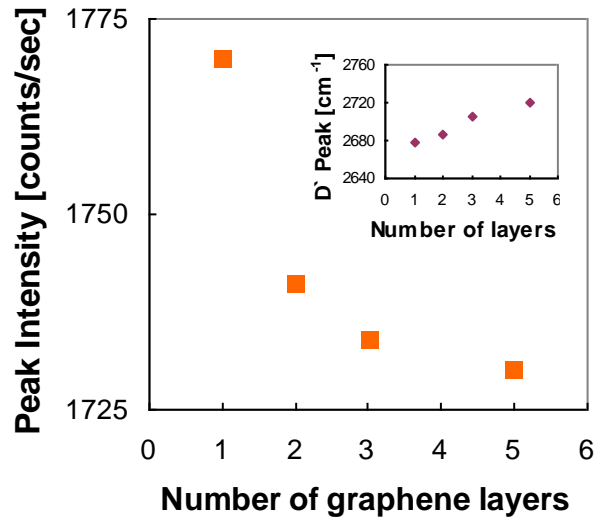
Figure 5.4 Peak of the D' Raman line of graphene on Si as a function of number of layers. The inset shows the shift in the graphene peak as a function of layers.

Suspended graphene on copper screens exhibited Raman spectra as well [Figure 5.5c]. Note that the line is extraordinarily narrow compared to the lines of Figure 5.5a and 5.5b. Three-layer graphene exhibits a few close lines in this spectral region. It has been postulated that one of these lines has been accentuated due to resonating effects by the IR screen.

In general, the Raman peak intensity depends on the screen orientation with respect to the polarization direction of the incident beam. The graphene deposition technique resulted in stress free films as judged by the un-shifted Raman spectra. Infrared transmission through the copper screens exhibited a band pass, typical of metal screens with periodic openings [77].
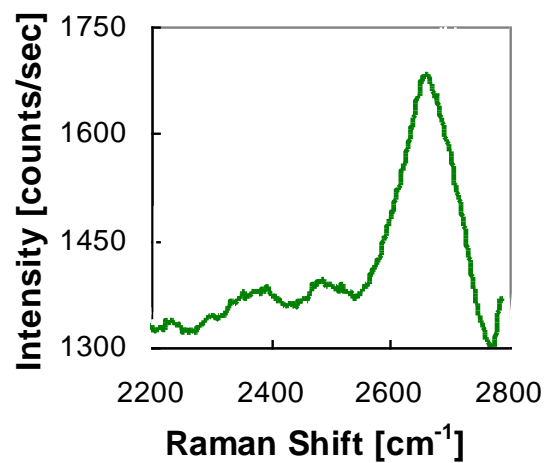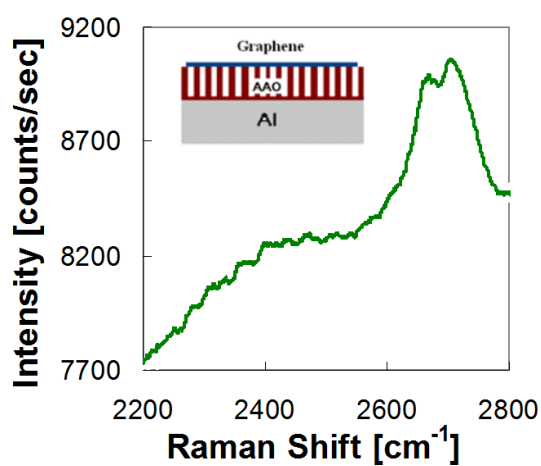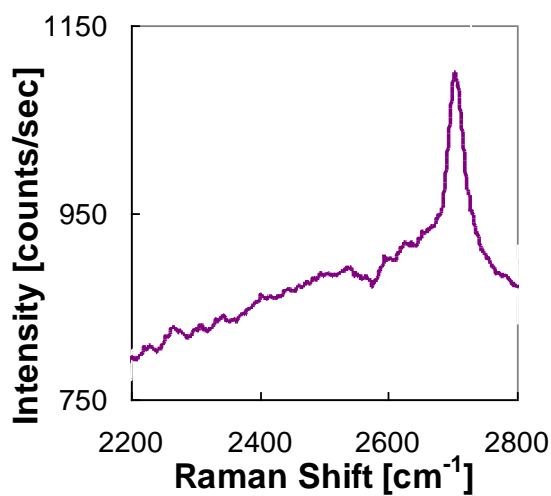
Figure 5.5 Unprocessed Raman spectra of two-layer graphene on (a) silicon substrate and (b) AAO substrate - the peak splitting is clearly visible and (c) 3-4 layers on IR screen. Note the relative narrow Raman line.

The deposition of mere 3-4 layers of graphene on the screen resulted in overall attenuated transmission and a 15 cm^{-1} shift of the resonance frequency [Figure 5.6]. Such relatively large impact is due to the high conductivity of graphene even though; graphite lacks absorption lines in 2.5-25 micron region.
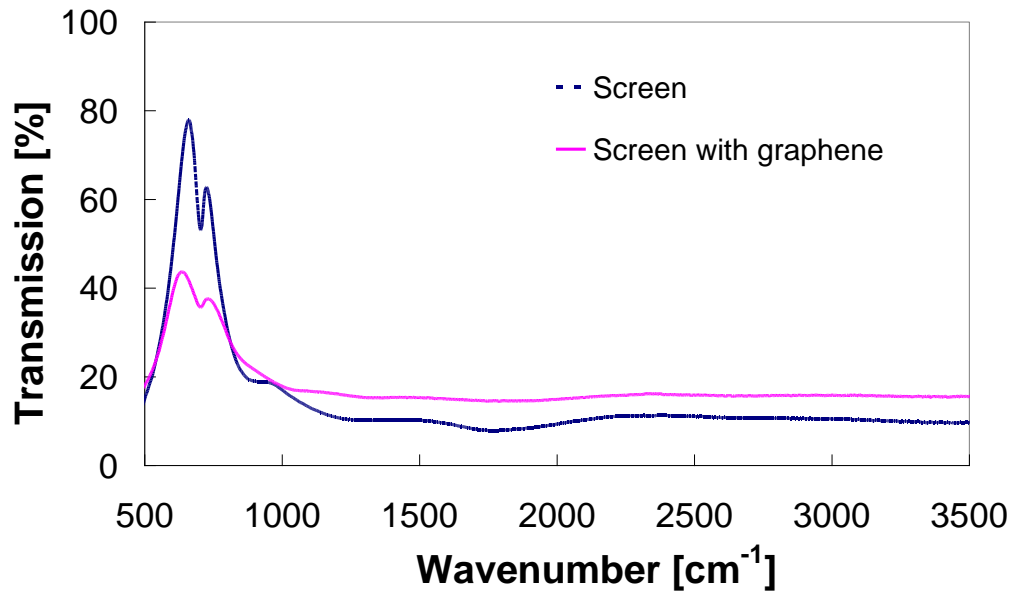
Figure 5.6 Suspended graphene layer on infra red (IR) screens: the square patterned screen had a square opening of 8 micron^2 and a pitch of 15 microns. The IR screen exhibits a transmission band centered at ~690 cm^{-1} or λ~14.5 microns.

5.2 Applications of Graphene

In this section, potential applications of graphene are discussed.

5.2.1   Graphene Based Transistor

Field effect transistors (FET) with graphene on Si/SiO$_2$ substrates were fabricated using 200 nm SiO$_2$ as an insulator layer and the back of the silicon substrate as the gate electrode [78 and 79]. The conductance was measured on FET and its variations as a

function of graphene thickness are shown in Figure 5.7. As expected, as-is deposited graphite film, which contains many layers (and is of thickness of a few microns), is highly conductive. Upon thinning the film by use of sonication, the graphene thickness is reduced to a few layers (no more than four layers). Surprisingly, the conductivity did not substantially change. This implies that the resistance of thick graphite films is the result of interlayer conductivity.
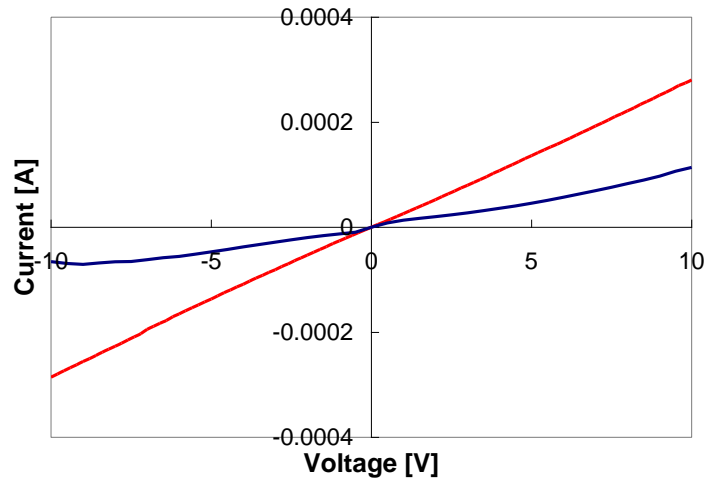
Figure 5.7 Current-voltage of graphene on silicon: as-is graphene layer (red) and after a thinning process by use of sonication (blue curve).

The graphene channel is highly sensitive to contaminations. This is the case shown in Figure 5.8. A drop of di-ionized (DI) water was placed on a graphenated AAO substrate. Two electrodes on the AAO surface were probing the film. Current-voltage (I-V) characteristics of the film exhibited a linear curve. The resistance of the channel increased, by approximately a factor of two, after the wetting process. The DI water was conductive as well due to the presence of ions (the lower linear curve in Figure 5.8): the pH value was relatively small, on the order of 5. While maintaining linear I-V curve, the

resistance fluctuated a bit over time until the sample dried out. At that point, the conductivity of the channel dropped to almost zero (the undulated curve in Figure 5.8) when the sample surface completely dried out. This accentuates the effect the various salts in the water had on the channel conductivity. It was made sure that the effect was not due to oxidation of the probes.
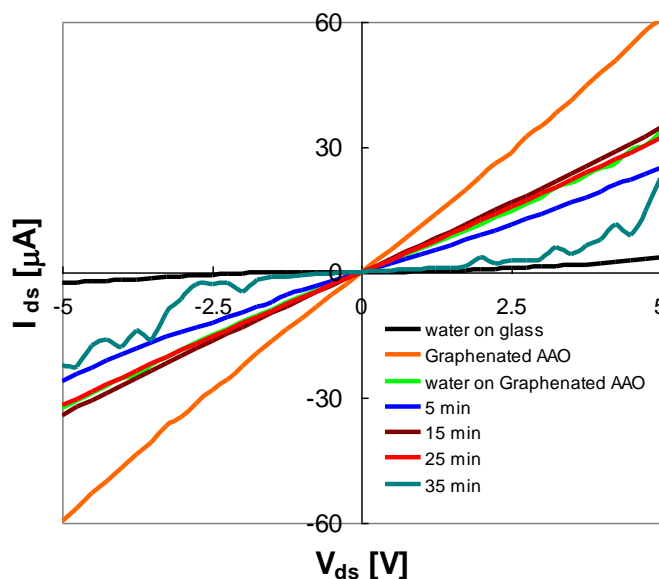
Figure 5.8 The effect of drying DI water on graphenated AAO. The resistance increased by a factor of two as the water dried out. The sample surface dried out completely after 35 minutes and the resistance between −1 V to +1 V became very large.

(a)

(b)

(c)   (d)
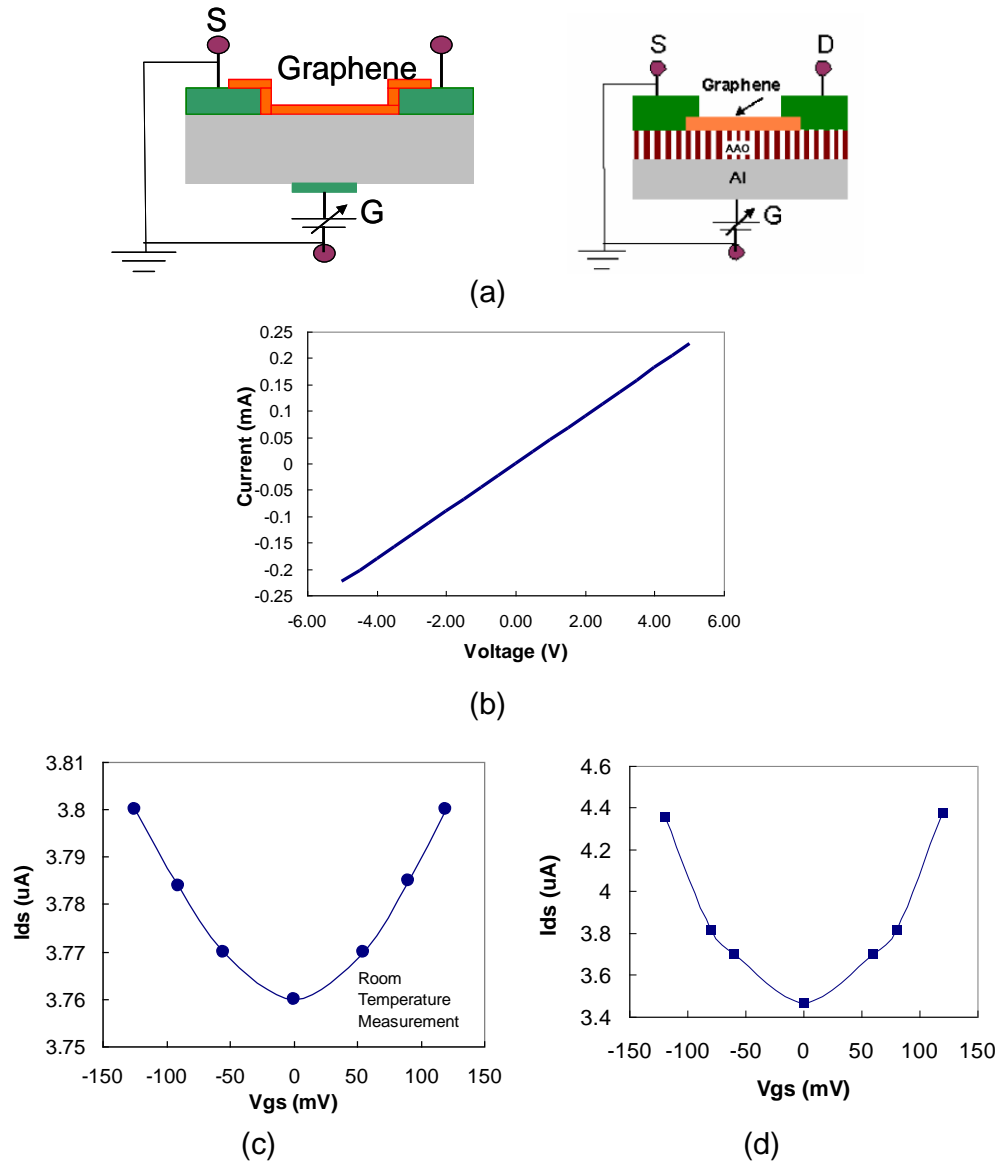
Figure 5.9 (a) Device configuration: left – on silicon; right – on AAO. (b) I_{ds}- V_{ds} characteristics of a graphene bridge on AAO. (c) Source-drain current as a function of gate voltage for a graphene bridge on AAO. (d) A typical Ids-Vgs curve for graphene on silicon substrate. The larger effect for Si is due to the differences in the oxide thickness (50 nm for AAO; 20 nm for SiO_2). V_{ds}=1 V

Electrical characteristics of the structure may be assessed by use of Field Effect Transistor (FET) configuration [78]. Bridges of graphene were made between two electrodes and were placed on the surface of either Si/SiO_2 or AAO substrates. Figure 5.9(a) shows the device configuration. The various current voltage characteristics are

shown in Figure 5.9(b) and 5.9(c) for graphene on AAO and in Figure 5.9(d) for graphene on silicon. Either the back aluminum film or the silicon was used as the gate electrode. Graphene exhibits a linear I_{ds}-V_{ds} curve because it is a semi-metal. The current-gate voltage or I_{ds}-V_{gs} characteristics are symmetric about the zero-bias gate potential with a transition point signifying a singular point of the density of states (the so called Dirac point).

Further measurements were made to assess the capacitance of graphene on silicon. The change in the capacitance as a function of gate voltage is shown in Figure 5.10. The gated configuration was made with graphene as a channel on oxidized Si substrates and using the silicon substrate as back gate electrode. The capacitance values were corrected for the capacitance of the cables. The mobility μ may be assessed by the conductivity σ at a given drain-to-source current I_{ds} and gate voltage V_{gs}. Here, calculated conductivity is the ratio of the derivatives of I_{ds} and V_{gs}. The mobility is written as, $\mu = \sigma/en$. Here e is the electric charge (1.6022×10^{-19} C) and n is the carrier density in the graphene layer ($\sim 10^{12}/cm^2$). The calculated mobility, $\mu = 5000$ cm^2/Vs, is in accord with known values for high-quality graphene [39]. The conductance of the same sample was measured as a function of various frequencies [Figure 5.11].
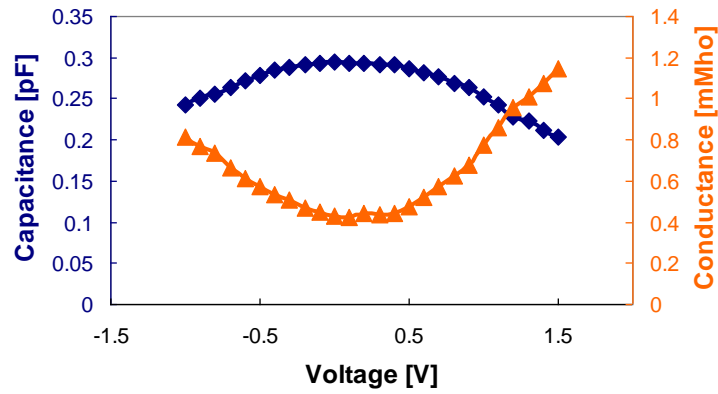
Figure 5.10 Conductance and capacitance of gated graphenated Si/SiO$_2$ sample as a function of gate voltage.
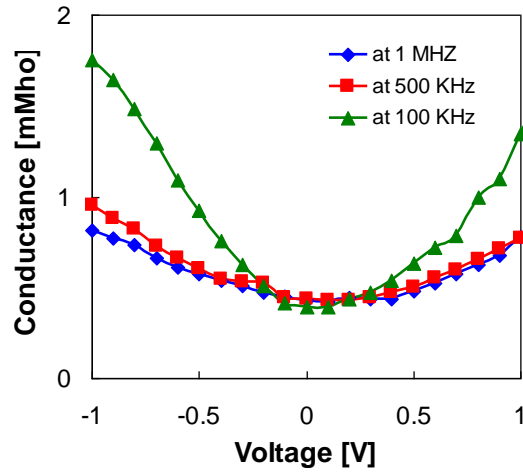
Figure 5.11 Conductance of graphene-coated channel on Si/SiO$_2$ as a function of gate voltage at various frequencies.
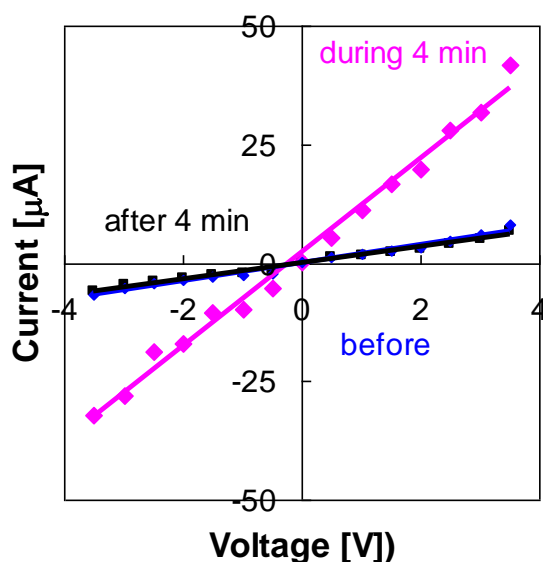
Figure 5.12 Effect of irradiating graphenated AAO sample with UV light (4 mW/cm^2). The conductivity in the dark before UV exposure was recovered after 4 minutes in the dark. The conductivity after 4 minutes of UV exposure was 6 times larger than the conductivity in the dark.

The effect of UV light on graphenated AAO is shown in Figure 5.12. The effect is rather slow. The sample recovered to its original resistance after 4 minutes in the dark. The slow effect is probably due to the high transparency of the film resulting in a limited interaction between light and film.

5.2.2 Graphene Based Battery

Electrochemical reactions have been studied since the early eighteenth century [80, 81]. In wet batteries, there are two half-cell reactions. In one, oxidation of the anode takes place and the positive metal ions are dissolved into an electrolyte. The remaining electrons flow through an external load to the second half-cell, where reduction takes place. The cathode is immersed in an electrolyte and its ions react with the excess electrons, donated by the anode. The circuit is completed by drift and diffusion of ions in

the electrolyte. The two-half cells are typically connected via a salt-bridge, which enables the passage of ions, yet, limits the flow of the bulk electrolyte (water). Instead of a salt bridge one may use a paper or a Teflon filter coated with graphene – monolayer or, a few layer thick graphite.
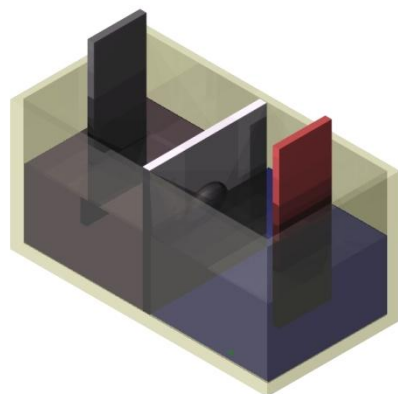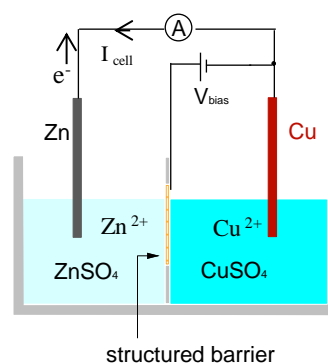
(a) (b)
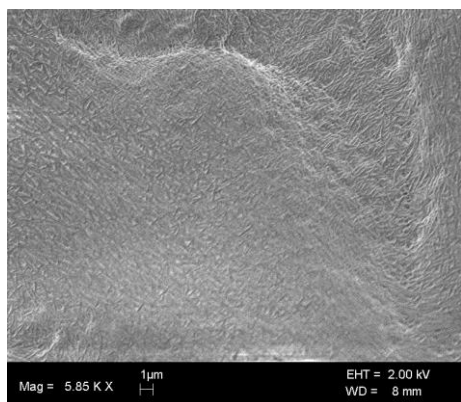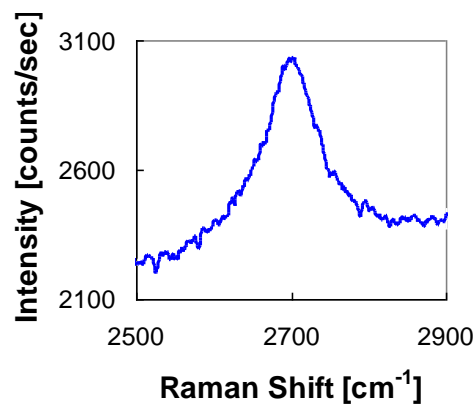
(c) (d)

Figure 5.13 (a) Block diagram for the measurement and (b) control setup. The two half-cells are brought to contact separated by a graphenated filter. Bias is provided either, between the graphene and Cu electrodes (as shown), or, between the graphene and Zn electrode. (c) Scanning electron microscope (SEM) picture of graphenated Teflon filter. (d) Raman spectra indicating 2-3 layered graphene.

The battery is schematically shown in Figure 5.13a and 5.13b. In one cell, Zn electrode (either solid or, preferably wool type) was immersed in $ZnSO_4$. In the other, a solid Cu electrode was immersed in $CuSO_4$. Graphene-coated 10 micron Teflon filter separated the two half-cells. Graphene was deposited on the filters according to the previous recipe [75]. Scanning electron microscopy (SEM) shows the graphene coated Teflon filter [Figure 5.13c]. The Raman D' line ($\sim$2700 cm^{-1}) indicates a 2-layer graphene [Figure 5.13d].

The outer circuit is defined between the Zn-Cu electrodes. External bias (or, simply, the bias) was applied either between the graphene and Cu (G-Cu) or between the graphene and Zn (G-Zn) pair of electrodes. The Zn and Cu electrodes were 5 cm apart with the graphene screen placed in the middle. In some instances, the biasing source was separated from the external circuit by a capacitor of 4.7 μF. The circuit was examined with and without the capacitor in place. The current I_{cell} in the outer circuit between the Zn-Cu electrodes and the open circuit voltage E_{cell} between them were monitored as a function of the bias voltage V_{bias}. The biasing unit was turned on even for V_{bias}=0; a typical voltage source has a residual voltage (<0.1 V) even when its dial shows 0. Each data point for these DC I-V curves was taken after a steady states condition was reached. This was a matter of a few seconds when the bias voltage was larger than $|1|$ V. It was a matter of a few minutes as the bias voltage approached the stopping potential value. Notably, the resistance of the cell with 0.1 M electrolyte was on the order of 1 Kohm; the capacitance of the graphene membrane is estimated at 10^{-5} F assuming 1 cm^2 graphene film and a double layer thickness of 1 nm; the time constant for the circuit is therefore, estimated at less than a second.

Following Nernst, the developed voltage between unbiased Cu-Zn electrodes ought to be $E_{cell}=1.1 - 0.03 log[Zn^{2+}/Cu^{2+}]\sim1.1$ Volts since the ion concentration of both the $ZnSO_4$ and the $CuSO_4$ are approximately equals to 0.1 M. The measured open circuit voltage was $E_{cell}=1.09$ V; the current was $I_{cell}=2$ mA. In Figure 5.14a, I_{cell} has been shown as a function of the bias potential V_{bias}, either $V_{bias}=V_{G-Cu}$, or, $V_{bias}=V_{G-Zn}$ (blue curve; left scale). The current curve is symmetric and the cell potential E_{cell} flips sign from -1.1 V to $+1.1$ V (red dot curve; right scale) with respect to the biasing voltage. Figure 5.14(b) exhibits a symmetric current curve with respect to the biasing voltage; however, E_{cell} is a monotonic curve. No change was noted in the color of the electrolyte or the graphene layer.
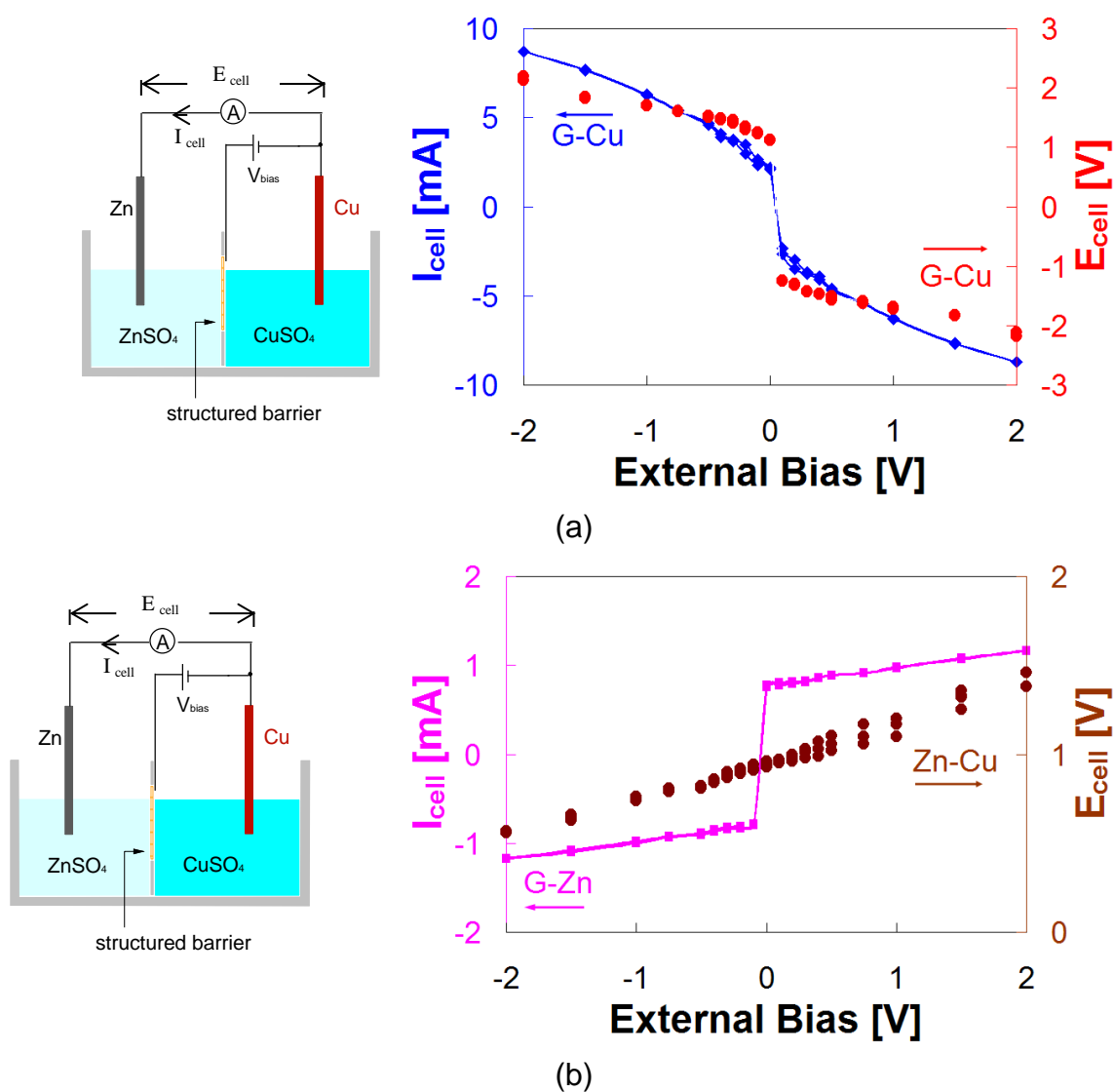
Figure 5.14 I_{cell}-V_{bias}, for (a) G-Cu and (b) G-Zn when the capacitor is omitted (scale on the left). Also shown is the open circuit potential E_{cell} as a function of the bias potential V_{bias} (scale on the right). The current curves become symmetric with respect to changing the biasing scheme.

In Figure 5.15(a) I_{cell} has been shown as a function of the bias potential $V_{bias}=V_{G-Cu}$. Here adding a capacitor of 5.14 μF helps the current to block from the biasing source to the Cu or Zn electrodes. No current was flowing through this capacitor, yet, $I_{cell}(V_{bias}=0)$ substantially dropped. The I_{cell}-V_{G-Cu} curve is linear: the point of current

stoppage, I_{cell}=0 A is assessed at a V_{bias}=+0.015 V (blue curve; left scale). At this point, the open circuit voltage approaches zero, as well: $E_{cell} \to 0$ V (red dots; right scale). When providing bias to the graphene-zinc (G-Zn) electrode pair the situation is somewhat different [Figure 5.15b]: the linear I_{cell}-V_{G-Zn} curve becomes zero at much more negative values, at approximately −3 V (violet curve; left scale); $E_{cell} \to 0$ V as well (brown dots; right scale).

Results were similar when the electrolyte concentration of both substrates was increased to 1 M in each half cell. As expected, the cell resistance decreased and I_{cell} at V_{G-Cu}=0 has increased by 50%. The stopping voltage for the 1 M case was +0.022 V. No hysteresis was noted during all experiments; there was no discoloring of the electrolyte; the graphenated filter could be reused over many I-V cycles and survived replenishment of electrolytes and drying out periods as well.

(a)

(b)
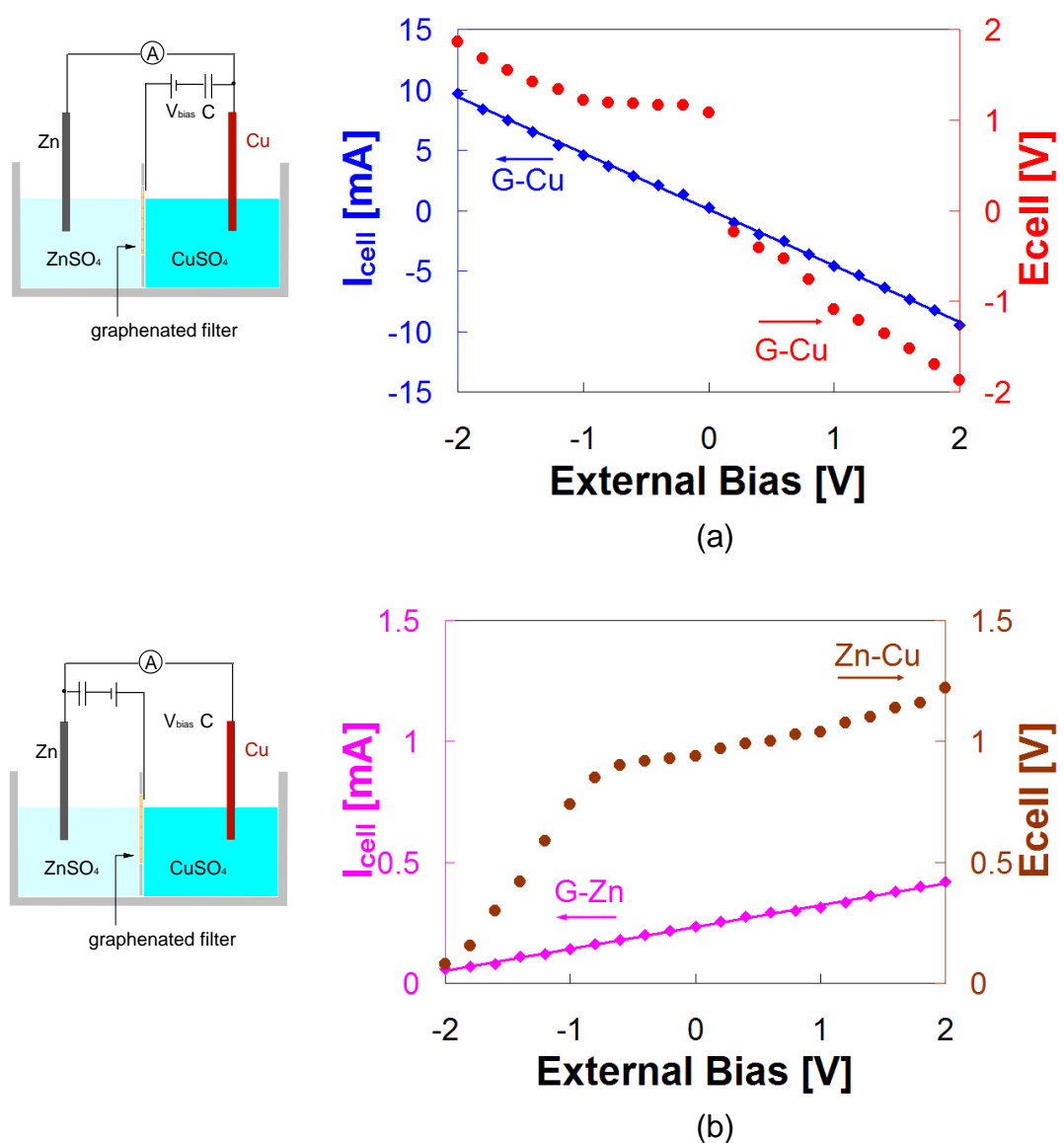
Figure 5.15 I_{cell}-V_{bias}, for (a) G-Cu and (b) G-Zn when the capacitor is in place (scale on the left). The bias source is separated from either electrode by a capacitor of 4.7 μF. Also shown is the open circuit potential E_{cell} as a function of the bias potential V_{bias} (scale on the right). The current curves become asymmetric with respect to changing the biasing scheme.

Control of ions by a screening electrode is far more complex than the screening

of electrons in vacuum tubes. In the latter, control of only one charge species is needed –

the negatively charged electrons. The mean free path for electrons in vacuum is larger

than the distance between the cathode and the anode. In contrast, both positive (cations) and negative (anions) charges are present in the electrochemical cell. Their charge is screened within a characteristic distance on the order of a few nanometers (the Debye length).

The bias potentials (between G-Cu and G-Zn electrodes) are then accessed, which are smaller than $|1|$ V. At these values, oxidation of the electrolyte (SO_4^{2-} to $S_2O_8^{2-}$ at $E_{ox}=-2.01$ V) and the oxidation of water at -1.23 V may be neglected. Thus, reactions, which involve either SO_4^{2-} with H^+, or with OH^- may be neglected, as well. One may also argue that $E_{cell}\sim1.1$ V at zero bias is an indication for the simple reaction $Zn_{(s)}+Cu^{2+}_{(aq)}\rightarrow Cu_{(s)}+Zn^{2+}$.

Direct current in the cell is driven by the two electrode reactions. At equilibrium, this current may be written as, $I_{cell}(0)=E_{cell}(0)/(R_{cell}+R_L)$. Neglecting the contact resistance and in the absence of an outer circuit load resistor R_L, the circuit's resistance is mainly dictated by the cell resistance, on the order of 1 KΩ from Cu to Zn. When separated from one of the electrodes by a capacitor, the effect of the biasing source is mostly to offset the electrode surface potential in its loop. The direct current at steady states conditions may now be written as, $I_{cell}(V_{bias})=I_{cell}(0)-(V_{bias}+V_C)/R_{half-cell}$. Here V_C is the voltage developed across the capacitor. The overall current through the graphene screen is therefore, substantially reduced but provides with a method to control I_{cell} with another battery (the biasing source). This is the linear curve of Figure 5.16a. The difference between the stopping potentials for the Cu and the Zn sides may be explained by the difference in the standard potentials for Zn and Cu and the behavior of the interfaces between graphene and either electrolyte under positive and negative bias.

These two cases need not be symmetric since an unbiased cell already breaks the symmetry by dictating a flow of electrons from the zinc to the copper electrode through the outer circuit. In these experiments it is found that the capacitor was fairly leaky; this means that the capacitor may be replaced by a large resistor.
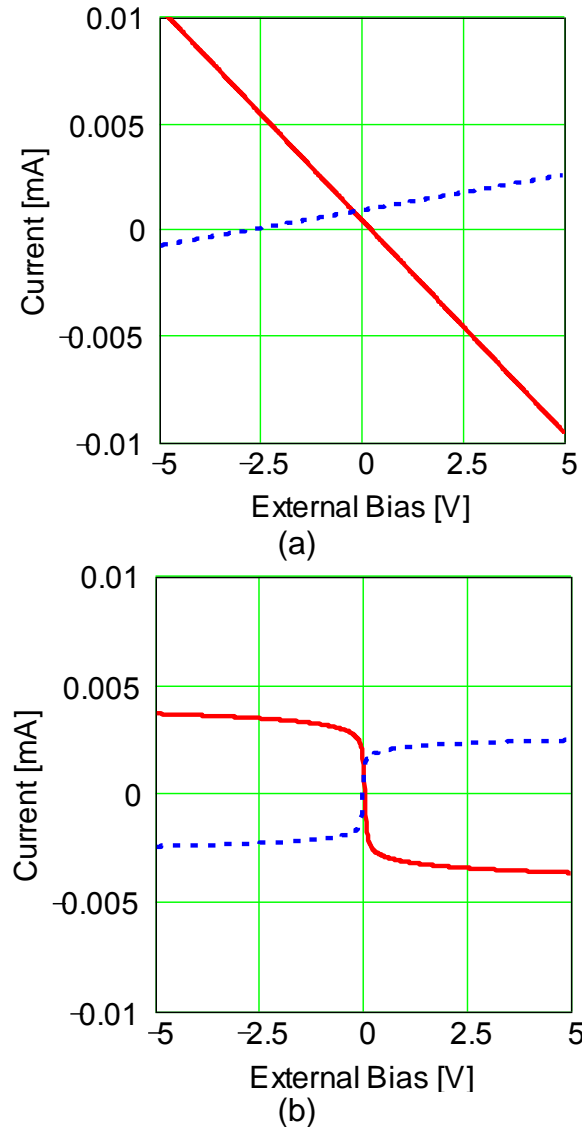
Figure 5.16 Model: (a) With a capacitor next to the biasing source: red solid curve – G-Cu; blue dash curve – G-Zn. R_{eff}=500 Ω and 3000 Ω for the solid and dash curves, respectively. (b) without a capacitor next to the biasing source: red solid curve – G-Cu; blue dash curve – G-Zn. R_{eff}=200 Ω and 300 Ω for the solid and dash curves, respectively. Other parameters are: a=1, I_0=10^{-6} A, V_C=0.3 V and R_L=25 Ω.

When the capacitor is removed another current source was added: which is the electronic current supplied by the biasing source. The effective resistors values were also modified. The additional oxidation-reduction current depends on the overpotential V−η as,

$$I_{ox\text{-}rd}(V)=I_0[\exp(a_a F(V-\eta)/RT)-\exp(-a_c F(V-\eta)/RT))]. . \qquad [5.1]$$

Here, RT/F=0.06 V at room temperature and a_a and a_c are the reaction coefficients. The overpotential V−η includes the effect of phase boundary potentials, as well as the potential drop across the electrolyte. At the same time, the ion current regulates the surface potential itself. To simplify, it is narrated that the overpotential to an effective potential, which depends on $I_{cell,}$ such that, V−η=$aI_{cell}R_{eff}$ with $a=a_a=a_c$ and R_{eff} − the effective cell resistance, including the resistance of the biasing source. The overall direct current at steady states condition is, $I_{cell}(V_{bias})=I_{cell}(0)-(V_{bias}-\eta)/R_L-I_{ox\text{-}rd}(V_{bias})$. Here, the load resistor is the resistance of the outer circuit (which is very small in our case). This is the nonlinear curve of Figure 5.16b. The model works equally well for G-Cu and G-Zn. The difference between the cases is the effective resistor value R_{eff}. Yet, as demonstrated by Figure 5.14 and 5.15, the screening is most effective of the cathode side due to the symmetry breaking current flow in batteries: in unbiased cell electrons will flow from the zinc to the copper electrode.

The time constant for steady states conditions has been established at less than a second based on the cell's resistivity, reasonable capacitance values for the screening electrode (graphene) and the other capacitor (4.7 μF). In most cases, a few seconds were

enough for the system to equilibrate except for very near to the stopping potential values. There, the oxidation-reduction reaction is stopped with no preferential current direction to the cell. Charge perturbations at a very highly screened system (Debye length on the order of 1 nm) are the major factor for the long time-constants.

In summary, oxidation-reduction reaction was stopped by placing a screening electrode in the ionic path. Such and similar constructions may be appropriate for transistor-like ionic tunneling experiments and useful for the fabrication of electronically controlled graphene interfaced bio-membranes.

5.2.3   Surface Plasmon Laser with Quantum Dots as Gain Media

Though dating back to the beginning of the twentieth century, the subject of surface plasmons [82, 83] has regained interest recently. Surface plasmons (SP) are near-field phenomena: these electromagnetic waves are confined to a surface between a conductor and dielectric. It is hoped that high-speed opto-electronics will benefit from the use of such metallic nano-structures [84]. As for ordinary lasers, surface plasmon lasers require gain and feedback. In the past, it has been demonstrated that SP laser attributes at 560 nm using dye (fluorescein) as a gain medium [74]. While dyes provide strong photo luminescence, they oxidize easily and tend to bleach. On the other hand, quantum dots (QDs) and specifically, core/shell dots, are robust photo-luminescence (PL) sources. The effect of amplified spontaneous emission (ASE) was discussed while demonstrating QD-based SP laser at 630 nm.

The structures were made of surface waveguides: a perforated 50 nm thick oxide layer (aluminum oxide) separated a metal (aluminum) from air [Figure 5.17]. The

perforated thin oxide layer was bound from the top by graphene. Gain was provided by core/shell, CdSe/ZnS, QDs. The dots were deposited on the graphene layer (Figure 5.17). As seen below, the graphene maintains the QDs just above the platform surface. Some of the dots were situated above the pores where strong electric field lines are concentrated [85]. The feedback to the SP waves was provided by the same sub-wavelength, periodic hole-array. Distinction from typical photonic-crystal based semiconductor lasers [86, 87] are the pitch of the hole-array - 1/6 of SP wavelength, extremely thin oxide layer and the presence of a metallic substrate.
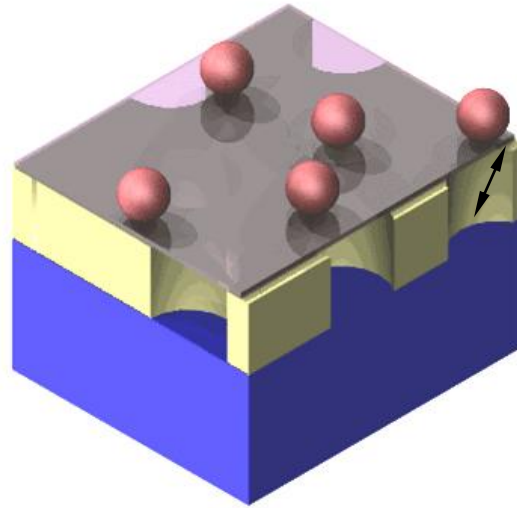
(a)
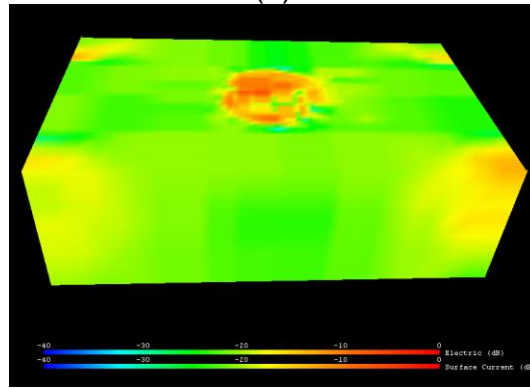
(b)
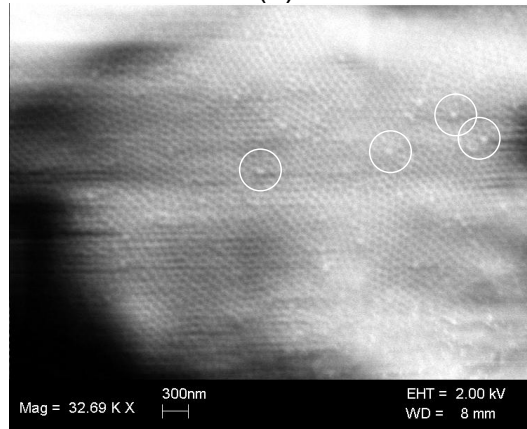
(c)

Figure 5.17 Quantum dots (red spheres) on top of a hole-array in alumina (pale yellow); the array is sandwiched between aluminum (blue) and a semi-transparent 2-layered graphene (gray). The hole-array pitch was a=90 nm. (b) The polarized electric field (black arrow) in a TEM mode is concentrated at the hole-air interface, removed from the aluminum substrate. (c) Quantum dots (marked by white circles) on graphaneted anodized aluminum oxide (AAO).

Conditions for optimal launching and retrieval of light for these perforated substrates are obtained when the samples are tilted at an angle θ and rotated at an angle φ with respect to the beam [85]. The optimal angle φ provides match between the linear input polarization and one of the symmetry axes of the perforated surface. The angle θ may be calculated as [74],

$$sin(\theta) = \frac{\lambda_0}{a}\sqrt{(\frac{4}{3})(q_1^2 - q_1q_2 + q_2^2)} - n_{eff} \ . \tag{5.2}$$

Here λ_0 is the wavelength of interest in vacuum, a is the lattice constant (or, the pitch of this hexagonal hole-array), q_1 and q_2 are the modified Miller indices (note that these are fraction of integers when dealing with sub-wavelength crystals). The surface waveguide mode is defined by the propagation constant $\beta = k_0 n_{eff}$, with n_{eff} – the effective index of the guide. For loaded and periodically patterned SP waveguides, namely, surface metallic guides topped by a very thin oxide layer with nano-hole array, $n_{eff} \sim \sqrt{(\varepsilon_1\varepsilon_2/\varepsilon_1 + \varepsilon_2)} \sim 1$ due to the large negative permittivity of the aluminum substrate and the small thickness of oxide layer. Here, ε_1, ε_2 being the dielectric constants of air and metal, respectively. For such two-dimensional loaded surface guide, both TM and TE modes of scatterings are possible, with the larger scattering obtained for TM modes. Simulations indicated that the strongest effect for TEM incident mode is obtained when the wavelength-to-pitch ratio is 4.

Substrates were made of anodized aluminum oxide (AAO) [88-90]. Two-layer graphene was deposited as outlined in Reference 68 and sonicated in water. The core/shell, CdSe/ZnS, QDs, purchased from NanoTech Ocean, were dissolved in toluene,

dropped on the substrate and let dry out. In the experiments, we used a confocal arrangement, whereby the sample was tilted and azimuthally rotated (in-plane rotations) with respect to the linearly polarized TM or TE incident beams until optimal conditions were obtained. The spot-size of the pump laser was small (~5 μm); it was found that a slight of defocusing is advantageous to these experiment. This was obtained with a beam diameter of ~0.5 cm and a focusing lens of f=5 cm (or, NA~0.1).

Photoluminescenc (PL) signal as a function of wavelength is shown in Figure 5.18 for glass-slide coated samples. The samples were pumped with a pulsed laser (doubled frequency, 10 Hz Nd:YAG laser, 10 ns pulses at 532 nm). Detection of the PL signals was made with a photomultiplier-interfaced spectrometer and a lock-in amplifier. Two sharp spectral filters cut the pump laser line off. When deposited on a glass slide, one measures several peaks. The peak is asymmetric and inclines towards the longer wavelengths [91]. The peak at λ=630 microns (1.96 eV) dominates the other lower energy peaks. As shown in Figure 5.18, the PL as a function of intensity exhibits a phase-transition like behavior. The spectral line width for the 630 nm peak remained unchanged at 12 nm when pumped with 2 (bottom of the transition curve), or 4 mW (top of the transition curve). Such phase transition signifies the effect of gain overcoming loss and in particular, Auger type loss [92]. The small dimensions of such spot limits the maximum gain to $G^{max}(\equiv \exp(\gamma l_g) \sim 4\pi(l_g)^2/A$. Here γ is the gain coefficient, l_g is twice the film thickness, or ~2x1 micron, due to the confocal arrangement; A is the area of the illuminated spot (~5^2 micron^2). This translates to G^{max}~2. As a result, one expects little or, no spectral line narrowing for glass coated films. In the absence of feedback, the experimental data point to the characteristics of amplified spontaneous emission (ASE).
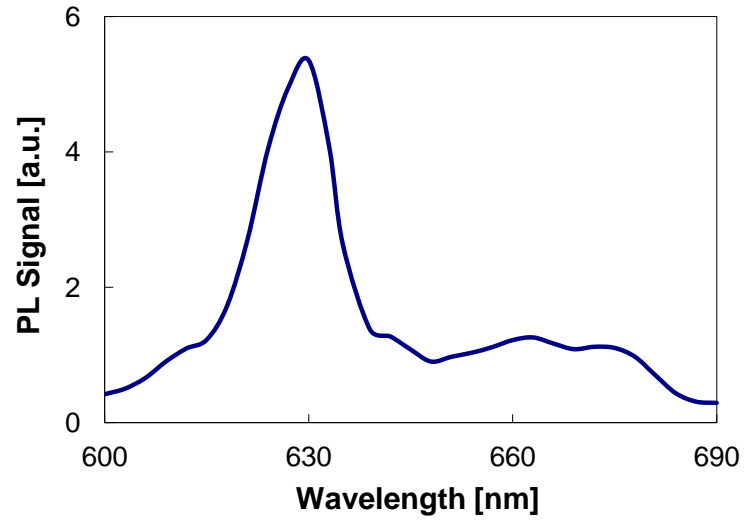
(a)
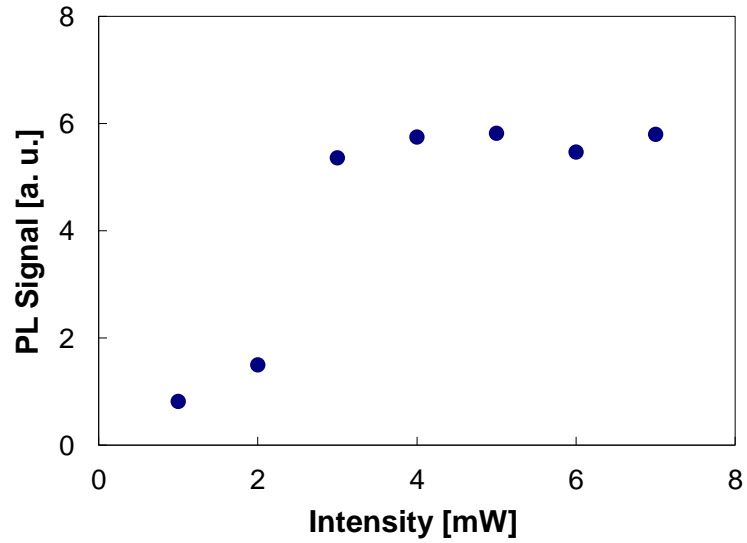
(b)

Figure 5.18 (a) PL spectra as a function of wavelength for a glass coated film. (b) The 630 nm peak as a function of pump intensity. The sample was placed normal to the pump beam.

The effect of feedback could be observed by placing a thin film of QDs on a silicon substrate (not shown). When the film is thin enough, gain guided effects are confining the pump and scattered beams laterally and Fabry-Perot modes are confining

the beam longitudinally. Both effects enhance the PL output. The transition curve as a function of pump intensity is sharp, similarly to the glass coated case, yet, is associated with spectral line narrowing. The PL line width may be as narrow as 4.5 nm. The angular emission is limited to $\pm 5^o$ from normal, pointing to the directional nature of the feedback.

The effect of feedback could be enhanced and the PL line width further narrowed when the QDs were placed on graphenated AAO substrates [Figure 5.19]. The spectral line width measured has reduced to less than 3 nm, or, a factor of 4 smaller than the line width for glass coated films. In Figure 5.19, a saturated gain fit has been added to the data: $PL \sim g_{ss}(I-I_{th})/[1+(I-I_{th})/I_s]$. Here, g_{ss} is the normalized small gain coefficient, I is the pump laser intensity, $I_{th}=5$ mW is the threshold value and $I_s=2.5$ mW is the saturation intensity. A high gain of $\gamma_{ss}=2 \times 10^5$ cm^{-1}, may be obtained from $\gamma_{ss} \sim g_{ss}/D$ with the assumption that it is distributed across the small spot size $D \sim 5$ μm.

Finally, when placing a polarizer in front of the spectrometer [93] one may assess the TM vs TE scattered modes at $\lambda=630$ nm. Both modes existed in the spectra when the samples were pumped with the incident TE pump mode; yet, the TM scattered mode was ten times stronger [Figure 5.20]. When pumped with an incident TM pump mode, the scattered light included only the TM mode. Such data corroborate the efficient coupling between pump and scattered plasmonic modes, which are mostly TM [74].

Laser attributes for SP laser with CdSe/ZnS QDs as gain medium have been demonstrated. Threshold and spectral line width narrowing, by more than a factor of 4, signified the laser operation. Besides opto-electronic applications, such as intra-chip communication, one may envision new bio-chemical applications since QDs are good bio-species fluorescence marker.
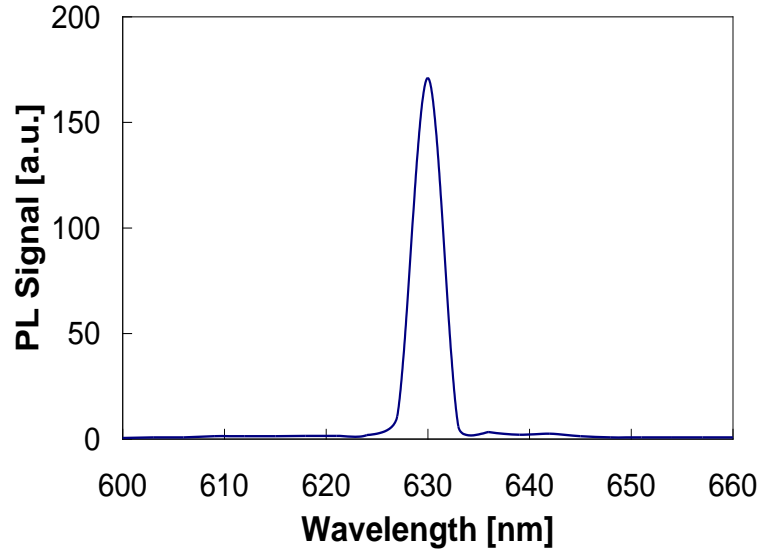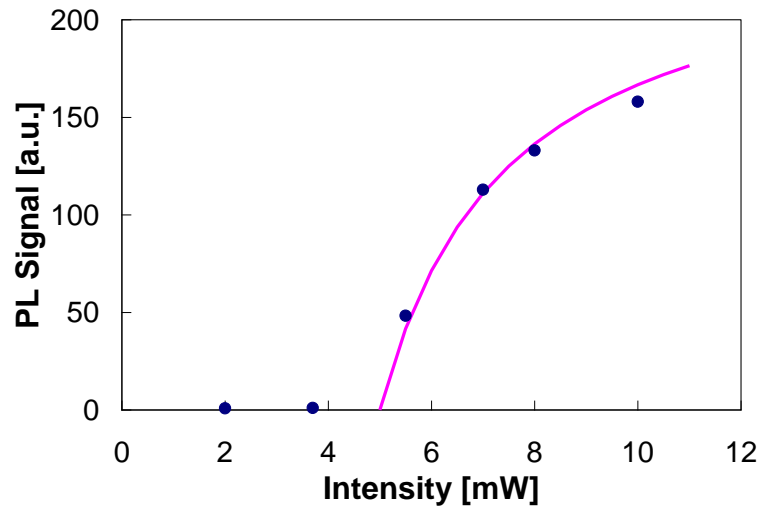
Figure 5.19 QD on graphenated AAO substrates. (a) PL as a function of wavelength at pump intensity of 10 mW. (b) The 630 nm PL peak as a function of pump intensity at the optimal tilt angle of $\theta=16^{\circ}$. The saturated gain fit is indicated by the solid line: $g_{ss}=100$; $I_{th}=5$ mW; $I_s=2.5$ mW.
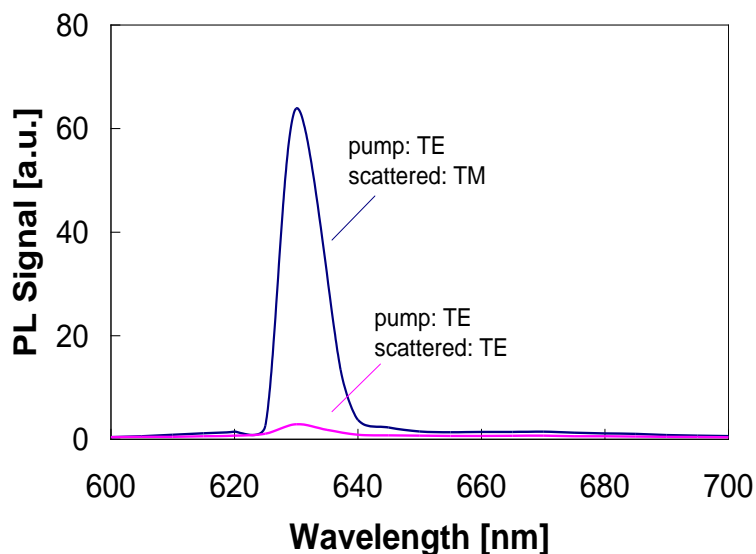
Figure 5.20 The effect of polarization on the PL signal when pump with TE mode. The tilt angle was θ=8°.

5.2.4   Graphene - Coated Infrared Screens for Bio-Detection

Here, various bio-materials are successfully deposited on graphene-coated metal screens and studied by use of infrared spectroscopy.

5.2.4.1 Graphene Based Sensor to Study Biotinylated Lipid Bilayer. Graphene-coated Infrared (IR) screens were used as new biosensing platforms to enhance IR absorption of bio-species. Mono and a few-layered graphene were successfully deposited into films on solid and perforated substrates. By combining the resonance properties of IR screens with the unique properties of graphene, fabrication of a new spectroscopic platform was achieved.

Freestanding, square shaped, electroformed copper screens were purchased from Buckbee-Mears. Those screens were 5 microns thick with periodicity of 15 microns and opening of 8 microns. Highly ordered pyrolitic graphite (HOPG) was purchased from SPI

Supplies. It's processing is detailed elsewhere [75]. For this purpose, biotinylated lipid bilayer were used along with streptavidin to mimic protein docking to a membrane surface. Synthetic phospholipid DMPC (1,2-dimyristoyl-*sn*-glycero-3-phosphocholine) and biotinylated lipid 16:0 Biotinyl Cap PE (1,2-Dipalmitoyl-sn-Glycero-3-Phosphoethanolamine-N-(Cap Biotinyl), sodium salt) were purchased from Avanti Polar Lipids (Alabaster, Alabama) in chloroform solutions and were stored in a freezer at 223 K prior to use. Preparation of multilamellar lipid vesicles is detailed elsewhere [90]. Streptavidin is a 53 kD tetrameric protein known for its extraordinarily strong affinity for the biotin moiety: the dissociation constant, $K_d \approx 10^{-15}$ mol/L, ranks the biotin-streptavidin complex as one of the strongest among the non-covalent interactions. DTAF-conjugated Streptavidin was purchased from Jackson ImmunoResearch Laboratories, Inc. (West Grove, PA) and dissolved in a 50 mM Na/K phosphate buffer at pH=7 (VWR International, West Chester, PA). DTAF-conjugated streptavidin was mixed with an excess of biotinylated lipids immediately before the experiments. The resultant bio films on graphenated IR screen were then inspected and characterized by using scanning electron microscope (FE-SEM).

The films were assessed by Raman spectroscopy: 514.5 nm line of Ar laser at 20 mW, a 75 cm single chamber spectrometer equipped with a cooled CCD camera at -15°C. In some cases longer wavelength Raman system (with 785 nm line of a diode laser) was also used. Additional assessments were made by infrared (IR) spectroscopy using Fourier Transform IR (FTIR) spectrometer.

Scanning electron microscope (SEM) picture of graphenated IR screen with the biotinylated bilayers/streptavidin complex is shown in Figure 5.21. Raman signal of the

graphenated screen was taken using Ar laser to determine the number of deposited graphene layers (Figure 5.22b). Due to the relatively large size of each opening, and the transparent nature of the film, it was easy to locate an opening under a microscope and assess its in-plane orientation. Monitoring the number of layers of graphene was made by examining its D` line (~2700 cm^{-1}). The peak shifts to lower frequencies and increases in intensity as the number of layer decreases. It is observed that the Raman line of Figure 5.18b is extraordinarily narrow when compared to lines shown in Figure 5.22a; the latter were obtained for graphene on a silicon substrate. In this spectral region, three-layer graphene exhibits a few close Raman lines. It seems that, one of these lines has been accentuated due to the resonating effects of the IR copper screen.
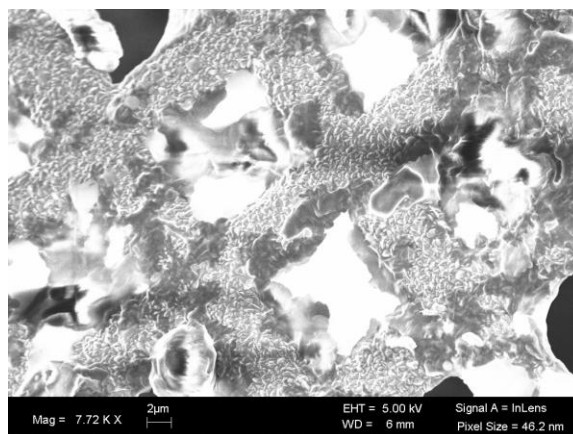
(a)
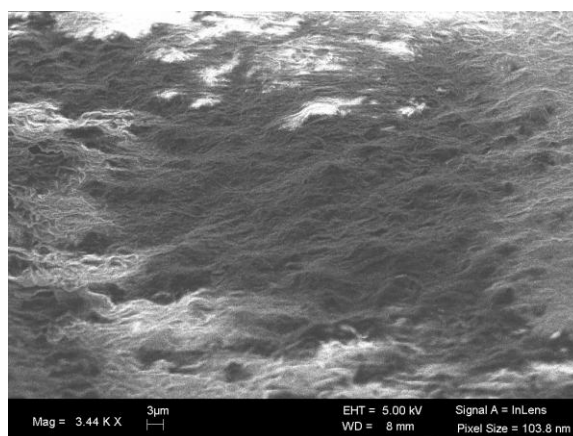
(b)
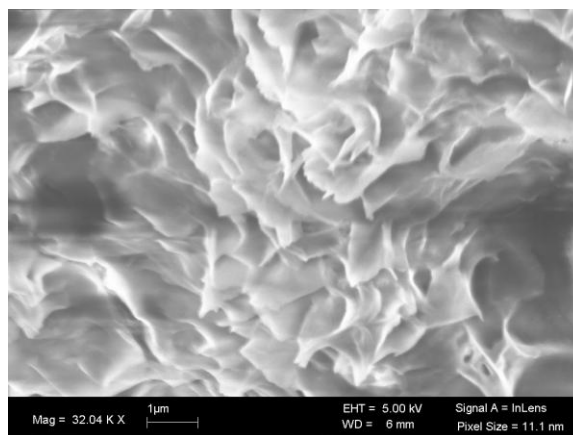
(c)

Figure 5.21 (a) Graphenated screen (b) with biotinylated lipid bilayer and (c) with biotinylated lipid bilayer and streptavidin.
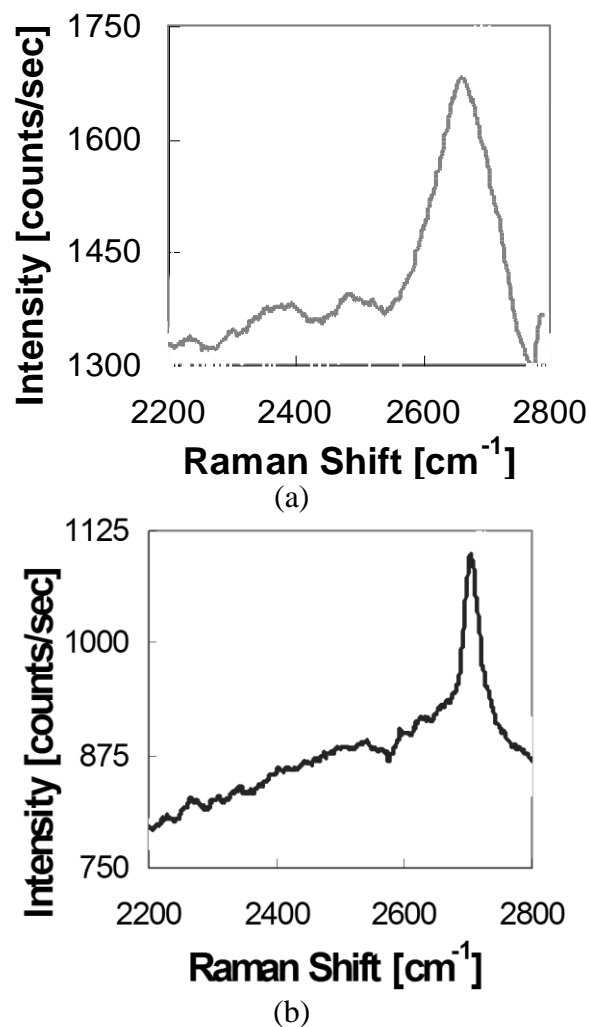
Figure 5.22 Raman spectra of graphene on (a) silicon wafer, (b) copper screen (pitch – 15 microns; opening – 8 microns); the peak has become substantially narrow.

Bionitylated lipid bilayer with conjugated streptavidin did not show any significant Raman peak when deposited on Si [Figure 5.23a]. Peaks were clearly visible only when the bio-species were placed on the graphenated copper screens [Figure 5.23b]. Clearer peaks are noted for the 15 μm screen compared with the 20 μm one. This is rather interesting and may be correlated with the relationship between the screen pitch and the equivalent surface Raman wavenumber.
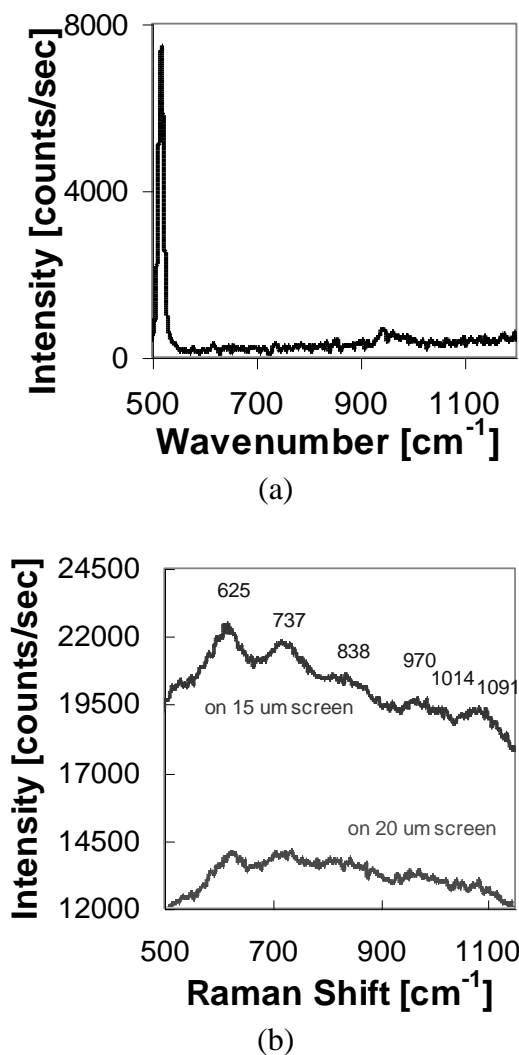
Figure 5.23. (a) Raman spectra of biotinylated lipid bilayer with streptavidin on a silicon substrate. The Raman line at 520 cm^{-1} is due to the silicon substrate. (b) Biotinylated lipid bilayer and streptavidin on graphenated copper screen (pitch – 15 μm; opening – 8 μm) as well as on graphenated nickel screen (pitch – 20 μm; opening – 11 μm).

Infrared transmissions and absorption of various graphenated screens were measured with and without the biotinylated lipid bilayers and streptavidin [Figure 5.24 and Figure 5.25]. The observed double peak for graphenated screens is the result of non-collimated incident IR beam constructed in many FTIR spectrometers [70]. Such non-collimation affects the scatterings of local polarization states, and specifically, those

which are within the plane of incidence (*H*-, or, *p*-polarization state). The deposition of only graphene resulted in an overall attenuation and peak shift of 15 cm^{-1}. This exhibits the high conductivity and good quality of the graphene layer. Generally, graphene lacks specific absorption in the 2-20 micron region. When deposited with bio-species the signal attenuated even further and the central peak shifted, as well. The absorbance was enhanced and the related peaks accentuated when the bio-films were deposited on copper screen with periodicity of 15 micron in comparison to other screens. These may be observed as small dips in the transmission curve. It is attributed that the enhancement is due to the resonating effect of this particular inductive screen.
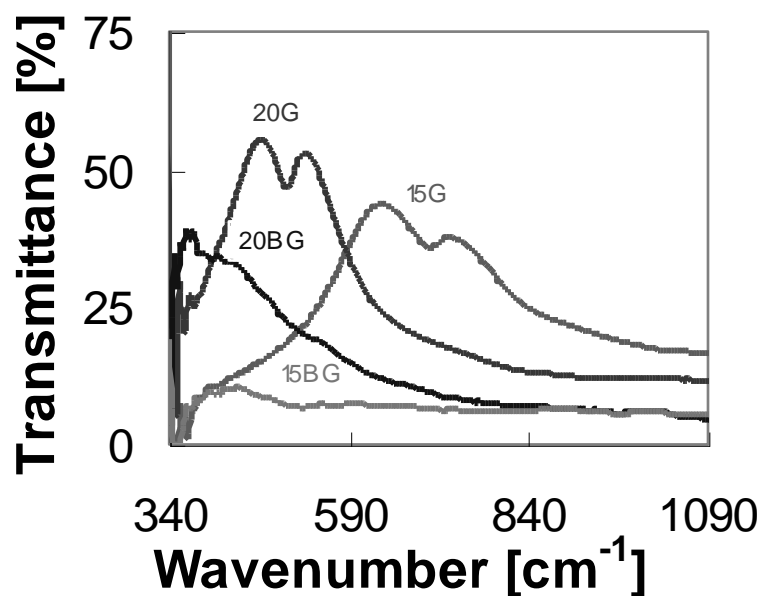
Figure 5.24 Transmission of graphenated screens with and without bio-species. The screen with the bio-species accentuates many of the spectral dips in the range of 1350 to 3350 cm^{-1}, compared to the relative smooth background of the screen without it. Here, 20G and 15G refer to graphenated screens with 20 μm and 15 μm periodicity, respectively. 20BG and 15BG refer same graphenated screens with bio-materials on them.
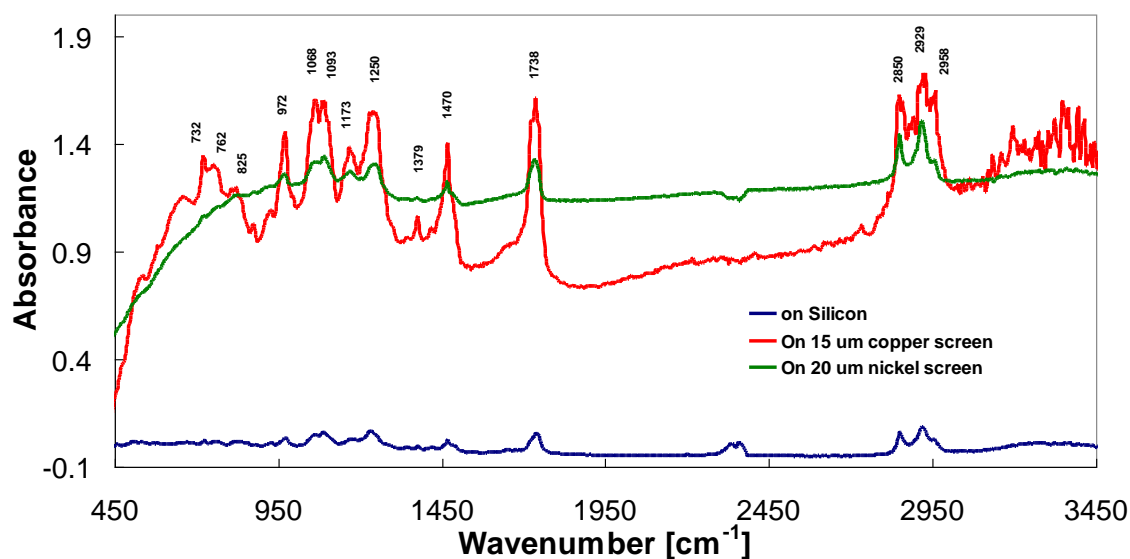
Figure 5.25 Absorbance of graphenated screens with bio-species. Bio-species on silicon substarte was also assessed as reference sample.

5.2.4.2 Graphene Based Sensor to DetectCytochrome c and *Salmonella Enterica*.

Here the efficacy of graphenated IR meshes was demonstrated by measuring Raman and

IR spectra of cytochrome c (Cyt c) from bovine heart and *salmonella enterica*.
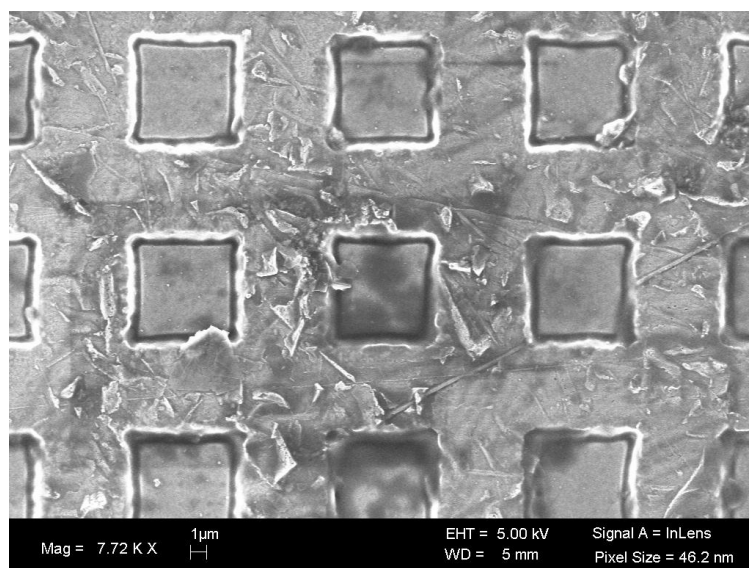
Figure 5.26 SEM picture of graphenated IR screen.

Scanning electron microscope (SEM) picture of graphenated IR screen is shown in Figure 5.26. SEM pictures of graphenated IR screen after depositing the Cyt c are shown in Figure 5.27. The left hand side picture shows the front side of the sample and the right hand side picture shows the same sample from the back side where suspended bio-material is clearly visible on top of graphene layer through the screen openings.
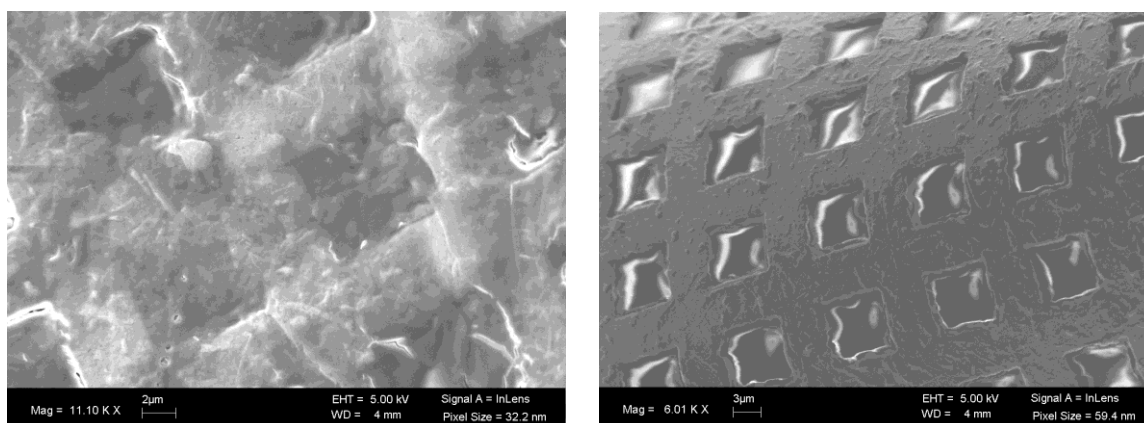
Figure 5.27 Scanning Electron Microscope picture of graphenated IR screen after depositing Cyt c. Left: the front side of the sample. Right: the same sample from the back where suspended bio-material is visible on top of graphene layer through the screen openings.

The Raman system was configured in a confocal arrangement, shown in Figure 5.28. The sample could be rotated and tilted as shown in the figure. Raman spectrum of Cyt c on graphenated IR screen is shown in Figure 5.29. Several peaks which are consistent with previously reported values are noted. In Figure 5.30, we show an angular dependence of 1345 cm^{-1} and 1570 cm^{-1} peaks. As for many bio-species, the peaks are situated on a large and broad background. A clear amplification of the peaks is noted as a function of in-plane rotations (azimuthal angle, ϕ) and tilt angle, θ. The background signal was amplified as well. The issue of background 'noise' is sometimes ignored in

evaluating SERS amplification factors. To overcome this problem we represent data as Signal-to-Noise Ratios (SNR) instead of just intensity values as a partial remedy. The SNR for each angle was evaluated as the ratio between the peak values to its nearest background levels.
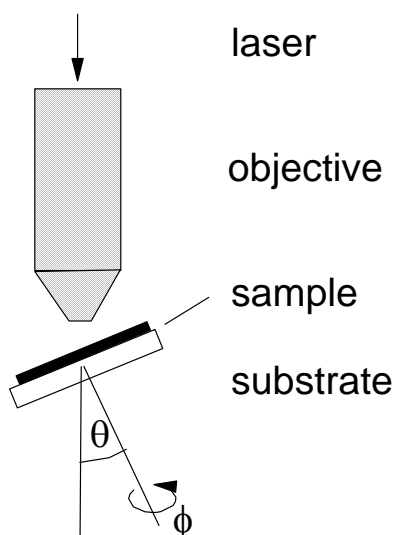
Figure 5.28 Experimental arrangement for angle-dependent Raman spectroscopy.
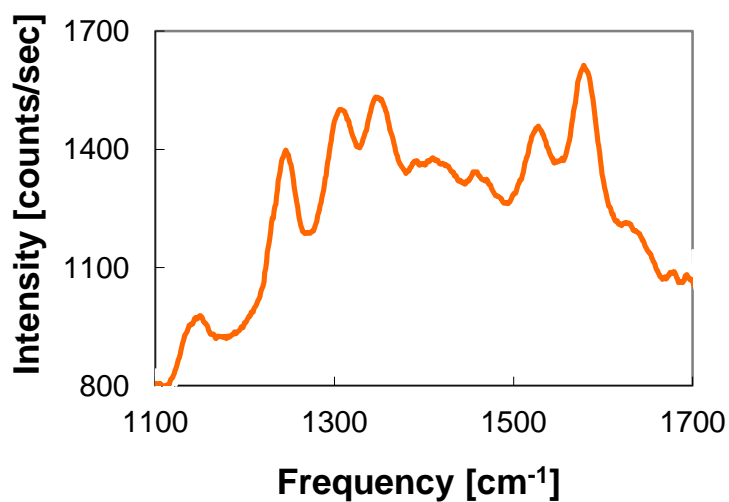
Figure 5.29 Raman spectrum of Cyt c, deposited on graphenated IR screens.
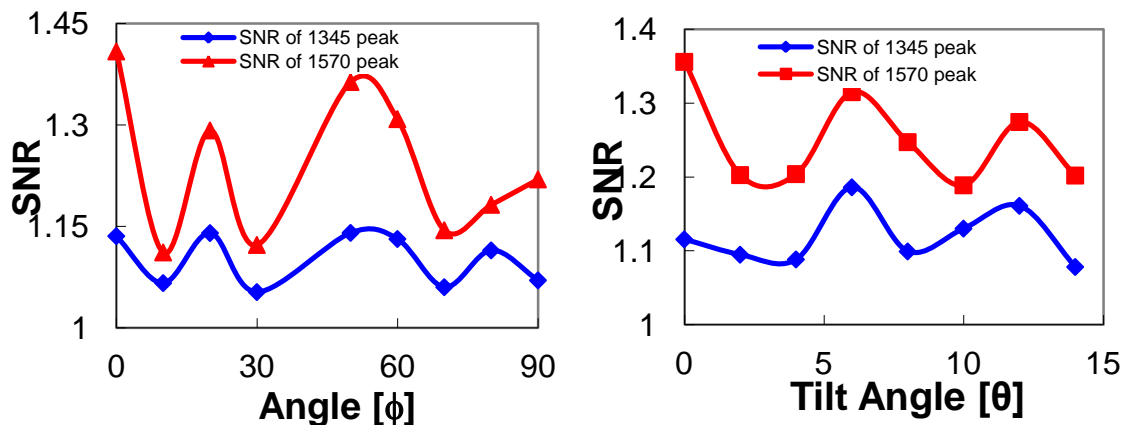
Figure 5.30 Signal to noise ratio of 1350 and 1570 peaks of Cyt c, deposited on graphenated IR screens with changing rotational angle, φ (left) and tilt angle, θ (right).

Absorbance of Cyt c on graphenated screens was measured by use of FTIR spectrometer (Figure 5.31). Graphene lacks specific absorption in the 2-20 micron region. This exhibits the high conductivity and good quality of the graphene layer. When deposited with Cyt c the signal varied as a function of sample orientation with respect to the incident IR beam. Two absorption peaks are noted at 1660 cm^{-1} and 1552 cm^{-1}, respectively. Their respective SNR values are shown in figure 6. We attribute these SNR variations to the resonating orientation of the inductive screen [70].
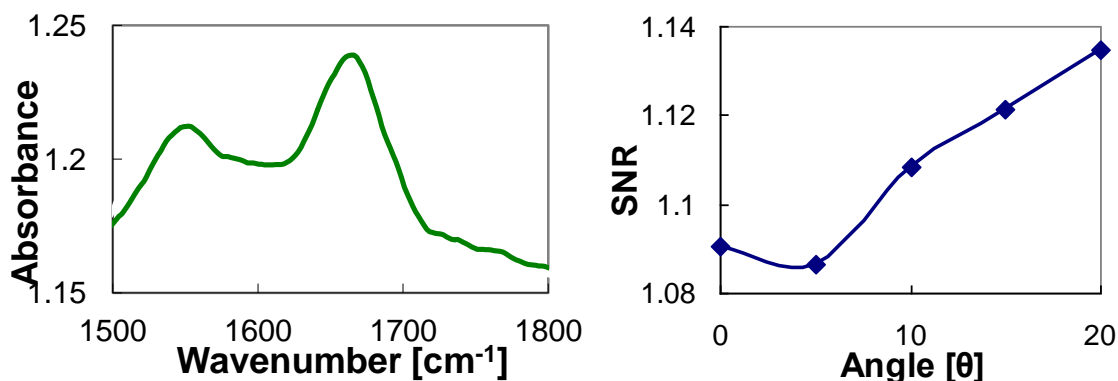
Figure 5.31 Left: Typical Infra Red (IR) spectrum of Cyt c, deposited on graphenated IR screen. Right: signal to noise ratio of 1660 cm^{-1} peak as a function of tilt angle, θ.

Salmonella enterica (a gram-negative bacterium related to *E. coli* which is a pathogen causing disease on humans and other animals). 10 μL of highly concentrated was mixed with 1 mL of DI water and then 1 μL of solution was taken to cover each 1 cm^2 area of screen. the peaks are situated on a large and broad background. A clear amplification of the peaks is noted as a function of tilt angle, θ. Similar measurements were performed for salmonella. Two prominent peaks were found at 1377 cm^{-1} and 1653 cm^{-1} for 0^0 tilt [Figure 5.28] [94]. When the sample further tilted to 10^0, all other peaks were accentuated. This enhancement was not observed for 12^0 or 14^0 tilts [Figure 5.33]. The background signal was amplified as well. The issue of background 'noise' is sometimes ignored in evaluating SERS amplification factors. As a partial remedy to this problem the data has been shown as Signal-to-Noise Ratio (SNR) instead of just intensity peak values. The SNR value for each angle was evaluated as the ratio between the peak values to its nearest background level.
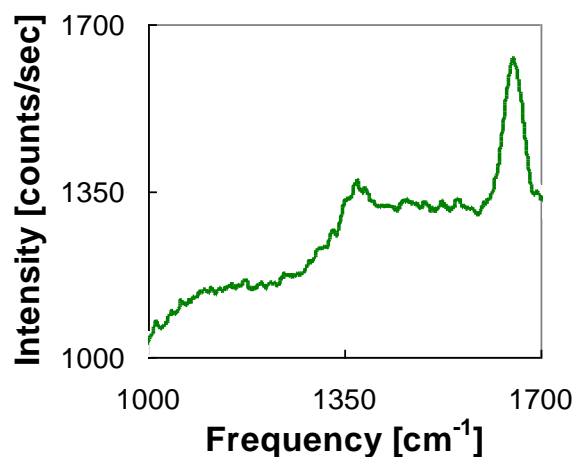
Figure 5.32 Raman spectrum of *salmonella enterica* at 0^0 deg tilt, deposited on graphenated IR screens. Two prominent peaks were observed at 1377 cm^{-1} and 1653 cm^{-1} respectively.
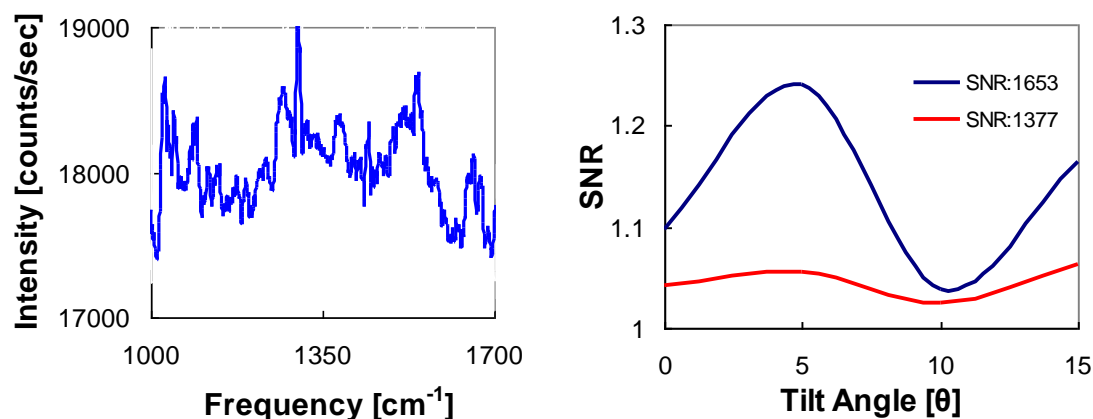
Figure 5.33 Raman spectrum of *salmonella enterica* at 10^0 tilt (right). Signal to noise ratio of 1377 cm^{-1} and 1653 cm^{-1} peaks of *salmonella enterica*, which was deposited on graphenated IR screens, as a function of tilt angle, θ (right) in degrees.

5.2.4.3 Graphene Based Sensor to Detect Flu Viruses. Swine influenza virus (H1N1) has been proven fatal to humans. Avian influenza virus (H5N1) has been known to inflict devastating damage to poultry industries around the world. Mutations in the hemagglutinin (HA1) area of the avian flu were attributed to its ability to bind to human receptors. Since the binding between the HA1 to its preferred receptor is made via H-bonds we hypothesized that it would carry a unique infrared (IR) signature. However, such IR signals are weak and require signal amplification. Signal amplification may be achieved by placing the sample on Plasmons' carrying platforms. Indeed, receptor-bound hemagglutinin (HA1) exhibited strong IR absorption peaks. Yet, contrary to simulations, a weak binding affinity was also observed between HA1(H5N1) and the human receptor without necessitating mutations. On the practical side, almost monolayer thick films were used, yet obtained sensitivity levels better than what is accustomed to by analytical methods. On the fundamental side, the role of hydrogen bonds (H-bonds) of influenza viruses in wet systems deserves a second look.

Binding of HA to sialylated glycans is the first step to virus infection [95-99]. On the avian flu side, transmission from birds to humans is believed to be closely associated with the ability of the HA to switch its preference from α2-3 sialylated glycans (α2-3) to α2-6 sialylated glycans (α2-6), which are extensively expressed in the human upper respiratory epithelia [100-106]. Crystal structures of HA from H1 (swine) and H5 (avian) and their complexes with oligosaccharides have provided useful information for such interactions [107-109], raising hope that minute differences in these interactions will be helpful to distinguish between different. Despite advances in key monitoring technologies [110], a dire need arises to characterize the saccharide bound HA by use of rapid, relatively simple non-invasive spectroscopic tool, such as, infrared (IR) spectrometer, and in an environment closely mimicking its expression location. Following spectroscopic changes upon (and perhaps during) binding events is the first step towards understanding of the evolving hydrogen-bonds involved.

In the experiments, virus receptors were imbedded in lipid membranes. Cellular plasma membranes are essential structural elements of eukaryotic cells, which define the cells' outer surface. The primary structural elements of a plasma membrane are amphiphilic phospholipid molecules, self-assembled into sheet-like structures, which was incorporated onto a bio-compatible micron-size periodic hole structures. By imbedding sialosaccharides in the membrane there is not only the immobilization of the receptors but also there is an attempt to mimic the natural binding process between protein and ligand. In general, detecting and understanding the interactions of analytes with lipid membranes represents an essential task for drug targeting.

All chemicals were purchased from Sigma-Aldrich (St. Louis, MO) and used as received unless indicated otherwise.

Hemagglutinin (HA1) of H1N1 (HA1 (A/California/06/09) (H1N1) (SWINE FLU 2009) (aa 18-344)) and H5N1 (HA1 (H5N1), 6xHis tagged Hemagglutinin (A/Vietnam/1203/2004) (aa 1-345)) viruses were purchased from Enzyme Incorporated: 10 μL of the HA1 protein was mixed with 240 μL of phosphate buffer saline, PBS (pH 7.4). The molar concentration of HA1 in the solution was 1 μM. The amount of bound HA1 to its receptor is unknown. Figure 4.35(a) below has been obtained with similar, yet untagged HA1 purchased from ProScience.

Tri-saccharides (tr40, Neu5Gca2-3Galb1-4GlcNAcb-Sp 3'SLN (Gc) and tr43, Neu5Gca2-6Galb1-4GlcNAcb-Sp 6'SLN (Gc)) were received from the Functional Glycomics Center, Core D (SCRIPP Inst, San Diego). 1 mg of either obtained saccharide was dissolved in 1 mL of water. The acquired molar concentration of either saccharide was 1.3 mM.

Synthetic zwitterionic phospholipid 1,2-dimyristoyl-*sn*-glycero-3-phosphocholine (DMPC) was purchased from Avanti Polar Lipids (Alabaster, AL). Multilamellar lipid were prepared by mixing chloroform solutions of DMPC. Subsequently, the chloroform was removed by a rotary evaporator and repeated washing yielding a thin lipid film on the surface of a round bottom flask. 50 mM Hepes buffer, pH 7.0 was added to the flask. The concentration of lipids in aqueous media was 30 mg ml^{-1}. 15 mg of DMPC were mixed with 2 mL of water. The final molar concentration of the DMPC was 22 mM. Films were deposited by drop casting at 30 $^{\circ}$C. The DMPC were thoroughly washed with PBS buffer solution prior to administering the HA1s.

Graphenated IR screens were made by coating a commercial (e-forming Inc., USA) copper screens (square array of holes, 7.6x7.6 micron squares with a pitch of 12.7 microns and screen thickness of 4 microns) with highly oriented pyrolitic graphite (HOPG) purchased from SPI, PA USA. The graphitic layer was then subjected to a thinning process [75] which culminated in a 2-4 layers of graphene on the copper screen as attested to by Raman spectroscopy. The resonance frequency of graphene-coated screens is peaked at 600 cm^{-1}. The absorption spectrum is fairly flat beyond 1000 cm^{-1}, the spectral region of interest.
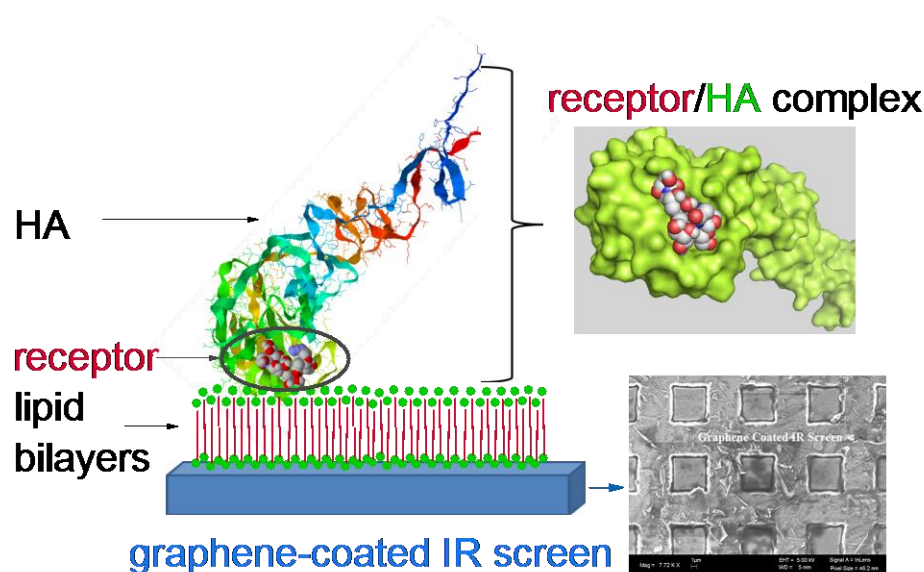
Figure 5.34 Schematics of the platform layout.

Here the approach is to assess the IR absorption of viruses bound to receptors, which in turn, are imbedded on signal amplifying platforms. The initial platform is schematically shown in Figure 5.34. The platforms are made of micron size periodic openings in metal films (similar to metal grids used for electron microscopy). The metal meshes were coated with graphene - monolayer or, few layers thick graphite [75, 111].

The signal amplification takes advantage of surface electromagnetic (EM) modes known as surface plasmon polariton (SPP) waves [112]. Coupling of the incident electromagnetic wave (the IR beam) to the platform is enabled by the periodic structure of screen opening. The surface waves result in an increased coupling between the incident IR beam and the bound receptors. Due to the periodicity of the hole pattern, fundamental and higher order harmonics of the surface modes are involved in this process, enabling molecular interrogation over a wide wavelength range. The graphene is a perfect molecular holder since it lacks specific IR absorption and is bio-compatible. The graphene coating is thin enough to allow optical transmission, yet conductive enough to enable the propagation of SPP waves throughout the screen. The substrates are further deposited with synthetic zwitterionic phospholipid 1,2-dimyristoyl-*sn*-glycero-3-phosphocholine (DMPC). The trisaccharides (tr43 containing α2-6, aimed at binding HA1 from the swine virus, and tr40 containing α2-3, aimed at binding the avian flu virus) are incorporated in the DMPC. Scanning electron microscope ascertained the full coverage of the lipid membrane [111, 79]. Similar recipe [106] for other lipids resulted in the formation of bilayers on graphene and on glass.

This signal amplifying platforms enabled to use concentration levels, which are by far smaller than what is accustomed to in similar spectral or chemical analysis. The starting molar concentration of HA1 in the stock solution was 1 μM compared to *e.g*., 4 μM used in [113].

IR absorption spectra of bound receptors exhibited new IR peaks. In Figure 5.35(a) it is shown that the IR absorption spectra of HA1 of H1N1 and H5N1 on the avian receptor tr40. Clearly, the HA1(H5N1) interacts with the tr40 while the

HA1(H1N1) is not: newly formed IR absorption bands at 1400-1650 cm^{-1} and at 3000-3800 cm^{-1} appear for HA1(H5N1). IR peaks appear only upon coupling between HA1(H1N1) and the human receptor tr43 as shown in Figure 5.35(b). There is a small but clear affinity of the HA1(H5N1) to the human receptor tr43 indicating a weak binding after washing the sample with a buffer solution.
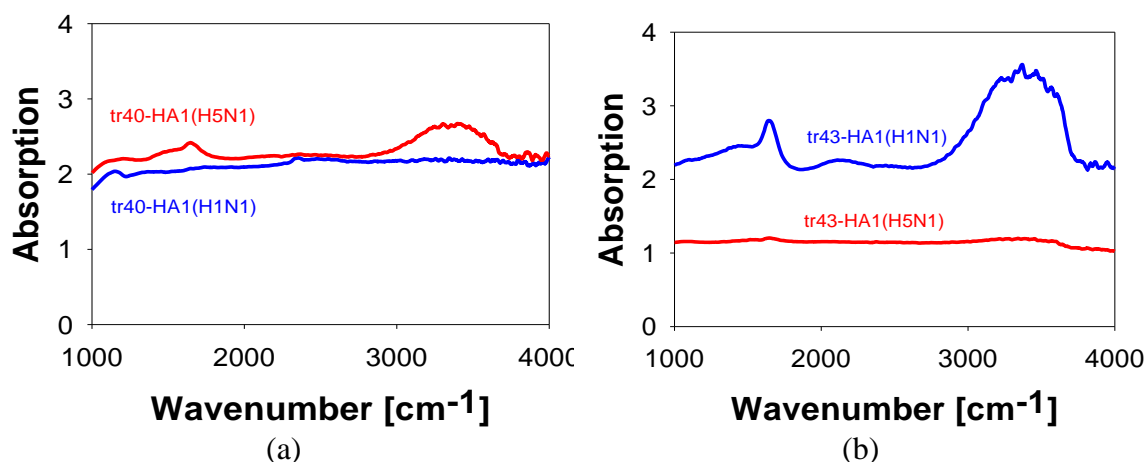
Figure 5.35 IR absorption spectra of HA1 from either H1N1 or H5N1 on bilayers situated on graphenated screens. The data is expressed as the negative logarithm of transmission, or, $-log$(transmission) and is referenced to the absorption of the receptor imbedded lipid bilayers: (a) Bilayers with tr40 (α2-3) receptor. (b) Bilayers with tr43 (α2-6) receptor. Note the weak affinity of tr43 to HA1(avian).

Infrared peak fitting is shown in Figure 5.36. For convenience, the constant background from the spectra was removed. In addition, the absorption was referenced to a platform with only the receptor imbedded lipid bilayer. That is the reason why the DMPC signature [20] is missing from the data. IR data were obtained for partially wet samples. The samples were washed with buffer solution prior of taking the IR absorption data.

Infrared Peak Analysis: various peaks were fitted by gaussian distributions: Tr40-HA1(H5N1): there exist three peaks at 1500 cm^{-1}: 1442 (CH$_3$), 1635 and 1673 cm^{-1} (bent vibrations of H$_2$O and C=O). The broad peak at 3400 cm^{-1} may be fitted with five peaks: 3078 (C–H), 3292, 3450 and 3585 (H–O–H) and 3797 cm^{-1} (N–H). The region between these peaks may be fitted with small and broad two peaks at 1921 (=C) 2454 cm^{-1} (O–H). One small peak may also be identified at 1162 cm^{-1} (CH$_2$).
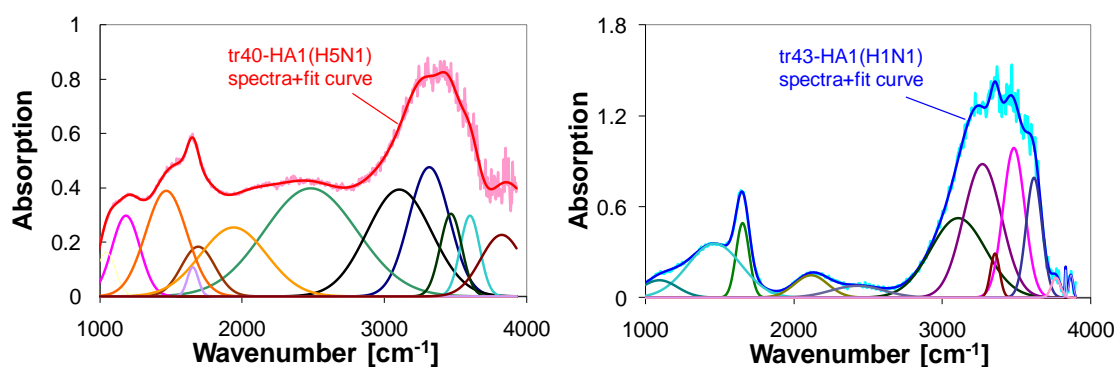
Figure 5.36 Peak fit for the various IR spectra for bound proteins.

Tr43-HA1(H1N1): there exist two peaks at 1500 cm^{-1}: 1438 (CH$_3$) and 1641 cm^{-1} (mostly bent vibrations of H$_2$O). The broad peak at 3400 cm^{-1} may be fitted with six peaks: 3085 (C–H), 3255, 3344, 3467 and 3608 (H–O–H) and 3856 cm^{-1} (N–H). The region between these peaks may be fitted with small and broad two peaks at 2090 (=C) and 2422 cm^{-1} (O–H). One small peak may also be identified at 1064 cm^{-1} (CH$_2$).

After one hour of drying in air, the bound tr40-HA1(H5N1) and tr43-HA1(H1N1) exhibited somewhat reduced peaks' amplitude, yet all peak characteristics were intact. These features do not appear for saliva, or for DMPC [Figure 5.37]. Other notable features for both viruses are the down-shift of the ~1640 peak by ~15 cm^{-1} which

indicates the vibrations of other than just water in the sample. The two small peaks at 2848 and 2918 cm^{-1} after dehydration are attributed to the fact that the reference sample (DMPC with imbedded receptor) was initially wet as opposed to the dehydrated sample.
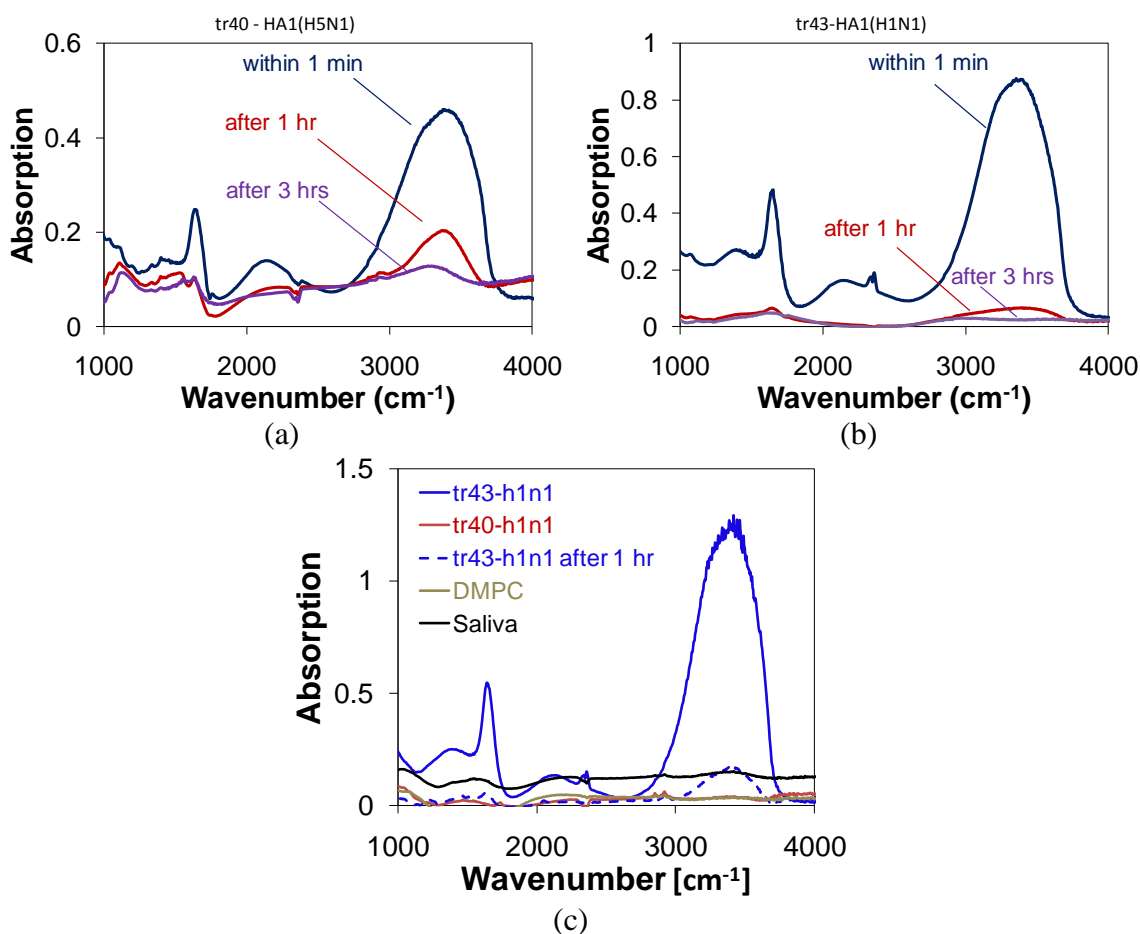
Figure 5.37 (a) Time dependent spectra of tr40-HA1(H5N1) (b) Time dependent spectra of tr43-HA1(H1N1). (c) Spectra of various films coating the graphene-coated platforms. Data was normalized to DMPC+receptor.

Further indication to the role of water was made by replacing the buffer solution with deuterated water, D$_2$O as shown in Figure 5.38. The stock solution was diluted 25 times with D$_2$O and the DMPC on the graphene coated structures was washed thoroughly

with D_2O as well. The main features at 3400 cm^{-1} and at 1600 cm^{-1} remained albeit modified a bit.
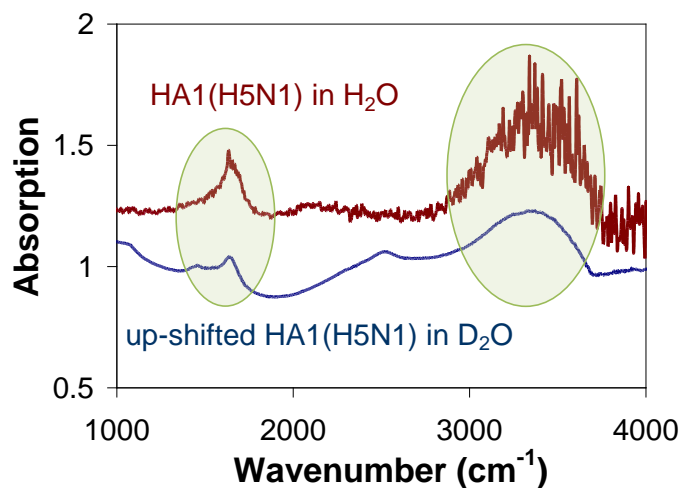
(a)
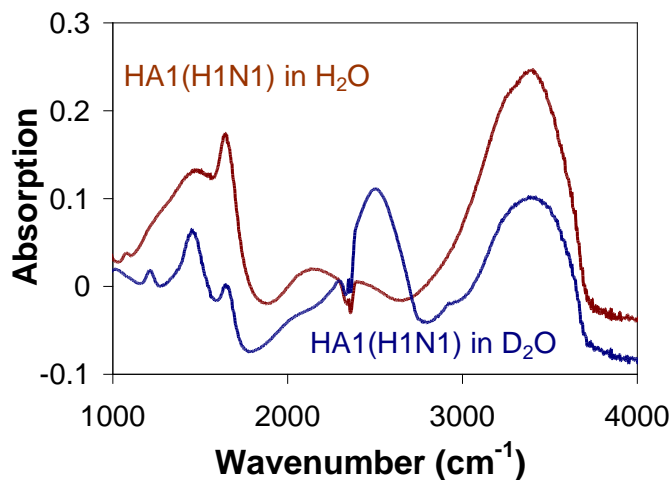
(b)

Figure 5.38 (a) Comparison between tr40-HA1(H5N1) in water (buffer solution) and in D_2O. The peak at 2500 cm^{-1} is attributed to D_2O. The curve for HA1(H5N1) in D_2O was up-shifted for convenience. (b) Comparison between tr43-HA1(H1N1) in water (buffer solution) and in D_2O. The peak at 1450 cm^{-1} has increased in consistence with the effect of D_2O. The peaks at 1200 and 2500 cm^{-1} are attributed to D_2O. For D_2O at 3000-3800 cm^{-1}, note the small shift to larger frequencies for both samples.

Homology modeling and docking simulations: All docking simulations were made using Autodock 4.2 [114] (Scripps Research Institute, USA). The ligand and macromolecule files were prepared using Autodock tools (ADT) 1.5.4 (Scripps Research Institute, USA). Autodock 4.2 and ADT 1.5.4 [23] were run in Cygwin shell-based (http://cygwin.com) windows platform, (Win-XP, CPU i7, 12 GB RAM, ATI Raedon 1GB). For H5N1 modeling, crystal structure of Hemagglutinin H5N1 (pdb id: 2FK0) was used as the macromolecule. Due to unavailability of a crystal structure of hemagglutinin of swine origin Influenza A virus A/California/06/2009(H1N1))(Cal06) an homology model of the same was generated using the Swiss-model workspace [115] (http://swissmodel.expasy.org) and was based on published crystal structure of a swine originated Influenza A virus (A/California/04/2009(H1N1)) (cal04) (pdb id: 3AL4). "Alignment mode" was used to build the homology model because of high sequence identity [Figure 5.39] of Cal06 with Cal04. Both macromolecules were prepared by similar fashion: removal of water molecules, addition of hydrogen atoms, merging of non-polar hydrogen atoms and addition of Gasteiger charges were obtained using ADT1.5.4. Macromolecules were treated as rigid molecules; no flexible residues were prepared. A 60X60X60 grid with a 0.375 Å spacing was set and was centered in the active site of H5N1. The energy minimized (MM2) pdb files of ligands TR-40 and TR-43 were prepared using Chem-bio3D Ultra v.12.0. Automated merging of non-polar hydrogen atoms and addition of Gasteiger charges was made using ADT 1.5.4. Active torsions were set to 22 for both TR40 and TR43 using the option "most atom" and random values were selected for the initial states. Docking experiments were performed using a Lamarckian genetic algorithm with 100 docks, an initial population of 300

individuals and performing 25000000 energy evaluations and 27000 generations. Docking cluster analysis was performed with 1.50Å root mean square distance (RMSD). The figures were developed using pymol (4 The PyMOL Molecular Graphics System, Version 1.2r3pre, Schrödinger, LLC) and python molecular viewer (PMV) [116].

```
Cal04           MKAILVVLLYTFATANADTLCIGYHANNSTDTVDTVLEKNVTVTHSVNLLEDKHNGKLCK 60
Cal06           MKAILVVMLYTFATANADTLCIGYHANNSTDTVDTVLEKNVTVTHSVNLLEDKHNGKLCK 60
1918Sc          MEARLLVLLCAFAATNADTICIGYHANNSTDTVDTVLEKNVTVTHSVNLLEDSHNGKLCK 60
2004vieth5n1    ------------ADPGDQICIGYHANNSTEQVDTIMEKNVTVTHAQDILEKKHNGKLCD 47
                 :  .* :**********: ***::********: ::**..******.

Cal04           LRGVAPLHLGKCNIAGWILGNPECESLSTASSWSYIVETPSSDNGTCYPGDFIDYEELRE 120
Cal06           LRGVAPLHLGKCNIAGWILGNPECESLSTASSWSYIVETSSSDNGTCYPGDFIDYEELRE 120
1918Sc          LKGIAPLQLGKCNIAGWLLGNPECDLLLTASSWSYIVETSNSENGTCYPGDFIDYEELRE 120
2004vieth5n1    LDGVKPLILRDCSVAGWLLGNPMCDEFINVPEWSYIVEKANPVNDLCYPGDFNDYEELKH 107
                   * *: ** * .*.:***:**** *: : ....******.... *. ****** *****:.

Cal04           QLSSVSSFERFEIFPKTSSWPNHDSNKGVTAACPHAGAKSFYKNLIWLVKKGNSYPKLSK 180
Cal06           QLSSVSSFERFEIFPKTSSWPNHDSNKGVTAACPHAGAKSFYKNLIWLVKKGNSYPKLSK 180
1918Sc          QLSSVSSFEKFEIFPKTSSWPNHETTKGVTAACSYAGASSFYRNLLWLTKKGSSYPKLSK 180
2004vieth5n1    LLSRINHFEKIQIIPK-SSWSSHEASLGVSSACPYQGKSSFFRNVVWLIKKNSTYPTIKR 166
                  ** :. **:::*:** ***..*::. **::**.: * .**::*:::** **...:**.:.:

Cal04           SYINDKGKEVLVLWGIHHPSTSADQQSLYQNADTYVFVGSSRYSKKFKPEIAIRPKVRDQ 240
Cal06           SYINDKGKEVLVLWGIHHPSTSADQQSLYQNADAYVFVGSSRYSKKFKPEIAIRPKVRDQ 240
1918Sc          SYVNNKGKEVLVLWGVHHPPTGTDQQSLYQNADAYVSVGSSKYNRRFTPEIAARPKVRDQ 240
2004vieth5n1    SYNNTNQEDLLVLWGIHHPNDAAEQTKLYQNPTTYISVGTSTLNQRLVPRIATRSKVNGQ 226
                  ** * : :::*****:***  .::* .****. :*: **:*  .::: *.** *.**..*

Cal04           EGRMNYYWTLVEPGDKITFEATGNLVVPRYAFAMERNAGSGIIISDTPVHDCNTTCQTPK 300
Cal06           EGRMNYYWTLVEPGDKITFEATGNLVVPRYAFAMERNAGSGIIISDTPVHDCNTTCQTPK 300
1918Sc          AGRMNYYWTLLEPGDTITFEATGNLIAPWYAFALNRGSGSGIITSDAPVHDCNTKCQTPH 300
2004vieth5n1    SGRMEFFWTILKPNDAINFESNGNFIAPEYAYKIVKKGDSTIMKSELEYGNCNTKCQTPM 286
                  ***:::**:::*.* *.**:.**::.* **: : : ..* *: *:    :***.****

Cal04           GAINTSLPFQNIHPITIGKCPKYVKSTKLRLATGLRNIPSIQSRGLFGAIAGFIEGGWTG 360
Cal06           GAINTSLPFQNIHPITIGKCPKYVKSTKLRLATGLRNVPSIQSRGLFGAIAGFIEGGWTG 360
1918Sc          GAINSSLPFQNIHPVTIGECPKYVRSTKLRMATGLRNIPSIQSRGLFGAIAGFIEGGWTG 360
2004vieth5n1    GAINSSMPFHNIHPLTIGECPKYVKSNRLVLATGLRNSPQRERR---------------- 330
                  ****:*:**:****:***:*****:*.:* :****** *. : *
```

Figure 5.39 Sequence comparison of Cal0409 HA with Cal0609, 1918 Spanish flu and Viet04 HA.

An example of a bound tri-saccharide to HA1 is shown in Figure 5.40(a) and (b). Shown are the bound ligand-protein complex and the various distances as assessed by docking experiments. Bound complexes exhibited negative binding energy: tr43-HA1(H1N1) it was -2.34 kcal/mol and for tr40-HA1(H5N1) it was -1.87 kcal/mol. The

cross experiments exhibited the following: for tr40-HA1(H1N1) it was +354.72 kcal/mol and for tr43-HA1(H5N1) it was +4.93 kcal/mol. Detailed assessments of the various distances between receptor and protein are provided in Table 5.1 (a) and (b).

The concentration levels used for this study are by far smaller than what accustomed to for both spectroscopy and analytical techniques. This is due to the use of extremely thin layers on signal enhancing structures. In fact, thick layers (including layer of water) mask the IR features. Secondly, the lipid membrane's features arenormalized out and the IR protein's features are not easily detected. The latter is due to low protein concentration and the relatively large proximity of the protein from the electromagnetic surface waves. Such construction accentuated the IR absorption signal from the newly formed H-bonds between protein and ligand. Thirdly, the concentration of the protein is by far smaller than the concentration of ligands, almost by a factor of 1000 smaller (see further discussion below).

The large peak in the 3000-3800 cm^{-1} region is typically attributed to water (obviously made of H-O-H bonds). In contrast to many other experiments which are performed with bulk wet samples, here extremely thin layers were used, on the order of a few monolayers. All water dissolved films exhibited *weak* peaks at the 3400 cm^{-1} region in contrast to a very strong band when a binding event, between the HA1 and receptor, occurred. Saliva taken from HG did not show a strong 'water' peak either. In addition, and as alluded to by Figure 5.37, upon drying, the IR peaks fainted but did not disappeared. This means that the binding between protein and ligand was relatively strong and the decaying signal should be attributed to the disintegration of the lipid

membrane. Washing the sample after 3 hours of drying in air eliminated the IR signal completely.

(a)

(b)

Figure 5.40 (a) HA1(H5N1) bound to tr40: Key interaction distances between ligand and protein are highlighted blue (left). Bound receptor (right). (b) HA1(H1N1) bound to tr43: Key interaction distances between ligand and protein are highlighted blue (left). Bound receptor (right).

Table 5.1 (a) Assessed Distances Between Receptor and Protein without Water Mediation. When Bound, the Minimal Distance is Less than 2 Å. When Unbound, the Minimal Distance Exceeds 2.5 Å.

H5n1-tr40	Interaction	type of interaction	Distance	H5n1-tr43	Interaction	type of interaction	Distance
	Gln226	O….H-O	1.79		Gln226		>7
		O….H-O	2.7		Gly 225		>7
		O….H-O	1.98		Arg216		>10
	Gly 225	O….H-O	2.11		Glu 190		>8
	Arg216		16.88		Gly 228		>9
	Glu 190		> 4.8		His 183		>8
	Gly 228		>6.0		Leu 194		>7
	His 183		>4.9		Lys 193	O…H-N	2.56
	Leu 194		>4			O…H-N	2.76
	Lys 193	N-H…O	2.56			O…H-N	3.11
		N..H-O	2.82		Lys222		>8
	Lys222		>4		Ser136	O…H-N	4.07
	Ser136		>4		ser137	O…H-N	3.33
	ser137		>4		ser221		>19
	ser221		>4		ser227		>8
	ser227		>4		trp153		>7
	trp153		>4		tyr98		>8
	tyr98	O…H-O	2.5		tyr195		>9
		O…H-O	3.69		Val135	O-H…O	3.34
	tyr195		>4			O…H-N	3.92
	Val135	O…H-O	2.63			O…H-O	4.04
		O…H-O	3.03				

(a)

Table 5.1 (b) Assessed Distances Between Receptor and Protein without WaterMmediation. When Bound, the Minimal Distance is Less than 2 Å. When Unbound, the Minimal Distance Exceeds 2.5 Å.

H1n1-tr40	Interaction	type of in	Distance
	ala151		>7
	ala152		>12
	ala203		>5
	asp204	O-H...O	3.8
	asp239		>8
	gln 240		>6
	glu241		>9
	gly242		>8
	His197		>6
	Leu168		>5
	Leu208		>4
	lys136		>9
	lys147	O-H...O	2.98
	lys159		>5
	lys 170		>4
	lys171		>5
	lys236		>11
	Ser200		>7
	Ser207	O-H...O	3.03, 3.31
	thr150		>5
	Thr201		>7
	tyr108		>6
	Tyr209		>4
	val169		>4

H1n1-tr43	Interaction	type of interaction	Distance
	ala151		>6
	ala152		>4
	ala203		>4
	asp204	O-H...O	2.91
		O-H...O	3.88
	asp239	O-H...O	2.61
		O-H...O	1.98
	gln 240	O-H...O	3.42
		O-H...N	3.99
	glu241	N-H...O	3.52
		O-H...N	3.9
	gly242		>4
	His197		>4
*	Leu168		>4
	Leu208		>4
	lys136		>11
	lys147		>4
*	lys159		>4
	lys 170		>4
	lys171		>4
	lys236	N-H...O	3.88
	Ser200	O-H...O	3.83
	Ser207	O-H...O	3.47
		O-H...O	2.6
	thr150		>4
	Thr201	O-H...O	2.89
		O-H...O	3.03
	tyr108		>5
	Tyr209		>4
	val169		>4

(b)

Indeed, the frequencies of the bound complexes coincide with IR water lines. The possibility that some or all of the IR peaks are associated with water molecules could be tested by using D_2O instead of the buffer solution. As shown in Figure 5.38, the band at

3000-3800 cm^{-1} decreased a bit and shifted towards the larger frequencies regime for both viruses. The band at 1645 cm^{-1} substantially decreased for HA1(H1N1) but not for HA1(H5N1): this means that the HA1(H1N1) line had a large contribution from bent vibrations of water molecules with only a small contribution from Amide I while the reverse is true for HA1(H5N1).

The intensity of IR peaks for bound receptors in H_2O was substantially larger than for peaks obtained with free H_2O, free D_2O molecules, a film of only buffer solution, saliva, or samples treated with D_2O. This means that the enhanced IR absorption may be attributed to (a) only water-like molecules trapped between ligand and protein or (b) relatively strong hydrogen bonds [117]. Hypothesis (a) is not supported by docking experiments: bound receptors were associated with negative binding energy (for tr43-HA1(H1N1) it was -2.34 kcal/mol and for tr40-HA1(H5N1) it was -1.87 kcal/mol) yet very short distanced H-bonds, below 2 angstroms, which cannot support trapped water molecules between them. Based on the strength of the absorption and the selective response to D_2O we conclude that peaks ought not to be solely attributed to free or bound water molecules.

Docking simulations also suggested a relatively short interaction distance, on the order of 3 angstroms, between unbound protein and receptor. There we distinguish between two cases: a very large positive free energy (+354.72 kcal/mol for swine flu – avian receptor) and therefore an unstable structure; and a positive, yet small free energy (+4.93 kcal/mol for avian flu – human receptor). The latter interaction could be, in principle mediated by water and hence result in weak IR absorption peaks. It is interesting to note that the distances between the avian HA1(H5N1) flu and the human

receptor tr43 are smaller than the corresponding distances between the swine HA1(H1N1) flu and the avian receptor, tr40. This may also indicate a weak interaction between the avian influenza virus to the human receptor, as alluded to by the weak IR absorption peaks [Figure 5.35]. This is the most direct evidence of such interaction without necessitating to mutation and/or virus adaptation [118].

Graphite is hydrophobic. The lipid bilayers heads are known to be hydrophilic. The good mixing of receptors within the lipid bilayers is probably due to hydrophobic termination of the receptors. Scanning electron microscope does not reveal excess lipid agglomeration. That limits the overall coverage of the DMPC to basically two layers. A reference experiment with biotinylated lipid bilayers and streptavidin on SiO_2/Si and on graphene showed that the IR peaks match almost one to one [111] so it could be concluded that lipid bilayers are grown in a similar fashion on both substrates, as also concluded in [113]. The relatively strong adhesion of the lipid membrane to graphene may be explained by either the formation of lipid monolayer (namely, the hydrophobic end faces the graphene) or adhesion of lipid bilayers to graphene defects, similarly to the functionalization process of carbon nanotubes [119]. Excess protein is washed away and therefore, the protein forms a monolayer on top of the lipid membrane. Such conclusion is corroborated by the unbound experiments described earlier and reference experiments on unbounded streptavidin [120]. A typical number of defects in graphene is $\sim 10^{10}$ defects per cm^2. This number is much smaller than close packed assembly of cylindrical lipid molecules on 1 cm^2 area (on the order of 10^{14} per lipid layer). The number of imbedded receptors within the lipid membrane is a factor of ten smaller than the number of lipid molecules. This means that the maximum number of active receptors imbedded in

a close packed lipid monolayer is smaller than $10^{13}/cm^2$ whereas the minimum number is $10^9/cm^2$. Geometrical considerations for protein binding will lower these limits even further. Nevertheless, since the binding of the lipid membrane is strong enough to withstand repeated washing and likewise, films of bound protein ligand complexes, the upper (worst case scenario) limit to the protein concentration as ~0.01 μM. As a note, our initial stock solution for the protein concentration was a factor of 100 larger.

In conclusion, selective binding between the hemagglutinin area of influenza viruses and their respective receptors was monitored. Such extremely thin-film methodology could be employed in detailing the characteristics of hydrogen bonds involved and in developing a database of unique signatures of known strains, therefore, facilitating global surveillance of the viruses.

5.2.5   Graphene - Coated Anodized Aluminum Oxide (AAO): Potential Aspirant for Bio-Detection

It has been demonstrated that array of nano-holes, with pitch much smaller than the propagating wavelength, enables the amplification of both Raman and fluorescence signals. To further investigate this phenomenon the Raman scattering of graphene deposited nano-hole arrays were measured. As the sample was azimuthally rotated, a periodicity of 7.5 and 5 degrees were revealed for the 2700 cm^{-1} and 1600 cm^{-1} Raman lines of graphene, respectively. This is contrary to the scattered laser line azimuthal symmetry of 30 degrees for the hole-array alone. When stilbene was deposited on the graphenated platforms, its Raman peak shifted as a function of incident angle; this was contrary to the unshifted 1600 cm^{-1} peak of graphene itself. The data suggest strong

coupling between the Raman spectra and surface plasmon polariton waves, which propagate along the graphene surface. Such graphenated substrates may open the door to a new class of signal enhancing platforms for bio-chemical applications.

All the experiments were carried out using an Ar ion laser at 514.5 nm wavelength with intensity of 20 mW. The signal was assessed by use of a 75 cm single chamber spectrometer equipped with a cooled CCD camera at -15°C. Figure 5.41(a) shows the experimental configuration. The sample was positioned in a confocal configuration, tilted and rotated as necessary with respect to the incident linearly polarized beam.

Raman signal [Figure 5.41(b)-(d)] was used to determine the number of deposited graphene layers [76]. In this spectral region, a monolayer of graphene exhibits a single peak; two-layer graphene exhibits two close D' Raman lines. The two inmost peak positions for a double layered graphene are ~2683 cm^{-1} and ~2702 cm^{-1} respectively. These two peaks are typically un-resolvable when the two-layer graphene is deposited on a silicon substrate [122]. In contrast, they are clearly visible for the graphene/AAO structure [Figure 5.41(c)]. In Figure 5.41(d), the Raman spectrum for a three layer graphene has been shown. Two peaks, at ~2677 ± 2 cm^{-1} and ~2716 ± 2 cm^{-1} respectively, are expected [76]. Figure 3.6(b) and Reference 82 suggests that the strongest electric field occurs within the holes, at the air/oxide interface level. Therefore, the coupling between the electric field components and the film under test are strongest when the film or molecules are residing on top of the aluminum oxide layer. *Such considerations emphasize the role of graphene as a 'molecular support' just above the hole.*
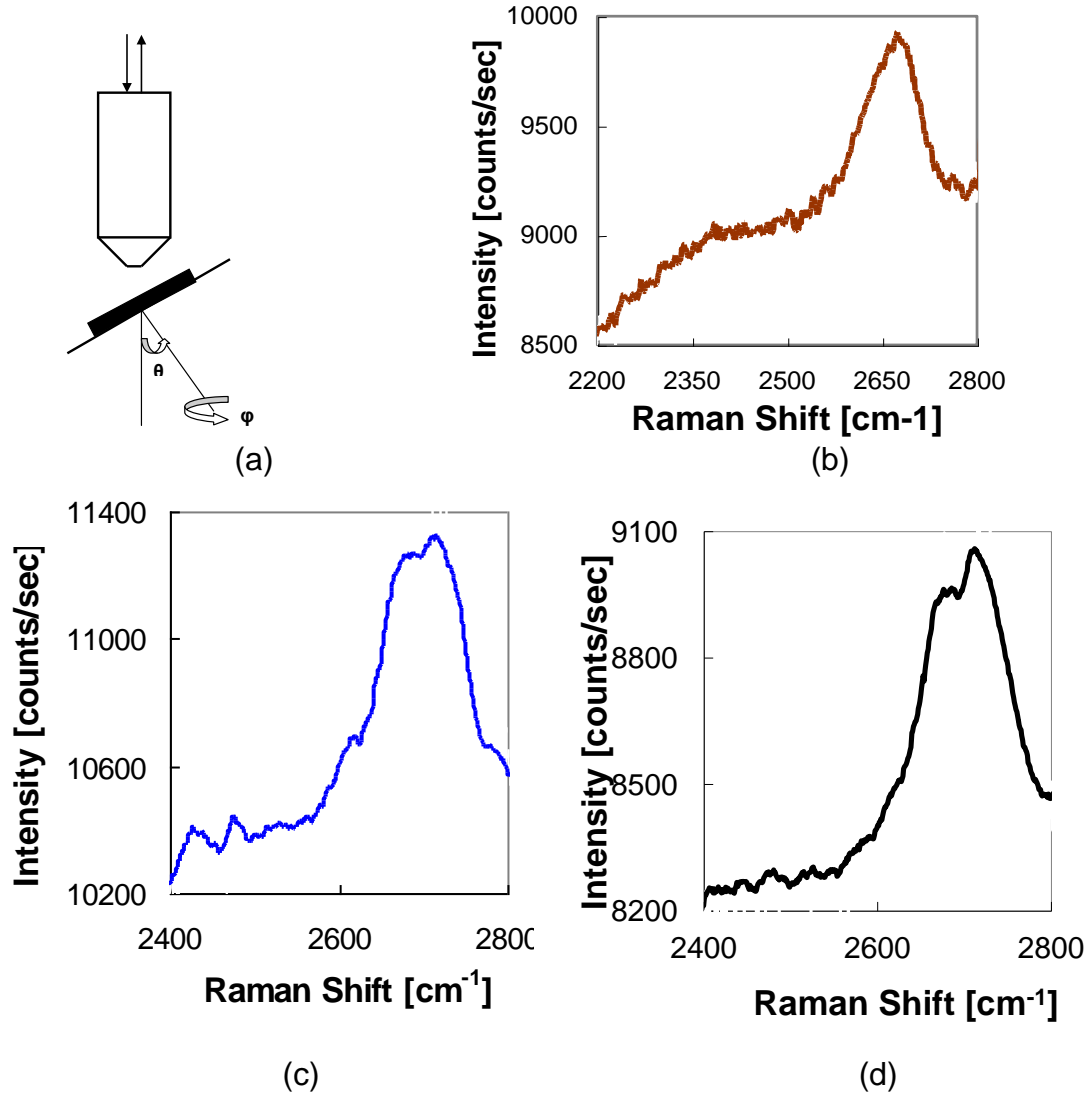
Figure 5.41 (a) Experimental configuration. (b) (c) and (d) Raman spectra of a monolayer, two-layer and three-layer graphene on AAO substrate; peak splitting for two and three-layers graphene is clearly visible.

Figure 5.42(a) shows the Rayleigh scattered laser line at 514.5 nm as a function of azimuthally rotating angle when the AAO sample is tilted at $\theta=0^o$ (normal incidence). The experiment was repeated for a tilt angle of $\theta=8^o$ – the angle for which the laser line is coupled to a Surface Plasmon (SP) mode. As may be expected for resonance conditions (standing wave) there appears a period doubling [123], hence, the symmetry of 30

degrees instead of the expected 60 degrees. The latter is due to the hexagonal close packing of the hole-array.

(a)   (b)
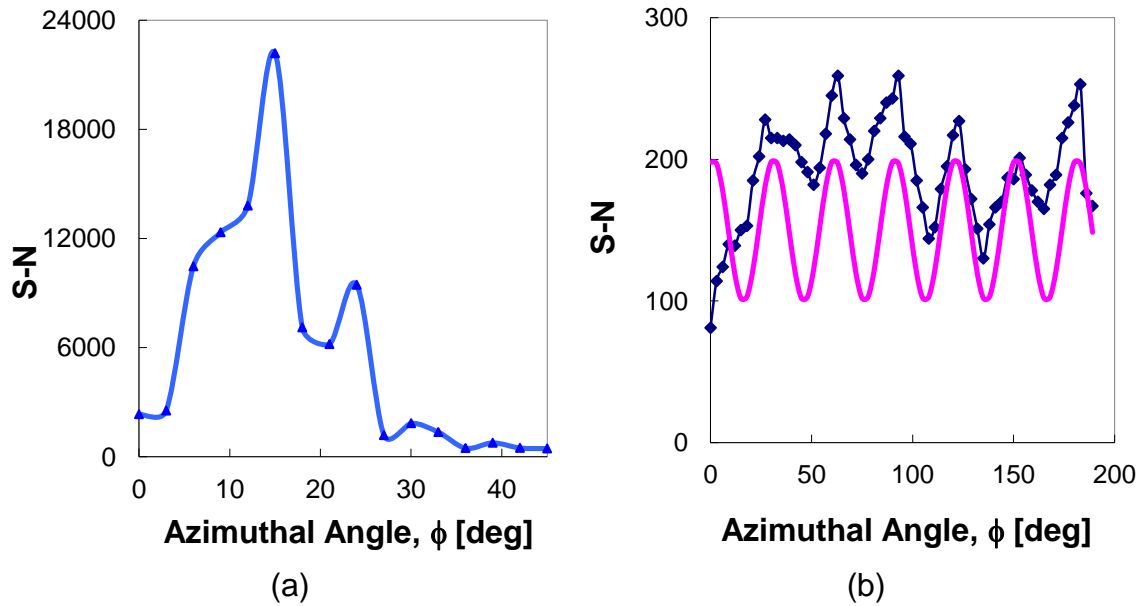
Figure 5.42 (a) Laser line scatterings (the 514.5 nm peak minus the noise floor) from an AAO substrate at tilt angle $\theta=0^o$ with occasional signal variations. (b) Laser line scatterings (the 514.5 nm peak minus the noise floor) from an AAO substrate at tilt angle $\theta=8^o$. The shifted sinusoidal curve, $A+Bsin^2(6\phi+\phi_0)$ accentuates the 30 degree symmetry.

Figure 5.43 shows the Raman D' line (~2700 cm^{-1}) for graphenated AAO as a function of azimuthal (in-plane rotations) angle, φ at normal incidence ($\theta=0^o$). The experiment was repeated for substrates tilted at $\theta=8^o$ – the angle for which surface plasmons mode for the pump wavelength is launched. The scattered wavelength was measure in parallel (blue curve) and in perpendicular (red curve) to the input polarization state. A periodicity of 7-8° in the signal (minus noise floor) with a hyperfine structure at approximately 3-4 degrees is clearly observed for a tilt angle of $\theta=8^o$ [Figure 5.43(b)].
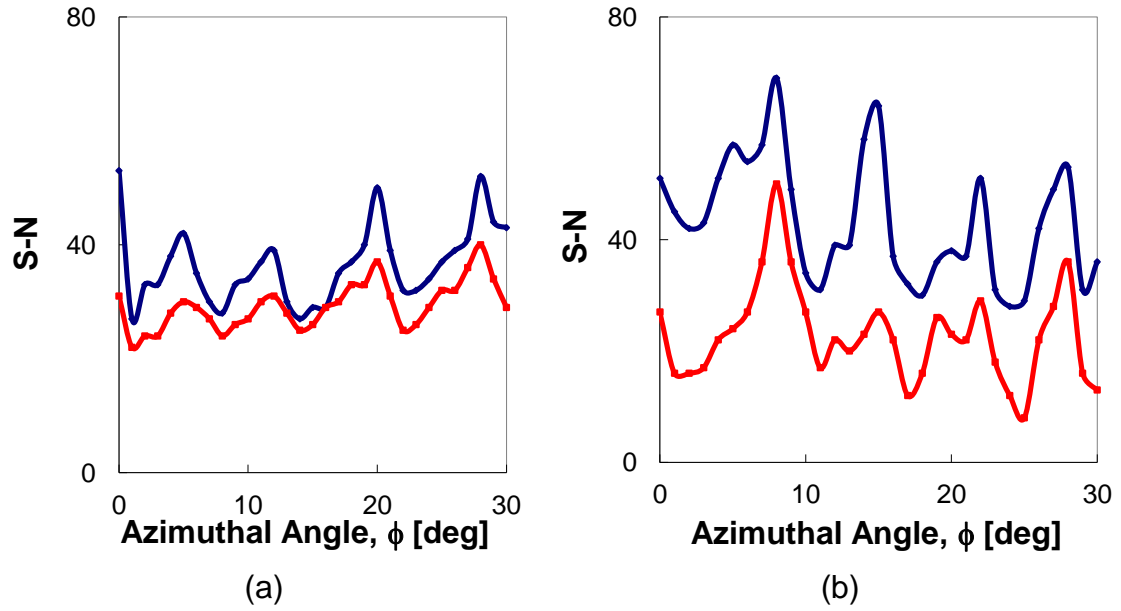
Figure 5.43 (a) D' Raman line (the ~2700 cm^{-1} peak minus the noise floor) of graphenated AAO as a function of azimuthal (in-plane rotation) angle at tilt angles of θ=0 and (b) θ=8 degrees. The blue (upper curve is for polarization state parallel to the polarization state of the incident beam. The red (lower) curve) is for polarization state perpendicular to that of the incident beam.

In Figure 5.44, Raman G-line (~1600 cm^{-1}) has been presented for graphenated AAO as a function of azimuthal angle. Here too, clear signal oscillations have been observed with periods of 5 and 3 degrees. Both effects may be explained by a generalized momentum conservation which involves phonons in addition to the various crystallographic planes of the substrate. As exemplified by Figure 4.5(c), the coupling between the marked holes exhibits azimuthal rotation symmetry of 7.5 degrees.

(a)   (b)
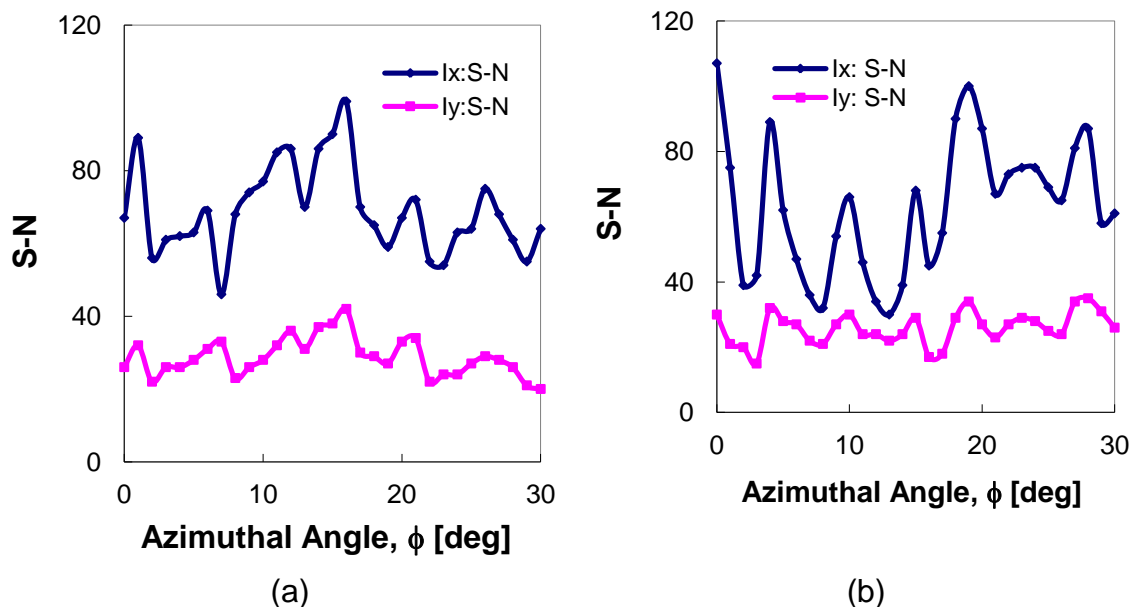
Figure 5.44 (a) G-Raman line (the 1600 cm^{-1} peak minus the noise floor) of graphenated AAO as a function of azimuthal (in-plane rotation) angle at tilt angles of $\theta=0$ and (b) $\theta=8$ degrees. The blue (upper curve is for polarization state parallel to the polarization state of the incident beam. The pink (lower) curve) is for polarization state perpendicular to that of the incident beam.

Such considerations ought to affect molecules placed on top of graphenated AAO substrates. To check that, stilbene has been used as a test molecule. Normalized data of as-is spectra are presented in Figure 5.45. In contrast to large molecules placed on AAO [73], the signal was not substantially enhanced here in comparison to the signal of stilbene on a glass substrate. This raises an old issue of deducing SERS amplification factor upon comparing differently prepared samples and the impact of local molecular concentration on that value. It was observed that at least for tilted experiments, the molecular concentration remains constant.
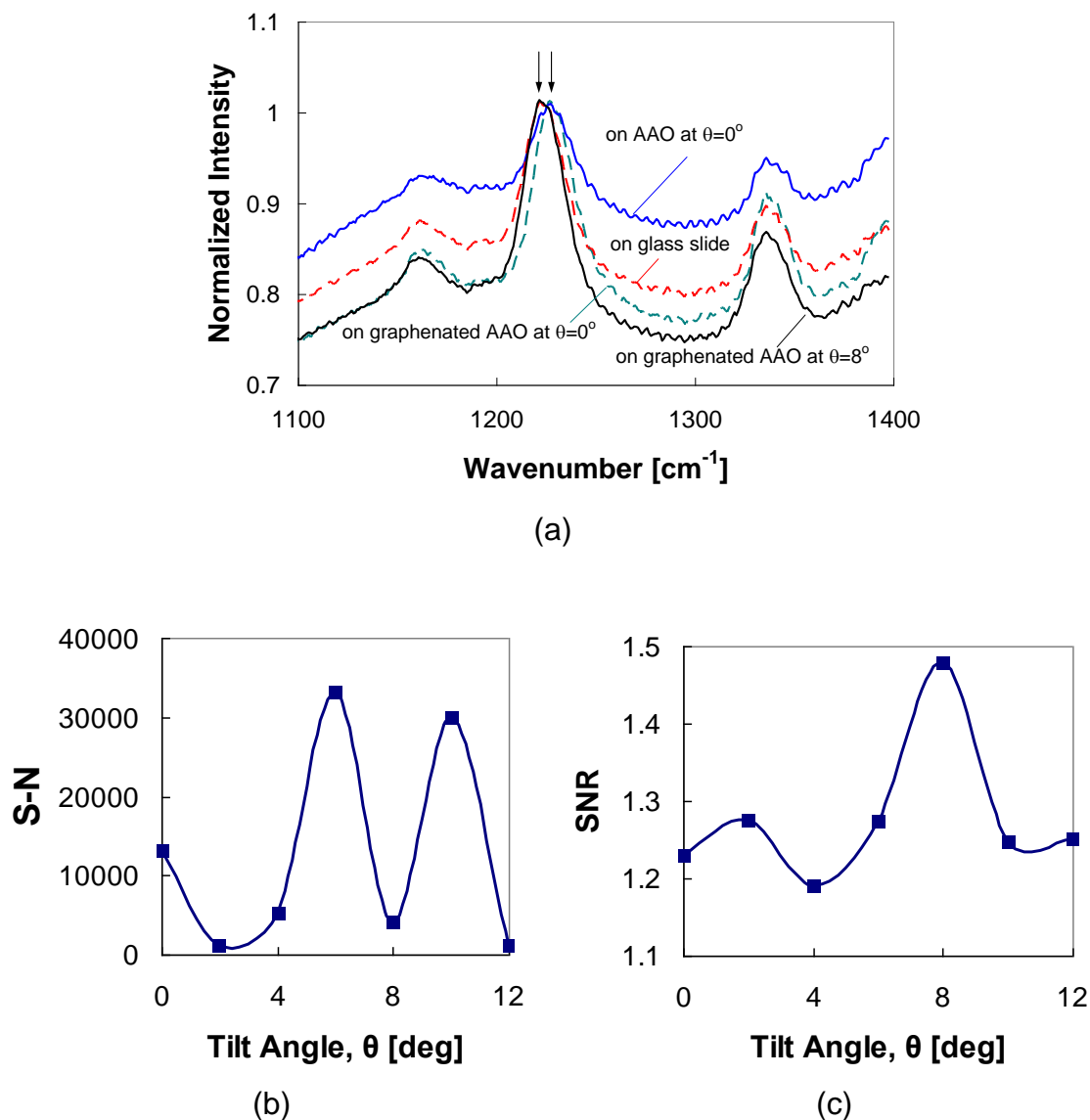
Figure 5.45 (a) Normalized Raman spectra of stilbene on various substrates. Note the peak shift for out of resonance cases (un-tilted AAO substrates). Note also the improved signal-to-background ratio for the graphenated AAO samples, tilted at 8 degrees. (b) Signal minus the noise and (c) Signal-to-noise ratio of the 1230 cm^{-1} line of stilbene.

A peak shift at off-resonance conditions is clear from Figure 5.45. The 5 cm^{-1} shift is also associated with spectral line broadening and may be related to shear stress since the relative peak frequency has increased. When placed on AAO *without graphene*, stilbene exhibited an angular *independent* peak shift as alluded to by Figure 5.45(a) and

which is attributed to stress. The small shift varied from sample to sample but nonetheless remained independent of the tilt angle. By comparison, the 1600 cm^{-1} line of graphene did not shift when placed on AAO, regardless of the incident angle used. The intensity of both peaks exhibited variations similarly to Figure 5.45(c).

Figure 5.45 also present data for stilbene placed on garphenated AAO substrates. The data has been shown using two methods: either taking the signal minus the noise floor [Figure 5.45(b)], or, dividing the peak value by the noise floor (Figure 5.45(c)). The period of signal oscillation is the same yet, complementing one another. The normalized data [Figure 5.45(a)] implies that the minimum spectral line width occurs at the minima of Figure 5.45(b) and for the maxima of Figure 5.45(c).

A model was proposed in which SERS was attributed to magnetic field effect [124]. Such magnetic effect in AAO is enabled by closure of magnetic loops, which effectively occurs only for large molecules covering several holes. This is the case for macromolecules, spores or, carbon nanotubes on AAO. It was found that small molecules will portray SERS in such substrates to a much lesser extent [89]. The angular *independent* Raman peak shift for stilbene on AAO alone is attributed to molecule stress, whereas the angular *dependent* Raman shift for stilbene on graphenated AAO is attributed to coupling to propagating phonons. The 'true' Raman peak position will appear when resonating conditions are met at either the minima of Figure 5.44(b) or alternatively at the maxima of Figure 5.45(c).

In conclusion, Raman scatterings from graphene overlayed on an array of nano-holes have been studied. In-plane rotation cycles signify the effect of coherent scattering from symmetry hole-planes, and allude to strong coupling between SPP and vibrating

molecules on the substrates surface. Such substrates may be useful for optically analyzing bio-chemistry at well-organized 'hot spots' on graphene-coated porous substrates.

CHAPTER 6

CONCLUSIONS

Graphene - monolayer, or a few layers of graphite - has attracted vast interest recently owing to its two-dimensional crystallographic nature and its potential use in a new generation of microelectronic devices. A new technique to lay out graphene has been developed and demonstrated here. By using this method, stress-free graphene films on solid and perforated substrates were obtained, with coverage of hundreds of microns squared. Various graphene based devices, such as field effect transistors, ionic screening electrodes, surface plasmon lasers, and bio-molecules sensors which are based on surface plasmons has been demonstrated and assessed.

The ability to control the ionic current in electrochemical cells by additional, yet smaller electronic source is very appealing. Such constructions may enable studies of ion tunneling and electronically controlled graphene-coated bio-membranes.

Model bio-systems, for example- conjugated streptavidin bound to biotinylated lipid bilayer, have been characterized by using graphene based bio-sensors. The samples exhibits enhanced IR and Raman characteristics. The enhancement was attributed to the properties of the related surface charge waves. Understanding this phenomenon may lead to the design of spectral platforms to detect bio-chemical reactions. The extremely thin-film methodology used could be employed in detailing characteristics of hydrogen bonds involved and in developing a database of unique signatures of known virus strains.

CHAPTER 7

FUTURE WORKS

Bacterial infections are the fifth cause of mortality in the US, and their economic impact on the industrial, agricultural, and healthcare sector is significant. Headlines in the press about the presence of enterrohemorrhagic *E. coli* in tainted produce, the identification of the extremely cytotoxic Subtilase AB5 toxin in *E. coli*, the aftermath of the *B. anthracis* attacks in 2001, and the recent identification of drug resistant *Mycobacterium tuberculosis* [XDR-TB] in Africa sparked public concern. Therefore, the need for developing fast, sensitive, and reliable detection methods for bacteria in food, the environment, and clinical samples is crucial to safeguard public health.

Traditionally, the presence of a bacterium is detected microscopically, usually after growth in culture. Confirmation is based on growth patterns in various media and biochemical tests. These methods, although highly specific, have some drawbacks. These methods require incubation time of more than 24 hours; lack sensitivity besides the fact that not all microorganisms may be amplified in a culture. More recently, other methods involving polymerase chain reaction (PCR) and fluorescent immunoassays have been developed. However, despite their enhanced sensitivity and specificity, these methods are costly, time-consuming, and require trained and experienced personnel.

Nanotechnology offers an attractive alternative to the identification of molecular targets in vitro and in vivo, requiring smaller sample concentration and shorter preparation time. It is known that fluorescence-based detection method is sensitive, selective, rapid, and cost-effective in the analysis of biomolecules. This may be achieved

 by using graphene oxide (GO) based platforms. One of the ideas takes the advantage of GO's fluorescence quenching, which is due to the fluorescence resonance energy transfer. A graphene-based DNA and protein sensing platform may be introduced by using GO coated anodized aluminum oxide. The strategy will be to put dye-labeled DNA on the platforms. When irradiated by the laser beam, the fluorescence of these dye-labeled DNA will quench. During the detection process, a target molecule (i.e., the complementary ssDNA), will hybridize with the dye-labeled DNA to form dsDNA, and the dye leaves from the GO surface leading to restoration of the dye's fluorescence. This way, prepared platform may be used to detect HIV-1 target DNA and human thrombin, resulting in good selectivity and sensitivity of the detection.

Using a different approach, GO could be complexed with a water-soluble and positively charged dye, through ion exchange. The fluorescence of the dye will quench upon the formation of dye-GO complex. The quenched fluorescence will be turned on, if the dye can interact with an analyte more strongly than does with GO. DNA can be able to complex with the dyeto switch on the fluorescence. Similarly, detection of RNA, glucose, and proteins, can be viable in the same approach.

Another strategy for graphene-based fluorescence sensing is based on the photoluminescent property of GO itself. GO exhibits the near-UV to blue fluorescence, which originates from the recombination of electron–hole pairs, localized within the small sp^2 carbon domains embedded in the carbon–oxygen sp^3 matrix. Following the fabrication of GO sheets on AAO, antibodies of the target may be immobilized them. At the same time, an antibody complex may be synthesized in a solution, such that it selectively binds to the target DNA molecule. Once the binding event takes place,

fluorescence resonance energy transfer between the antibody complex and GO occurs, and the reduction in GO fluorescence may be detected. This selective and sensitive platform may be expanded further to a GO microarray format for the multiple pathogen analysis.

REFERENCES

[1]   A. H. Castro Neto, F. Guinea, N. M. R. Peres, K. S. Novoselov and A. K. Geim, "The Electronic Properties of Graphene", *Rev. of Mod. Phys.*, vol. 81, no. 1, pp. 109-162, 2009.

[2]   A. N. Sidorov, M. M. Yazdanpanah, R. Jalilian, P. J. Ouseph, R. W. Cohn and G. U. Sumanasekera, "Electrostatic deposition of graphene", *Nanotech.,* vol. 18, no. 13, pp. 135301-135307, 2007.

[3]   A. C. Ferrari, J. C. Meyer, V. Scardaci, M. Lazzeri, F. Mauri, S. Piscance, D. Jiang, K. S. Novoselov, S. Roth and A. K. Geim, "Raman spectrum of graphene and graphene layers", *Phys. Rev. Lett*, vol. 97, no. 18, pp. 187401-4, 2006.

[4]   Y. Zhang, J. P. Small, M. E. S. Amori and P. Kim, "Electric field modulation of galvanomagnetic properties of mesoscopic graphite" *Phys. Rev. Lett.,* vol. 94, no. 17, pp. 176803-176807, 2005.

[5]   K. S. Novoselov, A. K. Geim, S. V. Morozov, D. Jiang, Y. Zhang, S. V. Dubonos, I. V. Grigorieva and A. A. Firsov, "Electric field effect in atomically thin carbon films" *Science*, vol. 306, no. 5696, pp. 666-669, 2004.

[6]   P. R. Wallace, "The band theory of graphene", *Phys. Rev*, vol.71, no. 9, pp. 622-634, 1947.

[7]   K. S. Novoselov, A. K. Geim, S. V. Morozov, D. Jiang, M. I. Katsnelson, I. V. Grigorieva, S. V. Dubonos and A. A. Firsov, "Two-dimensional gas of massless dirac fermions in graphene", *Nature*, vol. 438, pp. 197-200, 2005.

[8]   Y. Zhang, Y-W Tan, H. L. Stormer and P. Kim, "Experimental observation of the quantum Hall effect and Berry's phase in graphene", *Nature*, vol. 438, pp. 201-204, 2005.

[9]   X. K. Lu, M. F. Yu, H. Huang and R. S. Ruoff, "Tailoring Graphite with the Goal of Achieving Single Sheets" *Nanotech.*, vol. 10, no. 3, pp. 269-272, 1999.

[10] K. I. Bolotin, K. J. Sikes, J. Hone, H. L. Stormer, P. Kim, "Temperature Dependent Transport in Suspended Graphene" *Phys. Rev. Lett.*, vol. 101, no. 9, pp. 096802-096806, 2008.

[11] K. S. Novoselov, A. K. Geim, S. V. Morozov, D. Jiang, Y. Zhang, S. V. Dubonos, I. V. Grigorieva and A. A. Firsov, "Electrical field effect n atomically thin carbon films", *Science*, vol. 306, no. 5696, pp. 666- 669, 2004.

[12] K. S. Novoselov, E. McCann, S. V. Morozov, V. I. Fal'ko, M. I. Katsnelson, U. Zeitler, D. Jiang, F. Schedin and A. K. Geim, "Unconventional Quantum Hall Effect and Berry's Phase of 2n in Bilayer Graphene" *.Nat. Phys.*, vol. *2*, 177-180, 2006.

[13] Z. Jiang, Y. Zhang, Y. W. Tan, H. L. Stormer and P. Kim, "Quantum Hall Effect in Graphene" *Sol. St. Commun.*, vol. 143, no. 1-2, pp. 14-19, 2007.

[14] Z. Jiang, Y. Zhang, H. L. Stormer, and P. Kim, "Quantum Hall States near the Charge Neutral Dirac Point in Graphene", *Phys. Rev. Lett.*, vol. 99, no. 10, pp. 106802-4, 2007.

[15] Y. B. Zhang, Y. W Tan, H. L. Stormer, and P. Kim, "Experimental observation of the quantum Hall effect and Berry's phase in graphene", *Nature, vol. 438*, pp. 201-207, 2005.

[16] K. S. Novoselov, Z. Jiang, Y. Zhang, S. V Morozov, H. L. Stormer, U. Zeitler, J. C. Maan, G. S. Boebinger, P. Kim, P and A. K. Geim, "Room-Temperature Quantum Hal l Effect in Graphene", *Science*, vol. 315, no. 5817, pp. 1379-1382, 2007.

[17] B. Ozyilmaz, P. Jarillo-Herrero, D. Efetov, D. A. Abanin, L. S. Levitov and P. Kim, "Electronic Transport and Quantum Hall Effect in Bipolar Graphene p-n-p Junctions". *Phys. Re*V. *Lett.*, vol 99, no. 16, pp. 166804-166808, 2007.

[18] K. S. Novoselov, A. K. Geim, S. V. Morozov, D. Jiang, M. I. Katsnelson, I. V. Grigorieva, S. V. Dubonos, and A. A. Firsov, "Two-Dimensioanl Gas of Massless Dirac Fermions in Graphene", *Nature*, vol. *438*, pp. 197-200, 2005.

[19] V. Morozov, K. S. Novoselov, M. I. Katsnelson, F. Schedin, D. C. Elias, J. Jaszczak, A. K. Geim, "Giant Intrinsic Carrier Mobilities in Graphene and Its Bilayer *Phys. Re*v. *Lett.,* vol. 100, no. 1, pp. 016602- 016606, 2008.

[20] M. Han, B. Ozyilmaz, Y. Zhang, P. Jarillo-Herero and P. Kim, " Electronic Transport Measurement in Graphene Nanoribbons", *Phys.Status Solidi B: Bas. Sol. State Phys.*vol. 244, no. 11, pp. 4134-4137, 2007.

[21] F. Schedin, A. K. Geim, S. V. Morozov, E. W. Hill, P. Blake, M. I. Katsnelson and K. S. Novoselov, "Detection of Individual Gas Molecules adsorbed on Graphene", *Nat. Mater.*, vol. 6, pp. 652-655, 2007.

[22] K. Novoselov and A. Geim, "Graphene detects single molecule of toxic gas", *Mater. Technol.,* vol. 22, pp. 178–179, 2007.

[23] J. C. Meyer, A. K. Geim, M. I. Katsnelson, K. S. Novoselov, T. J. Booth, and S. Roth, "The Structure of Suspended Graphene Sheets", *Nature*, vol.446, no. 7131, pp. 60-63, 2007.

[24] M. Ishigami, J. H. Chen, W. G. Cullen, M. S. Fuhrer, and E. D. Williams, " Atomic Structure of Graphene on SiO_2", *Nano Lett.*, vol. 7, no. 6, pp. 1643-1648, 2007.

[25] J. H. Chen, C. Jang, S. Xiao, M. Ishigami and M. S. Fuhrer, " Intrinsic and extrinsic performance limits of graphene devices on SiO_2", *Nat. Nanotech.*, vol. 3, no. 4, pp. 206-209, 2008.

[26] A. K. Geim and K. S. Novoselov, "The rise of graphene", *Nat. Mat.*, vol. 6, no. 3, pp. 183-191, 2007.

[27] R. S. Shishir and D. K. Ferry, "Intrinsic mobility in graphene", *J. Phys.: Cond.. Matter*, vol. 21, no. 23, pp. 232204- 232208, 2009.

[28] F. Chen, J. Xia, D. K. Ferry and N. Tao, " Dielectric screening enhanced performance in graphene FET", *Nano Lett*., vol. 9, no. 7, pp. 2571- 2574, 2009.

[29] S. Adam, E. H. Hwang, V. M. Galitski and S. Das Sarma, " A self-consistent theory for graphene transport", *PNAS*, vol. 104, no. 47, pp. 18392-18397, 2007.

[30] I. W. Frank, D. M. Tanenbaum, A. M. van der Zande and P. L. McEuen, "Mechanical properties of suspended graphene sheets", *J. Vac. Sci. Technol. B*, vol. 25, no. 6, pp.2558-2561, 2007.

[31] C. Lee, X. Wei, J. W. Kysarand . Hone, "Measurement of te elastic properties and intrinsic strength of monolayer graphene", *Nature*, vol. 321, no. 5887, pp. 385-388, 2008.

[32] M. Kohlschütter and P. Haenni, "Zur Kenntnis des Graphitischen Kohlenstoffs und der Graphitsäure", *Z. Anorg. Allg. Chem,* vol. 105, no. 1, pp. 121–144, 1918.

[33] A.B. Kuzmenko, E. van Heumen, F. Carbone and D. van der Marel, "Universal optical conductance of graphite", Z. *Anorg. Allg. Chem.*, vol. 100, no. 11, pp. 117401-1-117401-4, 2008.

[34] R. R. Nair, P. Blake, A. N. Grigorrenk, K. S. Novoselov, T. J. Booth, T. Stauber, N. M. R. Peres and A. K. Geim, "Universal dynamic conductivity and quantized visible opacity of suspended graphene", *Nature*, vol. 320, no. 5881, pp. 3-7, 2008.

[35] I. Forbeaux, J. M. Themlin, A. Charrier, F. Thibaudau and J. M. Debever, "Solid-state graphitization mechanisms of silicon carbide 6h-SiC polar faces", *Appl. Surf. Science*, vol. 162, pp. 133-142, 2000.

[36] C. Berger, Z. M. Song, X. B. Li, X. S. Wu, N. Brown, C. Naud, D. Mayo, T. B. Li, J. Hass, A. N. Marchenkov, E. H. Conrad, P. N. First and W. A. de Heer, "Electronic confinement and coherence in patterned epitaxial graphene", *Science*, vol. 312, no. 5777, pp. 1191-1196, 2006.

[37] C. Berger, Z. M. Song, X. B. Li, X. S. Wu, N. Brown, C. Naud, D. Mayo, T. B. Li, J. Hass, A. N. Marchenkov, E. H. Conrad, P. N. First, and W. A. de Heer, "Electronic Confinement and Coherence in Patterned Epitaxial Graphene", *Science*, vol. no. 5777, 312, pp. 1191- 1196, 2006.

[38] W. A. de Heer, C. Berger, X. S. Xu, P. N. First, E. H. Conrad, X. B. Li, T. B. Li, M. Sprinkle, J. Hass, M. L. Sadowski, M. Potemski and G. Martinez, "Epitaxial Graphene", *Sol. St. Comm.*, vol. 143, no. 1-2, pp. 92- 100, 2007.

[39] J. Hass, W. A. de Heer and E. H. Conrad, "The Growth and Morphology of Epitaxial Multilayer Graphene", *J. Phys.: Condens. Matter*, vol. 20, no. 32, pp. 323202-323207, 2008.

[40] K. S. Kim, Y. Zhao, H. Jang, S. Y. Lee, J. M. Kim, K. S. Kim, J. H. Ahn, P. Kim, J. Y. Chai and B. H. Hong, " Large-scale Pattern Growth of Graphene Films for Stretchable Transparent Electrodes", *Nature*, vol. 457, pp. 706-710, 2009.

[41] X. Li, W. Cai, J. An, S. Kim, J. Nah, D. Yang, R. Piner, A. Velamakanni, I. Jung, E. Tutuc, S. K. Banerjee, L. Colombo and R. Ruoff, " Large-area Synthesis of High-Quality and Uniform Graphene Films on Copper Foils", *Science*, vol. 324, pp.1312-1314, 2009.

[42] G. Eda, F. Giovanni and M. Chhowala, " Large-area Ultrathin Films of Reduced Graphene Oxide as a Transparent and Flexible Electronic Material", *Nat. Nanotech.*, vol. 3, pp. 270-274, 2008.

[43] X. Li, G. Zhang, X. Bai, X. Sun, X. Wang, E. Wang and H. Dai, "Highly conducting Graphene Sheets and Langmuir-Blodgett Films", *Nat. Nanotech.*, vol. 3, pp. 538-542, 2008.

[44] Y. Lee and J. Lee, "Scalable growth of free-standing graphene wafers with copper(Cu) catalyst on SiO2/Si substrate: Thermal conductivity of the wafers", *Appl. Phys. Lett*., vol. 96, pp. 083101- 083104, 2010.

[45] Y. Lee, S. Bae, H. Jang, S. Jang, S. Zhu, S. H. Sim, Y. Song, B. H. Hong and J. Ahn, "Wafer-Scale Synthesis and Transfer of Graphene Films", *Nano Lett.*, 2010, vol. 10, no. 2, pp 490–493, 2010.

[46] K. S. Kim, Y. Zhao, H. Jang, S. Y. Lee, J. M. Kim, K. S. Kim, J. Ahn, P. Kim, J. Choi and B. Hee Hong, "Large-scale pattern growth of graphene films for stretchable transparent electrodes", *Nature*, vol. 457, pp. 706-710, 2009.

[47] Q. Yu, J. Lian, S. Siriponglert, H. Li, Y. P. Chen and S. Pei, "Graphene segregated on Ni surfaces and transferred to insulators", *Appl. Phys. Lett.,* vol. 93, pp. 113103-113106, 2008.

[48] J. Hass, C. A. Jeffrey, R. Feng, T. Li, X. Li, Z. Song, C. Berger, W. A. de Heer, P. N. First and E. H. Conrad, "Highly-ordered graphene for two dimensional electronics", *Appl. Phys. Lett.*, vol. 89, no.14, pp. 143106-143109, 2006.

[49] R. Sordan, F. Traversi and V. Russo, "Logic gates with a single graphene transistor". *Appl. Phys. Lett.* vol. 94, no. 7, pp. 073305-073308, 2009.

[50] H. Wang, D. Nezich, J. Kong and T Palacios, "Graphene Frequency Multipliers". *IEEE Electr. Device. L.* vol. 30, no. 5, pp. 547-549. 2009.

[51] Y. M. Lin, C. Dimitrakopoulos, K. A. Jenkins, D. B. Farmer, H. Y. Chiu, A. Grill, and P. Avouris, "100-GHz Transistors from Wafer-Scale Epitaxial Graphene". *Science*, vol. 327, no. 5966, pp. 662-662, 2010.

[52] Y. Wang, X. Chen, Y. Zhong, F. Zhu and K. P. Loh, "Large area, continuous, few-layered graphene as anodes in organic photovoltaic devices'. *Appl. Phys. Lett.,* vol. 95, no. 6, pp. 063302-063305, 2009.

[53] M. Fujita, K. Wakabayashi, K. Nakada and K. Kusakabe, "Peculiar Localized State at Zigzag Graphite Edge" *J. Phys. Soc. Jpn.* vol. 65, no. 7, pp. 1920-192, 1996.

[54] V. Barone, O. Hod, and G. E. Scuseria, "Electronic Structure and Stability of Semiconducting Graphene Nanoribbons" *Nano Lett.* vol. 6, no.12, pp. 2748- 2754, 2006.

[55] M. Y. Han, B. Özyilmaz, Y. Zhang, and P. Kim, "Energy Band-Gap Engineering of Graphene Nanoribbons" *Phys. Rev. Lett.* vol. 98, no. 20, pp. 206805-206809, 2007.

[56] M. D. Stoller, S. Park, Y. Zhu, J. An and R. Ruoff, "Graphene-Based Ultracapacitors", *Nano Lett.*, vol. 8, no. 10, pp. 3498- 3502, 2008.

[57] A.G. Pandolfo and A. F. Hollenkamp, "Carbon properties and their role in supercapacitors", *J. Power Sour.,* vol. 157, pp. 11–27, 2006.

[58] S. Stankovich, D. A. Dikin, G. H. B. Dommett, K. M. Kohlhaas, E. J. Zimney, E. A. Stach, R. D. Piner, S. T. Nguyen, R. S. Ruoff, "Graphene-based composite materials", *Nature*, vol.442, pp. 282–286, 2006.

[59] A. K. Geim and P. Kim, "Carbon wonderland", *Sci. Am.,* vol. 298, pp. 90– 97, 2008.

[60] N. Mohanty and V. Berry, "Graphene-Based Single-Bacterium Resolution Biodevice and DNA Transistor: Interfacing Graphene Derivatives with Nanoscale and Microscale Biocomponents", *Nano Lett*., vol. 8, no. 12, pp. 4469-4476, 2008.

[61] F. Schedin, A. K. Geim, S. V. Morozov, E. W. Hill, P. Blake, M. I. Katsnelson and K.S. Novoselov, " Detection of Individual Gas Molecules Adsorbed on Graphene", *Nat. Mater*., vol. 6, pp. 652-655, 2007.

[62] G. Ko, H. Y. Kim, J. Ahn, Y. M. Park, K. Y. Lee and J. Kim, "Graphene-based Nitrogen Dioxide Gas Sensors", *Curr. Appl. Phys.*, vol. 10, no. 4, pp. 1002-1004, 2010.

[63] H. Masuda and K. Fukuda, " Ordered Metal Nanohole Arrays Made by a Two-Step Replication f Honeycomb structures of Anodic alumina", *Science*, vol. 268, no. 5216, pp. 1466-1468, 1995.

[64] J.W. Diggle, T.C. Downie and C.W. Goulding, "anodic Oxide Films on Aluminum", *Chem. Rev.*, vol. 69, no. 3, pp. 365- 405, 1969.

[65] J. Goldstein, D. E. Newbury, D, C. Joy, C. E. Lyman, P. Echlin, E. Lifshin, L. Sawyer and J. R. Michael, "Scanning electron microscopy and x-ray microanalysis", 3rd edition, Kluwer Adacemic/ Plenum Publishers, pp. 689, 2003.

[66] D. E. Grupp, H. J. Lezec, T. W. Ebbesen, K. M. Pellerin and T. Thio, "Crucial role of metal surface in enhanced transmission through subwavelength apertures", *Appl. Phys. Lett*., vol. 77, pp. 1569, 2000.

[67] B. J. Munk, *Frequency Selective Surfaces* (Wiley, New York, 2000).

[68] M. Rebbert, P. Isaacson, J. Fischer, M. A. Greenhouse, J. Grossman, M. Peckerar, and H. A. Smith, *Appl. Opt*., vol. 33, pp. 1286- 1289, 1994.

[69] G. M. Ressler and K. D. Möller, " Far Infrared Bandpass Filters and Measurements of Resiprocal Grid", *Appl. Opt*., vol. 6, no. 5, pp. 893-896, 1967.

[70] O. Steernberg, K.P. Stewart, Y. Hor, A. Bandyopadhyay, J.F. federici, M. Bornefeld, Y.-L. Mathis, D. Sliwinski, K.D. Moeller and H. Grebel, "Square-shaped metal screens in the infrared to terahertz spectral region: Resonance frequency, band gap, and bandpass filter characteristics", *J. Appl. Phys*., vol. 104, pp. 023103-1, 2008.

[71] R. Ulrich, K. F. Renk, and L. Genzel, **"**Tunable Submillimeter Interferometers of the Fabry-Perot Type", *IEEE Trans. Microwave Theory. Tech*. vol.11, pp.363, 1963.

[72] S. Ramo, *Fields and Waves in Communication Electronics*. New York: Wiley, 1984, vol. 2.

[73] C. Zhang, A. Smirnov, D. Hahn and H. Grebel, "Surface enhanced Raman scattering of biospecies on anodized aluminum oxide films", *Chem. Phys. Lett.,* vol. 440, pp. 239– 243, 2007.

[74] R. Li, A. Banerjee and H. Grebel, "The possibility for surface plasmon lasers", *Opt. Express*, vol. 17, pp. 1622–1627, 2009.

[75] A. Banerjee and H. Grebel, "Depositing Graphene Films on Solid and Perforated Substrates", *Nanotech.*, vol. 19, no. 36, pp. 365303-365308, 2008.

[76] D. Graf, F. Molitor, K. Ensslin, C. Stampfer, A. Jungen, C. Hierold and L. Wirtz, "Spatially resolved Raman spectroscopy of single and few-layer graphene", *Nano Lett.,* vol.7, no. 2, pp. 238-242, 2007.

[77] A. Luker, H. Hein, J. Schulz, N. Dambrowsky, O. Sternberg, M. J. Sweetgall, K. Abdijalilov, K. D. Moeller and H. Grebel, "Band pass filters in the 1 μm spectral region: thick metal screens", *J. Infrared Technol.*, vol.51, no. 3, pp. 178–185, 2008.

[78] A. Banerjee, R. Q. Li and H. Grebel, "Raman Spectrum of Graphene Coated Nano-Holes", *Mater. Res. Soc. Symp. Proc*., vol. 1059, no. kk10, pp. 26-31, 2008.

[79] A. Banerjee and H. Grebel, "Freestanding Graphene and its Applications", *ECS Tran.*, vol. 19, no. 5, pp. 53-65, 2009.

[80] L. Galvani, "De viribus electricitatis in motu musculari", *Commentarii Bononiesi*, vol.7, pp. 363-418, 1791.

[81] A. Volta, "On the electricity excited by the mere contact of conducting substances of different kinds", *Phil. Mag.*, vol. 8, pp. 289-311, 1800.

[82] B. J. Munk, "Frequency Selective Surfaces", John Wiley & Sons, Inc., New York, 2000.

[83] H. Raether, "Surface Plasmons on Smooth and Rough Surfaces and on Gratings", Springer-Verlag, Berlin, 1988.

[84] A. V. Akimov, A. Mukherjee, C. L. Yu, D. E. Chang, A. S. Zibrov, P. R. Hemmer, H. Park, and M. D. Lukin, "Generation of single optical plasmons in metallic nanowires coupled to quantum dots", *Nature*, vol. 450, pp. 402-406, 2007.

[85] A. Banerjee, R. Li and H. Grebel, "Surface Enhanced Raman with Graphenated Anodized Aluminum Oxide Substrates: the Effect of Sub-Wavelength Patterns", *Nanotech.*, vol. 20, no. 29, pp. 295502, 2009.

[86] S. Noda, M. Yokoyama, M. Imada, A. Chutinan, and M. Mochizuki, "Polarization mode control of two-dimensional photonic crystal laser by unit cell structure design", *Science* vol. 293, no. 5532, pp. 1123-1125, 2001.

[87] X. Wu, A. Yamilov, X. Liu, S. Li, V. P. Dravid, R. P. H. Chang, and H. Cao, "Ultraviolet photonic crystal laser", *Appl. Phys. Lett*., vol. 85, pp. 3657-3659, 2004.

[88] S. C. Kitson, W. L. Barnes, and J. R. Sambles, "Surface plasmons and photoluminescence", *Phys. Rev. B*, vol. 52, pp. 11441-11445, 1995.

[89] C. Zhang, K. Abdijalilov, and H. Grebel, "Surface enhanced Raman with anodized aluminum oxide films", *J. Chemical Phys.*, vol. 127, pp. 044701, 2007.

[90] R.-Q. Li, A. Marek, A. I. Smirnov and H. Grebel, "Polarization-dependent fluorescence of proteins bound to nanopore-confined lipid bilayers", *J. Chem. Phys.*, vol. 129, no. 9, pp. 095102-095105, 2008.

[91] V. Vlasov, "Carrier dynamics, optical nonlinearities and optical gain in nanocrystal quantum dots", in *Semiconductor Nanocrystals, from Basics Principles to Applications*, pp. 73-111,

[92] A. Efros, D. Lockwood and L. Tsybeskov eds., Kluwer Academic/Plenum Publishers, 2003; A. Efros, "Auger processes in nanosize semiconductor crystals", *ibid*, pp. 52-72.

[93] R. Li and H. Grebel, "Surface enhanced fluorescence (SEF): Polarization states characteristics", *IEEE Sensor J.*, vol. 10, no. 3, pp. 465-468, 2008.

[94] S. B. Luo and M. Lin, "A Portable Raman System for the Identification of Foodborne Pathogenic Bacteria", *J. of Rapid Methods and Autom. in Microbio.*, vol. 16, no. 3, pp. 238-255, 2008.

[95] Y. Ha, D. J. Stevens, J. J. Skehel and D. C. Wiley, "Xray stryctures of H5 avian and H9 swine influenza virus hemagglutinins bound to avian and human receptor analogs", *Proc. Natl. Acad. Sci.*, vol. 98, no. 20, pp. 11181-11186, 2001.

[96] J. Stevens, O. Blixt, T. M. Tumpey, J. K. Taubenberger, J. C. Paulson and I. A. Wilson, "Structure and receptor specificity of the hemagglutinin from an H5N1 influenza virus", *Science,* vol. 312, no. 5772, pp. 404–410, 2006.

[97] R. J. Russell, D. J. Stevens, L. F. Haire, Gamblin and J. J. Skehel, "Avian and human receptor binding by hemagglutinins of influenza A viruses", *Glycoconj. J.*, vol. 23, no. 1-2, pp. 85–92, 2006.

[98] J. J. Skehel and D. C. Wiley, "Receptor binding and membrane fusion in virus entry: the influenza hemagglutinin", *Annu. Rev. Biochem.*, vol 69, pp. 531–569, 2000.

[99] J. Stevens, O. Blixt, L. Glaser, J. K. Tauberberger, P. Palese, J. C. Paulson and I. A. Wilson, "Glycan microarray analysis of the hemagglutinins from modern and pandemic influenza viruses reveals different receptor specificities", *J. Mol. Biol.*, vol. 355, no. 5, pp. 1143–1155, 2006.

[100] H. L. Yen, A. S. Lipatov, N. A. Ilyushina, E. A. Govorkova, J. Franks, N. Yilmaz, A. Douglas, A. Hay, S. Krauss, J. E. Rehg, E. Hoffman and R. G. Webster, " Inefficient transmission of H5N1 influenza viruses in a ferret contact model" *J. Virol.*, vol. 81, no. 13, pp. 6890–6898, 2007.

[101] T. R. Maines, L. Chen, Y. Matsuoka, H. Chen, T. Rowe, J. Ortin, A. Falcon, N. T. Hien, L. Q. Mai, E. R. Sedyaningsih, S. Harun, T. M. Tumpey, R. O. Donis, Nancy J. Cox, K. Subbarao and J. M. Katz, "Lack of transmission of H5N1 avian-human reassortant influenza viruses in a ferret model", Proc. *Natl. Acad. Sci.*, vol. 103, no. 32, pp. 12121–12126, 2006.

[102] T. Kuiken, E. C. Holmes, J. McCauley,G. F. Rimmelzwaan, C. S. Williams and B. T. Grenfell, "Host species barriers to influenza virus infections", *Science*, vol. 312, no. 5772, pp. 394–397, 2006.

[103]K. Shinya, M. Ebina, S. Yamada, M. Ono, N. Kasai and Y. Kawaoka, "Avian flu: influenza virus receptors in the human airway", *Nature*, vol. 440, pp. 435–436, 2006.

[104]D. van Riel, V. J. Munster, E. de Wit, G. F. Rimmelzwaan, R. A. M. Fauchier, Ab D. M. E. Osterhaus and T. Kuiken, "H5N1 Virus Attachment to Lower Respiratory Tract", *Science*, vol. 312, no. 5772, pp. 399, 2006.

[105]J. M. Nicholls, A. J. Bourne, H. Chen, Y. Guan, and J. S. Peiris, "Sialic acid receptor detection in the human respiratory tract: evidence for widespread distribution of potential binding sites for human and avian influenza viruses", *Respir. Res.*, vol. 8, no. 8, pp. 73-79, 2007.

[106]A. Chandrasekaran, A. Srinivasan, R. Raman, K. Viswanathan, S. Raguram, T. M. Tumpey, V. Sasisekharan and R. Sasisekhara, " Glycan topology determines human adaptation of avian H5N1 virus hemagglutinin", *Nat. Biotech.*, vol. 26, pp. 107-112, 2008.

[107]M. B. Eisen, S. Sabesan, J. J. Skehel and D. C. Wiley, "Binding of the influenza A virus to cell-surface receptors: structures of five hemagglutinin-sialyloligosaccharide complexes determined by X-ray crystallography", *Virol.*, vol. 232, no. 1, pp. 19–31, 1997.

[108]S. J. Gamblin, L. F. Haire, R. J. Russell, D. J. Stevens, B. Xiao, Y. Ha, N. Vasisht, D. A. Steinhauer, R. S. Daniels, A. Elliot, D. C. Wiley and J. J. Skehel, "The structure and receptor binding properties of the 1918 influenza hemagglutinin", *Science*, vol. 303, no. 5665, pp. 1838–1842, 2004.

[109]T. Ito, J. N. Couceiro, S. Kelm, L. G. Baum, S. Krauss, M. R. Castrucci, I. Donatelli, H. Kida, J. C. Paulson, R. G. Webster and Y. Kawaoka, "Molecular Basis for the Generation in Pigs of Influenza A Viruses with Pandemic Potential", *J. Virol*, vol.72, no. 9, pp. 7367-7373, 1998.

[110]J. Stevens, O. Blixt, J. C. Paulson and I. A. Wilson, "Glycan microarray technologies: tools to survey host specificity of influenza viruses" *Nat. Rev. Microbiol.*, vol.4, pp. 857–864, 2006.

[111]A. Banerjee, D. Moeller, Alex I. Smirnov and H. Grebel, "Graphenated IR Screens", *IEEE Sensors J.*, vol. 10, no. 3, pp. 419-422, 2010.

[112]A. Banerjee, D. Sliwinski, K. P. Stewart, K. D. Möller and H. Grebel, "Curved infrared screens", *Opt. Letts*, vol. 35, no. 10, pp. 1635–1637, 2010.

[113]P. K. Ang, M. Jaiswal, C. Haley, Y. X. Lim, Y. Wang, J. Sankaran, A. Li, C. T. Lim, T. Wohland, O. Z. Barbaros, and K. P. Loh, "A Bioelectronic Platform Using a Graphene_Lipid Bilayer Interface", *ACS Nano*, vol. 4, no. 12, pp.7387–7394, 2010.

[114] G. M. Morris, D. S. Goodsell, R. S. Halliday, R. Huey, W. E. Hart, R. K. Belew, and A. J. Olson, "Automated Docking Using a Lamarckian Genetic Algorithm and Empirical Binding Free Energy Function"*J. Computational Chemistry,* vol. 19, no. 14, pp. 1639-1662, 2009.

[115]K. Arnold, L. Bordoli, J. Kopp, and T. Schwede, "The SWISS-MODEL Workspace: A web-based environment for protein structure homology modeling", *Bioinfo.*, vol. no. 22, pp. 195-201, 2006.

[116]M. F. Sanner, "Python: A Programming Language for Software Integration and Development", *J. Mol. Graphics Mod.*, vol 17, no. 1, pp. 57-61, 1999.

[117]S. Yamada, Y. Suzuki, T. Suzuki, M. Q. Le, C. A. Nidom, Y. Sakai-Tagawa, Y. Muramoto, M. Ito, M. Kiso, T. Horimoto, K. Shinya, T. Sawada, M. Kiso, T. Usui, T. Murata, Y. Lin, A. Hay, L. F. Haire, D. J. Stevens, R. J. Russell, S. J. Gamblin, J. J. Skehel and Y. Kawaoka, "Haemagglutinin mutations responsible for the binding of H5N1 influenza A viruses to human-type receptors", *Nature*, vol. 444, pp. 378-382, 2006.

[118]A. Chandrasekaran , A. Srinivasan, R. Raman, K. Viswanathan, S. Raguram, T. M. Tumpey, V. Sasisekharan and R. Sasisekharan, "Glycan topology determines human adaptation of avian H5N1 virus hemagglutinin", *Nat. Biotech.*, vol. 26, pp. 108-113, 2008.

[119]S. Mirza and H. Grebel, "Crisscrossed and co-aligned single-wall carbon based films", *Appl. Phys. Letts.*, vol. 91, no. 18, pp. 183102-183105, 2007.

[120]A. Banerjee, R. Perez-Castillejos, D. Hahn, A. Smirnov and H. Grebel, "Microfluidic Channels on Nanopatterned Substrates: Monitoring Protein Binding to Lipid Bilayers with Surface-Enhanced Raman Spectroscopy", *Chem Phys Letts*, vol. 489, no. 1-3, pp. 121-126, 2010.

[121]M. Fleischmann, P. J. Hendra, A. J. McQuillan," Raman spectra of pyridine adsorbed at a silver electrode", *Chem. Phys. Letts*, vol. 26, pp. 163-166, 1974.

[122]H. Grebel, Z. Iqbal and A. Lan, "Detecting single wall nanotubes with surface enhanced Raman scattering from metal coated periodic structures", *Chem. Phys. Letts.*, vol. 348, no. 3-4, pp. 203-208, 2001.

[123]J. M. Tobias, M. Ajgaonkar and H. Grebel, "Morphology-dependent transmission through photonic crystals", *J. Opt. Soc. Am. B*, vol. 19, no. 3, pp. 285-291, 2002.

[130]H. Grebel, "Surface Enhanced Raman Scattering - phenomenological approach", *J. Opt. Soc. Am B*, vol. 21, no. 2, pp. 429-435, 2004.